In situ spectroscopic Study of the Electrochemical Reduction of CO$_2$ on single facet Copper Nanoparticles

Master Thesis

Martijn Hut

6260454

20-01-2023

Supervised by

Jim de Ruiter

Dr. Ward van der Stam

Inorganic Chemistry and Catalysis (ICC)

Institute for Sustainable Chemistry and Catalysis (ISCC)

Utrecht University

Acknowledgments

Firstly I would like to thank my daily supervisor Jim de Ruiter. It was a great pleasure being you master student. Besides academically skilled you were also very socially available. I learnt a lot from you: python, illustrator, lab skills etc. During this busy learning process there was somehow always still room for a joke, which I appreciated a lot.

Secondly, I want to thank dr. Ward van der Stam for examining my thesis. You provided not only me but the whole Electrobuzz team with a very pleasant work environment, where you put the focus on not only scientific but also personal development. I want to thank you for your flexibility and availability during my thesis, which both helped me become a better researcher. You and Jim taught me a lot, which I am grateful for.

Furthermore I want to thank dr. Eelco Vogt for being my second examiner and Thimo Jacobs for his help with the TEM. Joren Dorresteijn I thank for helping me work in the glovebox and not minding me being somewhat inexperienced. I also want to thank him for measuring the beautiful SEM-images.

This thesis would not be possible without the nanoparticles that were provided to us by Zaza Ludovic Emile Frédy from the group of Raffaella Buonsanti from the EPFL in Switzerland, so I want to thank them too.

I thank Ellen Sterk and Jaap Louwen for their help with the DFT calculations. An extra thanks goes out to Jaap for performing the Stark shift calculations.

A special thanks goes out to my colleague Bas den Hartigh. It was very fun working alongside you on a similar research topic. Making practical jokes, winning the poster grant and going to n3c and of course discussing data: you made my time at ICC much more enjoyable.

My friends, family and girlfriend I want to thank for the mental support during the thesis: you pulled me through it! Last but not least, I would like to thank everyone who helped me along the way in one form or another.

Layman's abstract

Of all the different greenhouse gases, CO_2 has been found to have the greatest influence on global warming. Technologies that lower the amount of CO_2 in the atmosphere have therefore gained a lot of attention the past years. CO_2 can either be captured and stored or captured and converted into useful chemicals. This thesis focuses on the latter technique, specifically on the conversion part. In this thesis very small Copper particles, that use electricity to convert CO_2 into a range of different products, are researched. It is known that the shape of the copper particles influences the type of product CO_2 can be converted to, but it is unknown how it does so. By conducting analytical experiments and performing computer simulations, we discovered more about how copper particles use electricity to convert CO_2 into different types of products. If we know more about how copper particles convert CO_2, we might be able to use this knowledge to make this conversion more efficient in the future.

0. Abstract

Converting CO_2 into useful chemicals and fuels with renewably generated electricity is of great technological and fundamental interest. Copper stands out as an electrocatalyst for this electrochemical reduction, as it is the only metal that can induce C-C coupling and therefore can reduce CO_2 into a variety of valuable C_{2+} hydrocarbons. The product distribution of these hydrocarbons depends on a lot of factors, of which the applied potential and the exposed surface facets have the most profound influence. Generally speaking it is known that the (100) facet produces more ethylene, while the (111) facet produces more methane. The exact reaction mechanisms and their differences on the different facets remain under debate. In this thesis research we use *in situ* Raman spectroscopy and *in silico* DFT calculations to study the differences between the electrochemical reduction of CO_2 (eCO$_2$RR) on copper nano cubes and octahedrons, which have (100) and (111) facets exposed respectively. We found that, different to polycrystalline Cu (pc-Cu), linear CO (CO_L) is not stabilized on the (100) or (111) facets under working conditions. This lead to the conclusion that the C-C coupling mechanism of the eCO2RR on both facets, probably involves at least one multiple bound CO species, which are stabilized on the (100) and (111) surface. The 460, 500 and 535 cm^{-1} peaks were observed on both facets and their origin was explored, but no intermediate could be assigned to these peaks with certainty. A novel find for these peaks is their negative Stark tuning rate, which has not yet been observed in literature. The direction of this tuning rate suggests that the intermediate that is the origin of these peaks possess both a σ-orbital as HOMO and a π^{*}-orbital as LUMO, similar to CO. It was also shown that Stark tuning rates can be calculated using DFT-calculations. This type of calculation may be used in the future as a tool in determining the origin of the peaks in the 500 region, further elucidating the eCO$_2$RR mechanism.

Table of Contents

1. Introduction

1.1 Context

According to the intergovernmental panel on climate change (IPCC) the greenhouse gas (GHG) concentrations in the atmosphere and annual anthropogenic GHG emissions continue to grow and have reached a historic high.[1] Of all the GHG CO_2 was found to be the biggest contributor to global warming.[2] Technologies that lower the concentration of CO_2 in the atmosphere, such as Carbon capture and Storage (CCS) or Carbon capture and utilisation (CCU) technologies, have therefore gained a lot of interest the past decades.[3] The difference between these techniques is that during CCS CO_2 is only stored, where CCU also converts CO_2 into chemical feedstock. Of the two techniques CCU is favoured, since it not only decreases the concentration of CO_2, but also contributes to the concept of a circular economy by using a waste stream (CO_2) of one sector as a feeding stock for another.[3] Another added benefit is that CCU can be used to store intermittent renewable energy, such as wind or solar, into chemical bonds.[4] The inherent thermodynamic stability of CO_2 makes its chemical conversion very energy demanding. Homo - or heterogeneous catalysts can be used to lower chemical energy barriers in CO_2 conversion during photochemical, biochemical, thermal or electrochemical processes. In this thesis the focus will lie on the electrochemical conversion of CO_2.

1.2 Electrochemistry

General

In order to understand the electrochemical conversion of CO_2 it is useful to introduce the concept of electrochemistry. The relationship studied in electrochemistry is the one between electrical potential and chemical change.[5] Characteristic for electrochemical reactions is the exchange of electrons between two or more chemical species. This type of chemistry is known as redox chemistry. Within an electrochemical process, multiple redox reactions can occur at the same time.
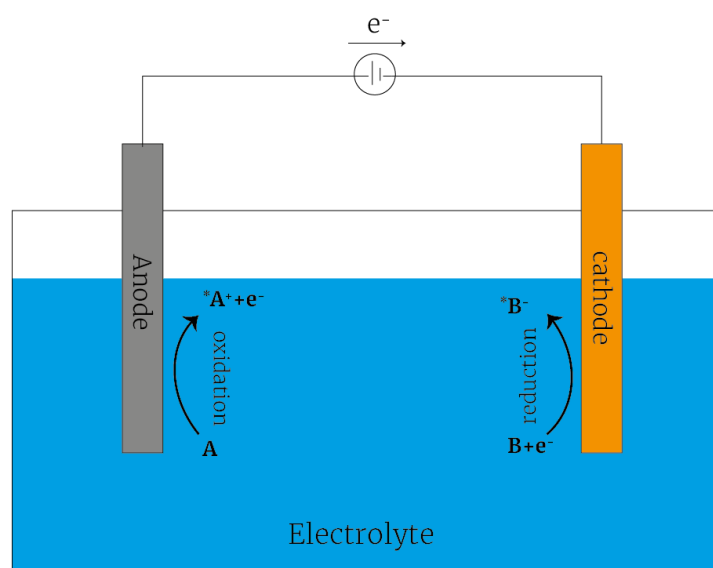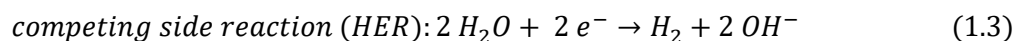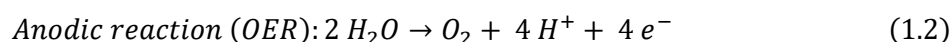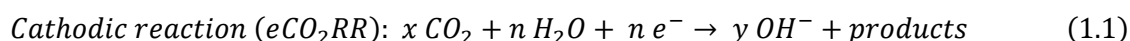

Figure 1.1 schematic representation of a simple electrochemical cell.

Electrochemical reactions happen within an electrochemical cell, which is depicted in Figure 1.1. In this cell there are two electrodes (anode & cathode) and these electrodes are connected via an external electrical circuit. Both electrodes are separated by an electrolyte, which is both electronically insulating and ionically conductive. During an electrochemical reaction half reactions occur at both of the electrodes. The electrode where the half reaction occurs in which a species loses electrons is called the anode. The electrons which are generated at the anode travel through the external circuit to the cathode, where a species gains electrons. The loss and gain of electrons is called oxidation and reduction respectively.

The electrochemical reduction of CO_2

During the electrochemical reduction of CO_2 (eCO₂R) in an aqueous solution two main half reactions occur: the reduction reaction (eq. 1.1) at the cathode side and the oxygen evolution reaction (OER, eq. 1.2) at the anode side. The protons generated at the anode react with the hydroxide ions produced at the cathode to form H_2O (eq. 1.4), which can be used to perform the eCO₂RR again. At the cathode a competing side reaction can also take place: the hydrogen evolution reaction (HER, eq. 1.3). This is a competing side reaction since the protons and electrons used in this reaction could be used to reduce CO_2.

$$Cathodic\ reaction\ (eCO_2RR):\ x\ CO_2 + n\ H_2O + n\ e^- \rightarrow\ y\ OH^- + products \tag{1.1}$$

$$Anodic\ reaction\ (OER): 2\ H_2O \rightarrow O_2 +\ 4\ H^+ +\ 4\ e^- \tag{1.2}$$

$$competing\ side\ reaction\ (HER): 2\ H_2O +\ 2\ e^- \rightarrow H_2 + 2\ OH^- \tag{1.3}$$

$$equilibrium\ water: H^+ +\ OH^- \leftrightarrow\ H_2O \tag{1.4}$$

The electrochemical cell that is used to carry out eCO₂R in this thesis is the H-cell (Fig 1.2), which is a more complex cell than the one represented in Figure 1.1. The H-cell consist of two chambers (anodic, cathodic) which are divided by a proton-selective (naffion) membrane. The membrane that separates both chambers must be permissible to protons, since the protons that are generated at the anode are needed to reduce CO_2 at the cathode. The main function of this membrane is to block reactants or contaminants from flowing freely between the two chambers. In the anodic chambre a counter electrode (anode) is present that carries out the OER. In the cathodic compartment a working electrode (cathode) that carries out the eCO₂RR is present as well as a reference electrode that ensures that a stable, well defined potential is applied during eCO₂RR. Gaseous CO_2 is constantly added to the cathodic chambre, in order to make sure enough CO_2 is dissolved in the electrolyte. The cathodic chambre is also connected to a gas chromatograph (GC), that measures gaseous products formed during the reaction.

The eCO₂RR is not a spontaneous reaction: an energy input is required to reduce CO_2 into a variety of products. This is done by applying a potential (V) between the cathode and anode via the external electrical circuit. The applied potential depends on both the thermodynamics as well as on the kinetics of the reaction (Ch 2.1). Due to the nature of

the two half reactions (eq 1.1/1.2), large potentials are required to reduce CO_2. However, electrocatalysts are able to lower the required energy input and with it the required potential.[6]
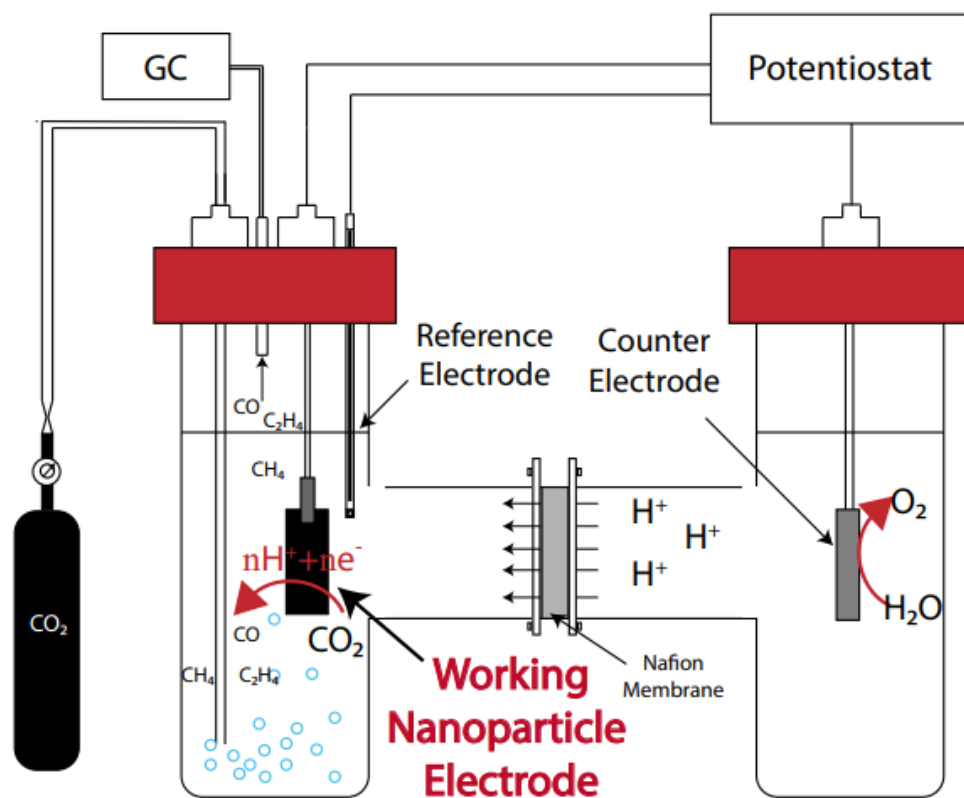

Figure 1.2: Schematic representation of an H-cell, Figure made by Kees Koolmeijer[7].

1.3 Copper as an electrocatalyst

While the use of an electrocatalyst lowers the energy input requirement significantly for these reactions, it also has a big influence on the product distribution. This is illustrated by Hori et al[8], who used different metal electrodes to carry out the eCO_2RR under the same conditions. They were able to classify the electrocatalysts into 4 groups: formate-producing (Hg, Tl, In, Sn, Cd, and Bi), CO-producing (Au, Ag, Zn, and Ga), H_2-producing (Ni, Fe, Pt, Pd, Rh, Ir and Ru), C_{2+}-producing (Cu).

The classification of these metals into these separate groups has been explained as the result of their binding energy to key CO_2R intermediates (CO, H).[9] Metals that bind *H too strongly only produce hydrogen, and metals that bind *H too weakly only produce CO or formate. The unique ability of Cu to reduce CO_2 to C_{2+} products may be due to the fact that it is the only metal that has a negative adsorption energy for *CO but a positive adsorption energy for *H (Fig. 1.3). Not only is Cu unique in its ability to make C_{2+} products it also differentiates itself from the other metals by the fact that it produces a distribution of different products, instead of just one product.
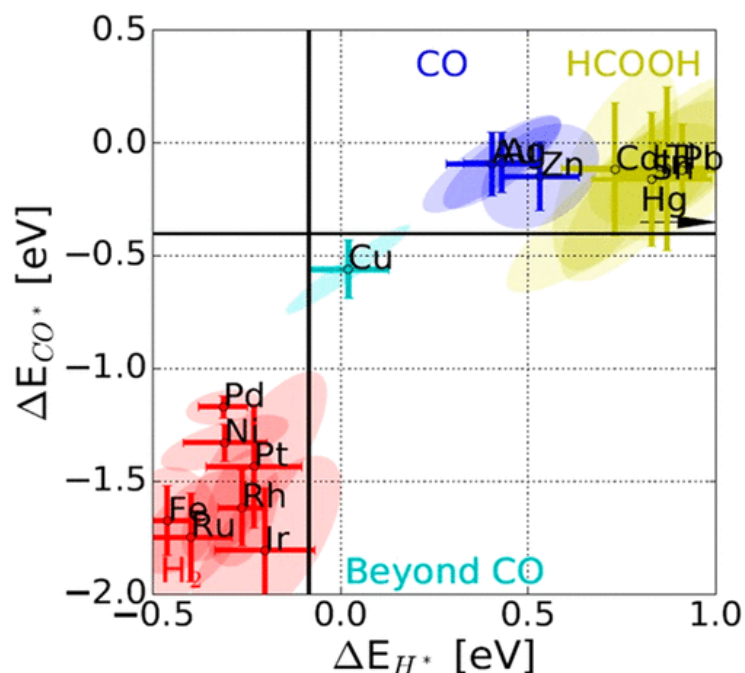

Figure 1.3: The binding energies of the intermediates CO* and H* on different metals, and their grouping. Adapted from[9]

Potential and facet dependency

The distribution of these different products on Cu is dependent on different reaction conditions (pH of electrolyte, cations in electrolyte, type of cell etc.) of which the applied potential has the most profound influence.[10] This is illustrated in Figure 1.4 where the yield of different products is plotted against the applied potentials. At lower overpotentials the HER is dominant and the main product is H_2. When moving to more cathodic potentials CO and HCOOH formation starts to increase. The most valuable hydrocarbons reach their peak around -1.0 V_{RHE}.

An applied potential leads to changes in the local environment at the surface of the catalyst, which has an effect not only on the binding energy of different intermediates[11-13] but also on the transition state energy[11,12] of intermediate reaction steps. The binding energy and the transition state energy determine the activation energy for the reaction step. Any changes in these energies thus has a consequence for the reaction product distribution, as the height of the activation energy determines the probability of the reaction occurring.

Besides potential dependent, is has also been discovered that the eCO$_2$RR on Cu is facet dependent.[14] Similarly to the applied overpotential the exposed facet has a big influence on the local environment, which has a similar consequence for the reaction product distribution. The main consensus on facet dependency is that the (100) facet produces more ethylene while the (111) facet produces more methane.
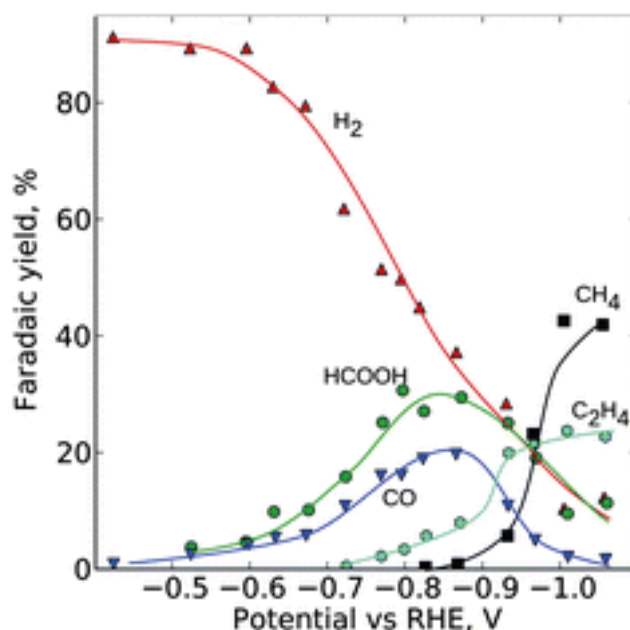

Figure 1.4: Product distribution on the copper electrode at various overpotentials. Adapted from Peterson et al.[15]

1.4 *In situ* spectroscopy of eCO$_2$RR on Cu

While it is known that the overpotential and exposed facet both have a major influence on the reaction distribution, the exact mechanism behind the formation of different products remains under debate.[16]

In situ spectroscopy can be a useful tool for elucidating the reaction mechanism. Measuring the vibrational modes of the system and its intermediates and their time – or potential dependence, conclusions can and have been made about the mechanism of the eCO$_2$RR (see Ch 2). *In situ* Raman spectroscopy can be especially insightful, as this technique probes metal-adsorbate vibrations. Since the eCO$_2$RR occurs at the surface of the Cu electrode, these types of vibrations provide information about intermediates or other surface bound species, which are vital in our understanding of the working mechanism.

Spectroscopic studies have provided valuable insights (Ch 2.3), but their reach is often somewhat limited. Since not every intermediate is present on the surface long enough to measure its vibrational modes, it is difficult to propose a full reaction pathway with just spectroscopy. With the use of DFT calculations, entire reaction pathways have been proposed. It has however also been shown that different computational models yield different results. It is therefore essential that DFT results are supported by experimental evidence.

In this thesis we attempt to further elucidate the mechanism of eCO$_2$RR by making use of a combination of *in situ* Raman spectroscopy on single facet copper nanoparticles (cubes(100) and octahedra (111)) and *in silico* DFT calculations on vibrational modes of intermediates on these facets. By combining experiment and theory we hope to come one step closer in finding the reaction mechanism.
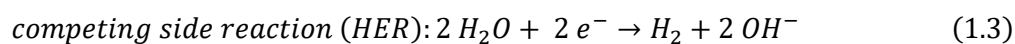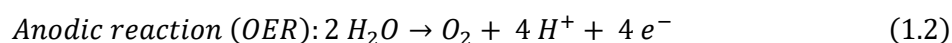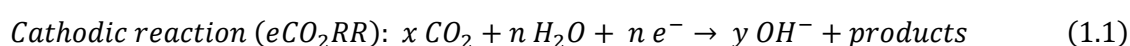
2. Theory

In this chapter theoretical background will be provided about the topics of this thesis. Starting with a deeper understanding of the thermodynamic and kinetic principles behind the eCO_2RR. Afterwards Raman spectroscopy is explained and an overview of Raman spectroscopy on eCO_2RR is provided. Finally this chapter ends with an the state of the art of the reaction mechanism of the eCO_2RR.

2.1 The electrochemical reduction of CO_2

Thermodynamics

In the introduction it was mentioned that three half reactions are involved in eCO_2R: the OER (eq 1.2), the HER (eq 1.3) and the general eCO_2RR (eq 1.1).

$$Cathodic\ reaction\ (eCO_2RR):\ x\ CO_2 + n\ H_2O + n\ e^- \rightarrow y\ OH^- + products \quad (1.1)$$

$$Anodic\ reaction\ (OER): 2\ H_2O \rightarrow O_2 + 4\ H^+ + 4\ e^- \quad (1.2)$$

$$competing\ side\ reaction\ (HER): 2\ H_2O + 2\ e^- \rightarrow H_2 + 2\ OH^- \quad (1.3)$$

For each of the many different products that can be produced in equation 1.1 a different half reaction exists. An overview of these half reactions is given in Table 2.1, adapted from[17]. Each of these half reactions has a different reduction potential (E^0_{red}). The reduction potential is a measure of the tendency of a species to gain electrons and get reduced. Where a more positive reduction potential are indicates a greater tendency to get reduced.[18] The opposite of the reduction potential is the oxidation potential (E^0_{ox}), for this potential a more negative value is indicative of a greater tendency to get oxidized.

Table 2.1: Half reaction in the eCO_2R and their oxidation and reduction potentials

Half reactions anode	Oxidation potential (V_{RHE})
$2\ H_2O \rightarrow O_2 + 4\ H^+ + 4\ e^-$	1.643 V
Half reactions cathode	Reduction potential (V_{RHE})
$CO_2 + 2\ e^- + H_2O \rightarrow 2\ OH^- + HCOO^-$	–1.078 V
$CO_2 + 2\ e^- + H_2O \rightarrow 2\ OH^- + CO$	–0.934 V
$2\ CO_2 + 2\ e^- \rightarrow C_2O_4^{2-}$	–0.59 V
$CO_2 + 4\ e^- + 3\ H_2O \rightarrow 4\ OH^- + HCHO$	–0.898 V
$CO_2 + 4\ e^- + 2\ H_2O \rightarrow 4\ OH^- + C$	–0.627 V
$CO_2 + 6\ e^- + 5\ H_2O \rightarrow 6\ OH^- + CH_3OH$	–0.812 V
$CO_2 + 8\ e^- + 6\ H_2O \rightarrow 8\ OH^- + CH_4$	–0.659 V
$2\ CO_2 + 12\ e^- + 8\ H_2O \rightarrow 12\ OH^- + C_2H_4$	–0.764 V
$2\ CO_2 + 12\ e^- + 9\ H_2O \rightarrow 12\ OH^- + C_2H_3OH$	–0.744 V
$2\ H_2O + 2\ e^- \rightarrow H_2 + 2\ OH^-$	0 V

Using the oxidation and reduction potentials of the half reactions in the electrochemical cell, you can calculate if a reaction is spontaneous or not. By subtracting the E^0_{ox} from E^0_{red} you find the total cell potential (E^0_{cell}). The gibbs free energy (ΔG^0) of the reaction can than be calculated from the E^0_{cell} using equation 2.1.

$$\Delta G^0 = -nFE^0_{cell} \tag{2.1}$$

Where n is the moles of electrons and F is the Faradaic constant (≈ 96 J/(V*n)). This means that for an electrochemical reaction to spontaneously occur a positive E^0_{cell} value is required. The more negative the E^0_{cell} value is, the more energy is required to perform that electrochemical reaction.

In the introduction (Ch 1.2) it was noted that high potentials are required to perform eCO$_2$R. By examining Table 2.1, the thermodynamic reason for these high potentials is clear: due to the positive oxidation potential of the OER and the negative values of the reduction reactions, some energy is needed to drive eCO$_2$R.

Kinetics barriers

According to Table 2.1 high value products (CH_4, C_2H_4) are thermodynamically favoured over products such as CO, but in Figure 1.4 we see that CO is produced at lower potentials than these high value products. This is because the reaction product distribution is determined by the kinetics of the reaction, not the thermodynamics. There are two main types of kinetic barriers that need to be taken into account in eCO$_2$RR[6]:

1) Activation barriers:

Different reaction steps have different activation energies. A product may be thermodynamically favoured, but if the reaction pathway towards this product contains considerable activation energies it is kinetically unfavoured. An electrocatalyst is able to lower the activation energies of reaction steps, promoting the formation of different products

2) Diffusive barriers:

a) In order to create hydrocarbons, intermediates need to be hydrogenated by reaction with surface bound hydrogen (H^*). The HER competes for these H^*, influencing the rate of hydrocarbon production.

b) In order to create C_{2+} products two carbon based intermediates need to undergo dimerization.(Ch 2.4). For dimerization to occur these carbon based intermediates need to be near each other on the surface. However some carbon based intermediates, such as CO, might diffuse back into the electrolyte before C-C coupling can occur.

Both type of barriers are important in determining the reaction product distribution of eCO$_2$RR. In this thesis we attempt to elucidate the reaction mechanism of eCO$_2$RR by primarily focussing on calculated activation barriers in literature (Ch 2.3) and spectroscopic observations of intermediates (Ch 4.3).

2.2 Raman spectroscopy

The theory on Raman spectroscopy is derived from Atkins[19], unless indicated otherwise.

Principles of Raman spectroscopy

A system can absorb radiation and use that energy to go from a lower vibrational or rotational state to a higher energy state. Similarly, a molecular system can also emit radiation when transitioning from a higher to a lower energy state. However, a molecular system can also scatter incoming radiation. It can do so elastically (without a change in energy of the radiation) or inelastically (with a change in energy of the radiation).

The scattering of radiation can be studied with Raman spectroscopy. During Raman spectroscopy a molecule is exposed to monochromatic radiation, which means that all the photons have the same energy. Most photons that encounter the molecule, are scattered elastically, this is called Rayleigh scattering. However, a small portion (about 1 in 10^7) of the photons is scattered inelastically. When photons lose energy to the molecule during the scattering this is called Stokes scattering. When they gain energy upon scattering this is called anti-stokes scattering. The gain or loss in energy is realised by a change in the vibrational or rotational state of the molecule. The radiation promotes an initial energy state to a series of virtual states and the system than returns to its final state. The energy difference between the initial and final state is either carried away or supplied by the photon. In Figure 2.1 there is a schematic representation of Raman scattering.
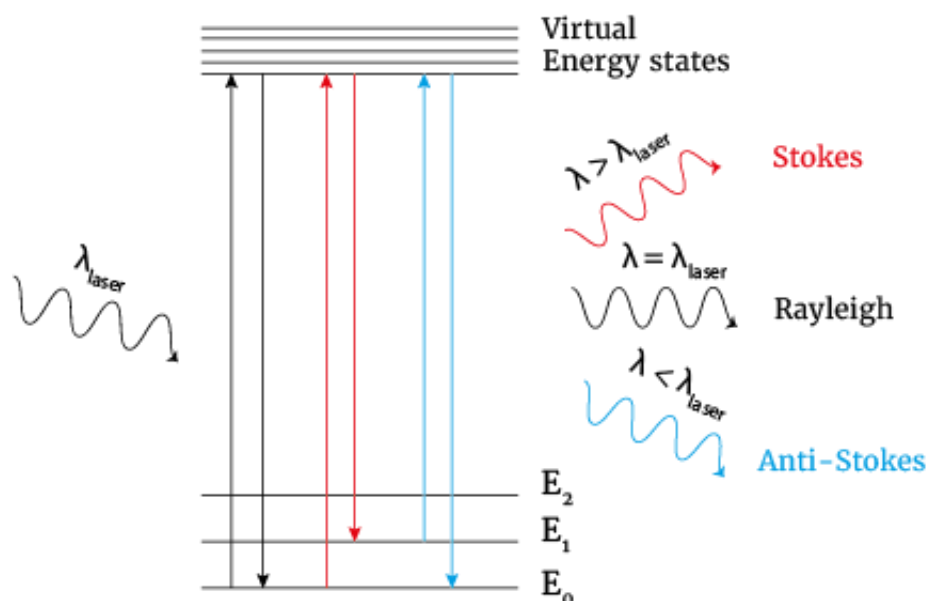
Figure 2.1: Raman scattering. Photons are scattered by a molecule and may either lose, gain or remain at the same energy. The scattering can be viewed as an excitation of an initial energy state to a series of virtual energy states and a return to the final state.

In Figure 2.2 a schematic representation of a Raman spectrometer is given. A monochromatic laser is pointed at the sample cell, . The Raman laser is scattered by the sample cell and the scattered radiation is consequently bundled and dispersed by the

monochromator or interferometer. This allows different energy photons to be independently detected.
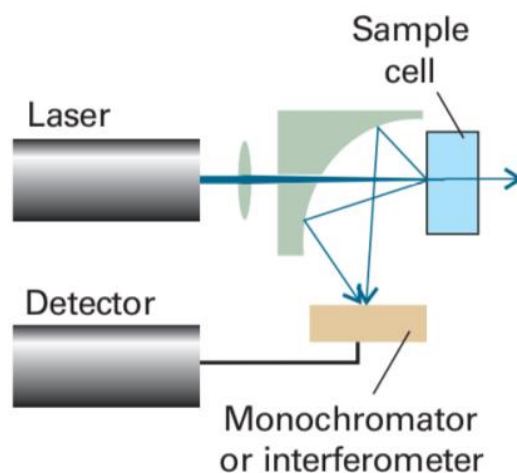
Figure 2.2: An example of a Raman spectrometer from Atkins[19]

Not every vibrational mode can be detected using Raman spectroscopy: some vibrations are Raman-active, others are Raman-inactive. For a vibration to be Raman-active the polarizability of the molecule must change during the vibration.

Raman spectroscopy on eCO$_2$RR

The multitude of peaks present in the Raman spectra measured on this electrochemical system are evidence of many Raman-active vibrational modes. Some peaks have been assigned to the vibrational modes of different intermediates, while others remain elusive. In Figure 2.3 an overview of the Raman spectra on polycrystalline copper (pc-Cu) is provided and the known vibrations are highlighted.
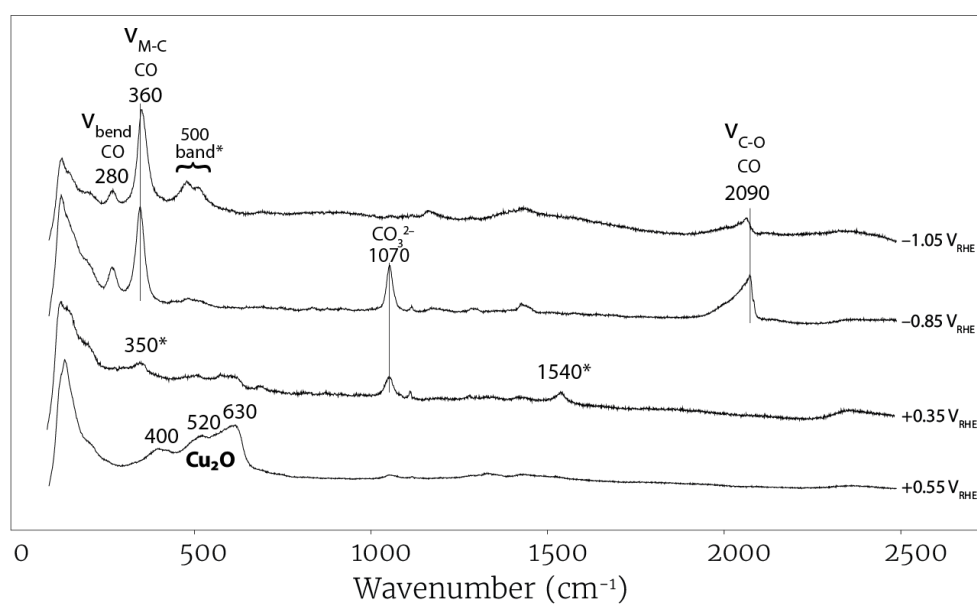
Figure 2.3: Overview of the Raman signal at different potentials on pc-Cu. The origin of the peaks with an asterisks are still under debate. Adapted from de Ruiter et al[20]

Under strong anodic potentials (+0.55 V_{RHE}) three bands are present : 630, 520, and 400 cm^{-1}, these vibrations are assigned to the vibrational modes of copper oxide. Around +0.35 V_{RHE} the copper oxide layer starts to reduce and electrolyte vibrations appear: 1070 cm^{-1}, which belongs to the stretching vibrations of carbonate (CO_3^{2-}) .The origin of the 350 and 1540 cm^{-1} peaks, which are also present at this point, remain under debate.

Under working conditions for eCO_2R three peaks are present which can be assigned to the vibrational modes of the same intermediate: 280, 360 and 2090 cm^{-1} peak. These peaks are assigned to the bending vibration ($v_{bend}$), the metal carbon stretching vibration (v_{M-C}) and the CO stretching vibration (v_{C-O}) of linear (or top-adsorbed) CO (Fig 2.4). A band around 500 cm^{-1} is also present, but the origin for this band remains under debate in literature. Scientists have assigned this band to the vibrational modes of different species: the vibrational modes of $CuO_x/(OH)_y$[21,22], a $Cu_2(OH)_2CO_3$[23] phase or intermediates beyond CO.[20] The mechanistic consequences for these spectroscopical observations are discussed in Ch 2.4.

Some Raman peaks in this system have been observed to shift, based on the applied potential. A peak shift is also observable in Figure 2.4: the 2090 peak shifts to lower wavenumbers and the 360 peak to higher wavenumber with increasing cathodic potential. This potential induced shift is called a Stark shift and is caused by the Stark effect. The Stark effect is also observed in the measured Raman spectra in this thesis and used to gain more information about the origin of certain peaks.
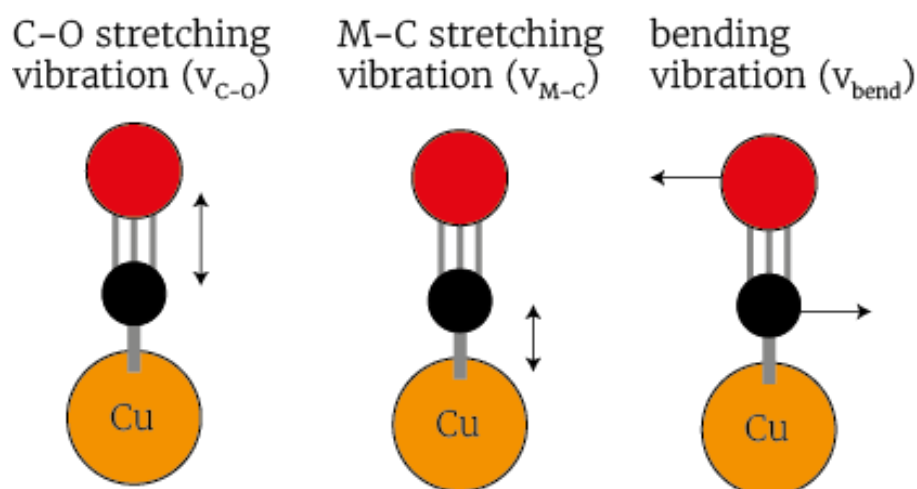

Figure 2.4: The different vibrational modes of top absorbed CO.

The Stark effect

In electrochemistry the Stark effect can be measured by applying an cathodic or anodic bias. When a bias is applied, an electric field is generated which causes a difference in an adsorbed molecular dipole moment of the molecule in the ground and excited vibrational energy states. This causes the vibrational energy levels and with them the vibrational frequencies to shift.

The degree by which these stark shifts occur is dependent on the applied bias. For sufficiently weak electrical fields (low applied biases) the stark shift is linearly dependant on the applied bias, leading to the following formula:

$$\Delta v = v - v_0 = -\Delta\mu \times F \tag{2.1}$$

Where Δv is the vibrational Stark shift, $\Delta\mu$ is the difference in dipole moments for the molecule in the ground and excited vibrational states (this is also known as the Stark tuning rate) and F is the external electric field.

It should be noted that the applied bias is not solely responsible for the generated electric field. Local fields, that originate for solute/solvent interaction, also contribute. A correction factor (f) can be added to equation (2.1) to take into account these local field contributions. [24] Furthermore it is important to state that any chemical interactions between the solvent and the solute that induce vibrational frequency shift (such as hydrogen bonding) do not fall under the Stark effect.[25]

The origin of the Stark effect is still debated in literature.[25] However there is some consensus about the effect consisting of two components[25-27], namely: an electrochemical (though-bond) and an electromechanical (through-space) component. The former is the direct effect of charging on the chemical bond of the species that is chemisorbed due to the applied electric field. The latter arises from the surface dipole interaction with the applied electric field. In Figure 2.5 a schematic representation of the 2 components of the electrochemical Stark shift is given.
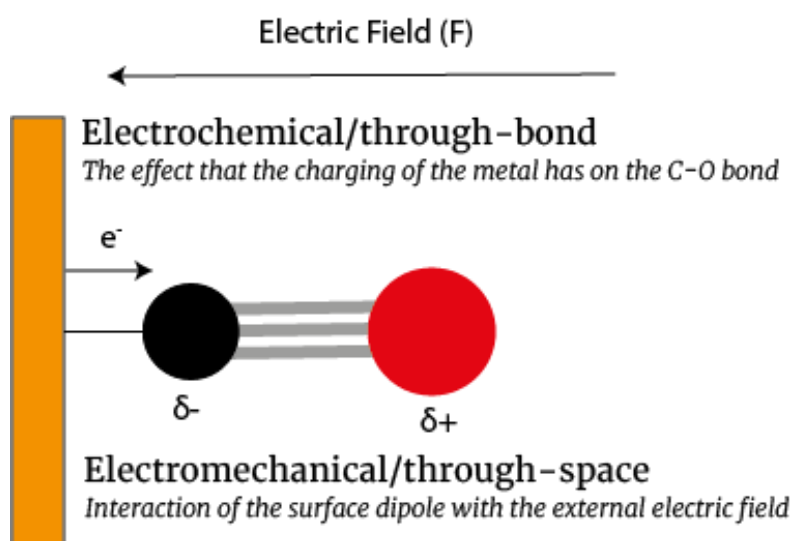

Figure 2.5: Schematic representation of the electrochemical Stark Effect.

2.3 Reaction mechanism state of the art

General reaction

Through a combination of experimental and theoretical work Xia et al[16] summarised four widely recognized basic steps in their review on eCO_2RR:

Step 1: Chemisorption of CO_2 onto the surface of the electrode and formation of a partially charged $*CO_2^{\delta-}$ species through an interplay with the surface metal atoms.

Step 2: Proton coupling/electron transfer to split the C–O bond

Step 3: The C–C bond formation to achieve a mixture of C_2 species

Step 4: Diffusion of bound intermediates from the surface to the bulk electrolyte

During Step 2 a few key intermediates are formed, one of which is CO. The reason why CO is regarded as a crucial intermediate in the eCO_2RR is because when starting from CO or CO_2 similar reaction product distributions are observed.[28,29] The spectroscopic observation of CO on the surface of the Cu electrocatalysts[20,30] is also in support of this claim.

In order to produce CO, the intermediate in step 1 ($*CO_2^{\delta-}$) needs to undergo a proton transfer (PT) to form a carboxyl ($COOH^*$) intermediate (eq 2.2).[31] The carboxyl intermediate can also be formed directly from CO_2[32,33] (skipping step 1) by undergoing a coupled proton electron transfer (CPET) (eq. 2.3). The $COOH^*$ then undergoes a CPET to make $^*CO$ and H_2O (eq 2.4). These mechanisms are shown in the equations below.

$$CO_2 + H^+ + e^- \rightarrow COOH^* \ (CPET) \tag{2.2}$$

$$CO_2 + e^- \rightarrow {}^*CO_2^- + H^+ \rightarrow COOH^* \ (ET, PT) \tag{2.3}$$

$$COOH^* + e^- + H^+ \rightarrow {}^*CO + H_2O \ (CPET) \tag{2.4}$$
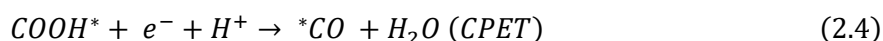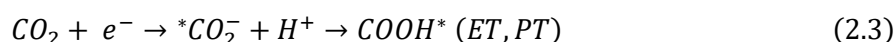
What happens after step 2 is what is mostly debated in literature. The many products that can be made during the eCO_2RR are evidence of the complexity of this reaction step. Nitopi et al.[6] made an overview of the proposed reaction pathways to reach different products (Fig 2.6). In order to reach these high value hydrocarbons a lot of electron and proton transfers are required, leading to a lot of possible of intermediates. Figure 2.6 highlights again the importance of CO as an intermediate: in order to make all the different high value hydrocarbon products CO_2 needs to first be reduced to CO.
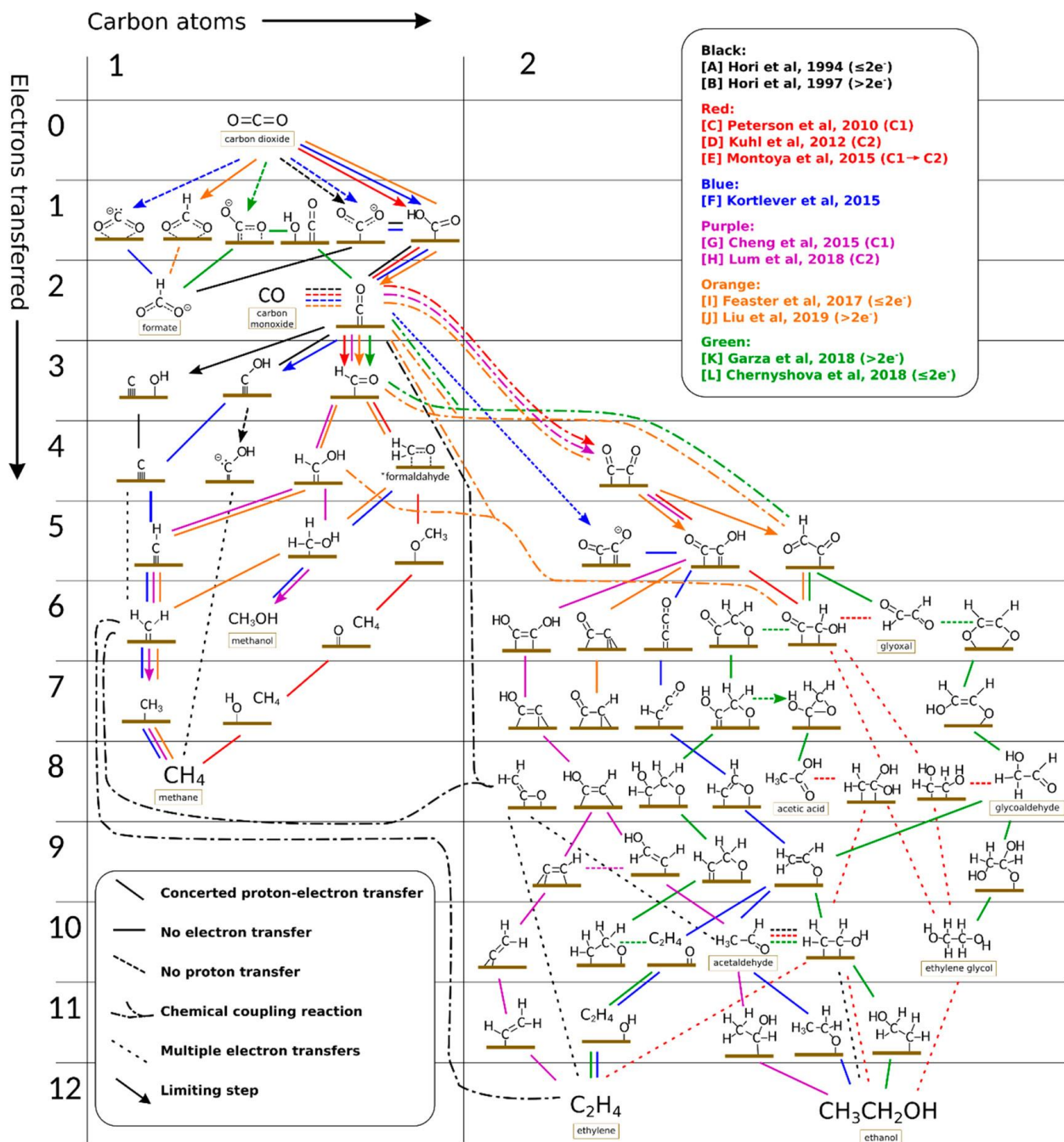
Figure 2.6: An overview of possible reaction pathways of the electrochemical reduction of CO_2 towards different products. Figure by Nitopi et al.[6]

C-C coupling and facet dependency

Even though the reaction pathways towards C_{2+} products are quite complex, there is one step that all pathways share: a C-C coupling step. A C-C bond is induced by the dimerization of two carbon based intermediates, such as two *CO molecules. Schouten et al.[34] have shown experimentally that the dimerization process is facet-dependent. By conducting differential electrochemical mass spectrometry (DEMS) experiments at different pH's on Cu(100) and Cu(111) they discovered that on Cu(100) there are at least two dimerization processes that can take place, while at Cu(111) only one dimerization process takes place. They suggested that at relatively low overpotentials CO-CO coupling can take place on the Cu(100) facet, but not on the (111) facet. This is supported by DFT calculations in later studies[35,36], where the CO-CO dimer was found to be stable on (100) facets, but not on (111) facets.

The second dimerization pathway that can occur on both facets is the subject of debate. Making use of DFT-calculations scientists have argued that for the other dimerization pathway to occur *CO is first further reduced to *HCO[11,36] or *COH[35] (Fig 2.7) . These two intermediates can than reduce further to form methane or they can dimerize with *CO and be reduced further to C_{2+} products.

Of course other dimerization processes could be conceived, in principle many reduced carbon based intermediate could dimerize. However the concentrations of many of these intermediates is likely to be very low, which makes it unlikely for these intermediates to be an important contributor to the C-C coupling.[36]
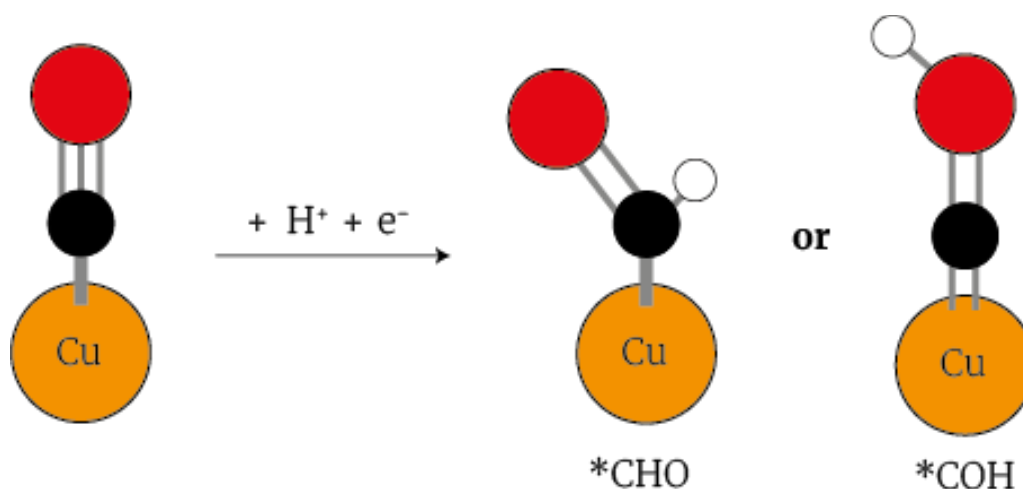
Figure 2.7: The first reduction step after the reduction towards CO: the reduction towards HCO or COH

Spectroscopic evidence

Although DFT calculations can provide valuable insights with regards to the mechanism, it has been shown that different computational models yield different results. It is therefore essential that DFT results are supported by experimental evidence.

Spectroscopic studies on the eCO_2RR have mainly been focussed on CO and electrolyte species, since the vibrational modes of these intermediates have been assigned to certain peaks and visible during the reaction.

By relating the peak intensity ratio between the v_{M-C} and v_{bend} of top absorbed CO to the activity towards C_{2+} products Roldan et al.[37] were able to relate C_{2+} product formation to CO coverage. An et al.[30] were able to use the v_{C-O}, to differentiate different types of CO and their relation to different products.

There is not much spectroscopic evidence on intermediates beyond CO. In one study Pérez-Gallent et al.[38] claim to have discovered spectroscopic evidence of the hydrogenated dimer (OCCOH*) using Fourier transform Infrared (FTIR) spectroscopy. Furthermore C-H vibrations have been observed on Cu foil measurements using Raman spectroscopy, suggesting that other intermediates than CO can be observed.

3. Methods

3.1 Chemicals

As particles were provided by an external party the chemicals used in this thesis do not include the chemicals needed to synthesize the particles. Ultrapure water was obtained using a Direct-Q® 3 UV water purification system. KHO_3, 99.7% was used for making the electrolyte.

3.2 particle synthesis

The particles used in this thesis are provided to us by Zaza Ludovic Emile Frédy (EPFL) in the form of ~2 ml vials containing a concentration of ~1mg/ml cubes or octahedra dissolved in toluene. These particles were synthesized according to the following procedures (provided by Zaza, based on[39,40]):

Cubes synthesis

TOPO (trioctylphosphine oxide; 3.5 g) was loaded in a 250 ml three-neck flask connected to a Schlenkline under N_2 atmosphere and degassed for 30 minutes. 115 mL of OLAM (oleylamine) was added and degassed under stirring for 30 minutes at 120°C. 0.25 g of CuBr was added when the mixture had cooled down to 40°C. The reaction mixture was heated and stirred at 80°C for 10 minutes under vacuum and then at 260°C for 1h under nitrogen atmosphere. After the reaction, the solution was washed with hexane in a 1:1 ratio and centrifuged for 10 minutes at 6000 rpm. The suspension was recovered with a minimum amount of hexane, diluted with a 1:1 ratio of ethanol, and centrifuged for 10 minutes at 6000 rpm. The Cu nanoparticle suspension was recovered and stored in a minimum amount of toluene. The suspension was stored in the fridge of a glovebox to avoid the evaporation of toluene and keep a constant concentration of Cu nanoparticles.

Octahedra synthesis

CuBr (6.4 mmol), TOP (8.0 mmol) and olelyamine (360 mmol) were mixed in a three-neck round-bottom flask (250 ml) in a glovebox before the flask was connected to a Schlenkline. After 60 mins of nitrogen flow at room-temperature and then at 80°C, the reaction was heated to 270°C and kept for 1 hour. When the heating process was finished, the heating mantle was removed, the reaction solution allowed to cool naturally and the sample was centrifuged with toluene 2 times at 6000 rpm before being redispersed and stored in toluene.

3.2 Electrode synthesis

Electrodes were prepared by drop casting the nanoparticle solution onto a 1 by 1 cm glassy carbon (GC) and drying overnight under inert atmosphere. The amount of μL drop casted was dependent on the exact concentration of the nanoparticle solution. The goal was to create a 15 μg/cm^2 catalyst loading, the amount of μL was chosen accordingly based on the concentration of the solution.

In between measurements the GC was cleaned by polishing it with Al_2O_3 powder and rinsing it with ultrapure water. The GC was then brought over into a small vial containing

a 1:1:1 mixture of ethanol:acetone:ultrapure water. This vial was sonicated for 10 min. Finally the GC was removed from the vial and rinsed using ultrapure water.

3.3 Experimental

Raman

Prior to performing Raman measurements the electrodes were pre-treated in order to remove ligands stuck to the surface of the electrode. This was done by washing the electrode three times with ethanol and consequently with ultrapure water. The electrode was then electrochemically pre-treated in 0.1M CO_2 sat. $KHCO_3$ by applying overpotential of –1.6 $V_{Ag/Ag+}$ for 300 seconds. The electrode was washed one final time with ethanol and ultrapure water before performing Raman measurements.

In Figure 3.1 the Raman cell is visualized and its different parts are highlighted.
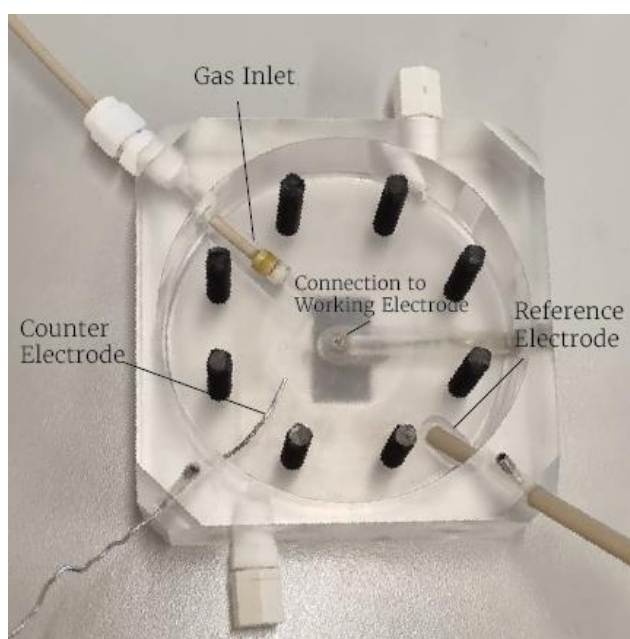
Figure 3.1 The *in situ* Raman cell

Raman measurements were carried by placing the electrode in the middle of the *in situ* Raman cell and anchoring it in place. Then the electrolyte solution containing CO_2 saturated 0.1M $KHCO_3$ was added to the cell. The spectroscopic measurements were carried out using the Renishaw® inVia confocal Raman microscope and a 785 nm laser. The objective for the *in situ* measurements was a Nikon 40X, 0.80 NA water immersion objective. The Raman cell was connected to a Metrohm Autolab PGSTAT101 potentiostat. The standard settings for the measurements were a laser power of 10%, extended Step measurements with 5 steps from 200-3200 cm^{-1} with an exposure time of 1 s.

Data-processing

Some Raman spectra have been baseline-corrected, this was done using the SNIP algorithm.[41]

When peaks were fitted, they were fitted to Lorentzian functions with upper and lower boundary conditions and initial guesses (set by the user per experiment), using the scipy.optimize function.

Activity

Activity measurements were carried out in the H-cell (Fig 1.2) as explained in the introduction. This H-cell was connected to a GAS Compact GC 4.0 gas chromatograph equipped with two two flame ionization detectors and thermal conductivity detectors. Every ~4 minutes a GC sample was taken during catalysis.

The working electrode was the similar to the electrode used in Raman experiments, only it had a slightly higher loading (~60 μg/cm^2) and it was not pre-treated. The counter electrode used was a platina mesh and the reference electrode a saturated Ag/AgCl electrode. A constant flow of CO_2 and Kr gas was bubbled through the cathodic compartment during catalysis with a flow rate of 10 mL/min and 0.2 mL/min, respectively. Both compartments were filled with an electrolyte solution of CO_2 saturated 0.1M $KHCO_3$.

Transmission Electron Microscopy (TEM)

For the TEM images the FEI Technai-T20 microscope was used. An accelerating voltage of 200 kV was applied during operation. TEM samples were prepared by drop-casting a small drop of the nanoparticle solution on a 300-mesh copper grid coated with a polymer (Formvar) and carbon inside of the glovebox and drying overnight.

High resolution super electron Microscopy (HR-SEM)

For the HR-SEM images the SFEI Helios Nanolab G3 was used at an electron energy of 2.0 kV and a probe current of 0.1 nA.

3.4 Computational details

All DFT calculations in this work were performed using the Vienna Ab-initio Simulation Package (VASP) with the projector-augmented wave (PAW) method. The exchange-correlation functional that was used was the Perdew-BeckeErnzerhof (PBE). The Cu bulk system was constructed by making a cubic Fm3m unit cell with a lattice constant of 3.6147 Å and expanding this unit cell four times in all directions. The geometrically optimized bulk system showed no difference in lattice constant and next nearest neighbour distance.

A (100) slab was constructed by constructing a new cubic Fm3m unit cell using the optimized parameters from the Bulk calculation. This unit cell was expanded two times in the a & b direction and three times in the c direction.

A (111) slab was constructed by constructing a new cubic Fm3m unit cell using the optimized parameters from the Bulk calculation. This unit cell was consequently multiplied with the following matrix:

$$\begin{pmatrix} -0.5 & -0.5 & -1 \\ 0 & 1 & -1 \\ 0.5 & -0.5 & -1 \end{pmatrix}$$

This new (111) unit cell was expanded two times in all directions.

Relaxation was allowed for all atoms. The kinetic energy cut off for the plane wave basis set was 400 eV. Monkhorst-Pack mesh k-points of (3x3x1) was used for the geometry optimisation calculation of the slab with adsorbates. Each slab was applied with 20 Å vacuum perpendicular to the surface between the layers, in order to prevent interaction of intermediates due to translation of the super-cell in the z-direction. Dipole-dipole interactions between super-cells are avoided by adsorption on both sides of the exposed surface retaining a centre of inversion. An energy criterion was used for the ionic convergence using the conjugate gradient algorithm. Geometries were converged to 10^{-4} eV and electronic convergence was set at 10^{-5} eV.

For the gas-phase calculations of OH, CO, HCO , a Γ centred grid for k-point sampling was used. The molecules were placed at the origin of a 10x10x10 Å unit cell. A Gaussian smearing with a width of 0.00002 eV was used for electron smearing.

For all slab with adsorbates, the adsorbate molecules and the Cu atoms they were attached to were allowed to relax and a selective dynamic calculation was performed in order to find the vibrational energies. The Hessian matrix was constructed using a finite displacement approach with a step size of 0.02 Å for displacement of individual atoms along each Cartesian coordinate.

4. Results

The main goal of this thesis is to elucidate the mechanism of the eCO2RR by making use of *in situ* Raman spectroscopy on well defined, single facet nanoparticles. As explained in the introduction the eCO$_2$RR is facet dependent: the (100) facet produces more ethylene, while the (111) facet produces more methane. Any spectroscopic differences between these two facets, may be attributed to the preferential formation of these different products, leading to a better understanding of the reaction mechanism. The particles used in this thesis are colloidally synthesized nano cubes and octahedra, which respectively have the (100) and (111) facet exposed.

4.1 Characterisation

The particles used in this thesis were synthesized by PhD student Zaza Ludovic Emile Frédy from the group of Raffaella Buonsanti from the EPFL in Switzerland (see Ch 3.2).

In order to make sure the particles had retained their morphology upon arrival in our lab, TEM-images were taken. These TEM-images are compared to the TEM-images taken by Buonsanti et al. before shipping the particles (Fig. 4.1).
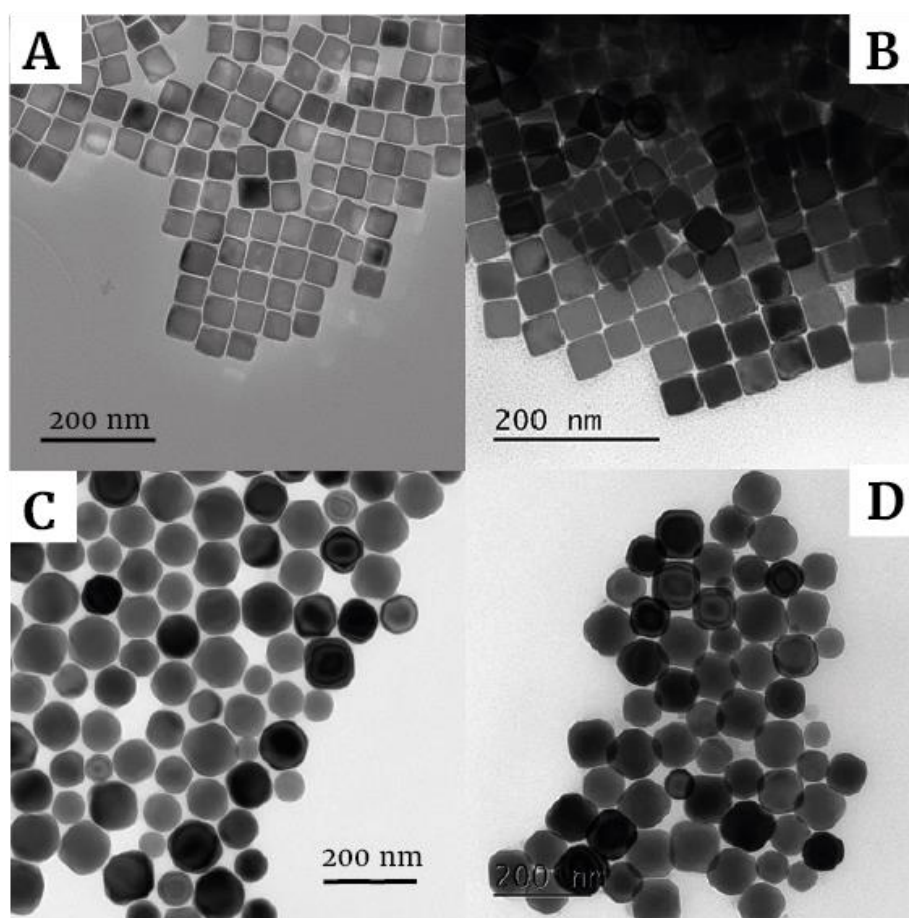

Figure 4.1: TEM-images (A t/m D) of the copper nanocubes (A, B) and octahedrons (C, D). The images on the left were made in our lab, the ones on the right in the lab of Buonsanti et al.

It was observed that the NP morphology was unaffected during sample transfer. The cubes were found to have an average size of 49.1nm ± 3.9 and the octahedra an average size of 90.0nm ± 12.2.

The morphology of these particles suggests that the orientation of the facets these particles is as expected: (100) for the cubes and (111) for the octahedra. The orientation of the exposed facet was confirmed with XRD measurements by Buonsanti et al. prior to shipping the particles.

It is important that we make sure that the nanoparticles under study remain stable during electrocatalysis, so that any changes in the Raman spectra can be attributed to the molecular dynamics of the reaction and not to any structural changes the particles undergo during electrocatalysis.

In order to measure the stability of the particles HR-SEM images were taken before and after electrocatalysis. For both the cubes and octahedra three samples were prepared: one sample which had only been pre-treated, one sample which underwent pre-treatment and performed electrocatalysis for 1 hour under -1.6 $V_{Ag/Ag+}$ and one sample which underwent pre-treatment and performed electrocatalysis during a cyclic voltammetry (CV) program. During CV current is measured against time as the applied potential is cycled between an upper vortex and lower vortex potential with a certain scan rate. The CV program for this measurement included a lower vortex potential of -1.7 $V_{Ag/Ag+}$ an upper potential of -1 $V_{Ag/Ag+}$ with a stepsize of 10 mV and a scanning rate of 3.33mV/s for 8 cycles. An overview of the different HR-SEM images is given in Figure 4.2 (next page)

The images taken after only the pre-treatment show that the morphology of the particles is not affected by the pre-treatment. The stable morphology also suggests that the exposed facet was not altered during the pre-treatment, which is important for this research on facet-dependency.

After one hour of electrocatalysis, the morphology of the cubes still seems to be intact, while the octahedrons seem slightly deteriorated. The tiny bulges that are present on the surface of the octahedrons could be small copper oxide heaps, that were formed when the Cu surface was oxidized by the air in the time it travelled from the activity set up to the microscope. It could also be that these bulges are metallic copper atoms that are starting to come loose of the surface as a part of the restructuring process.

The cyclic voltammetry program had a bigger influence on the morphology of both the cubes as well as the octahedrons. After this program, the cubes started to form spikes, these spikes were somewhat removed by the electron beam from the SEM. The octahedrons show even more evidence of restructuration, with tiny islands of Cu agglomerates being visible on the electrode. In general the cubes showed a higher degree of stability than the octahedrons

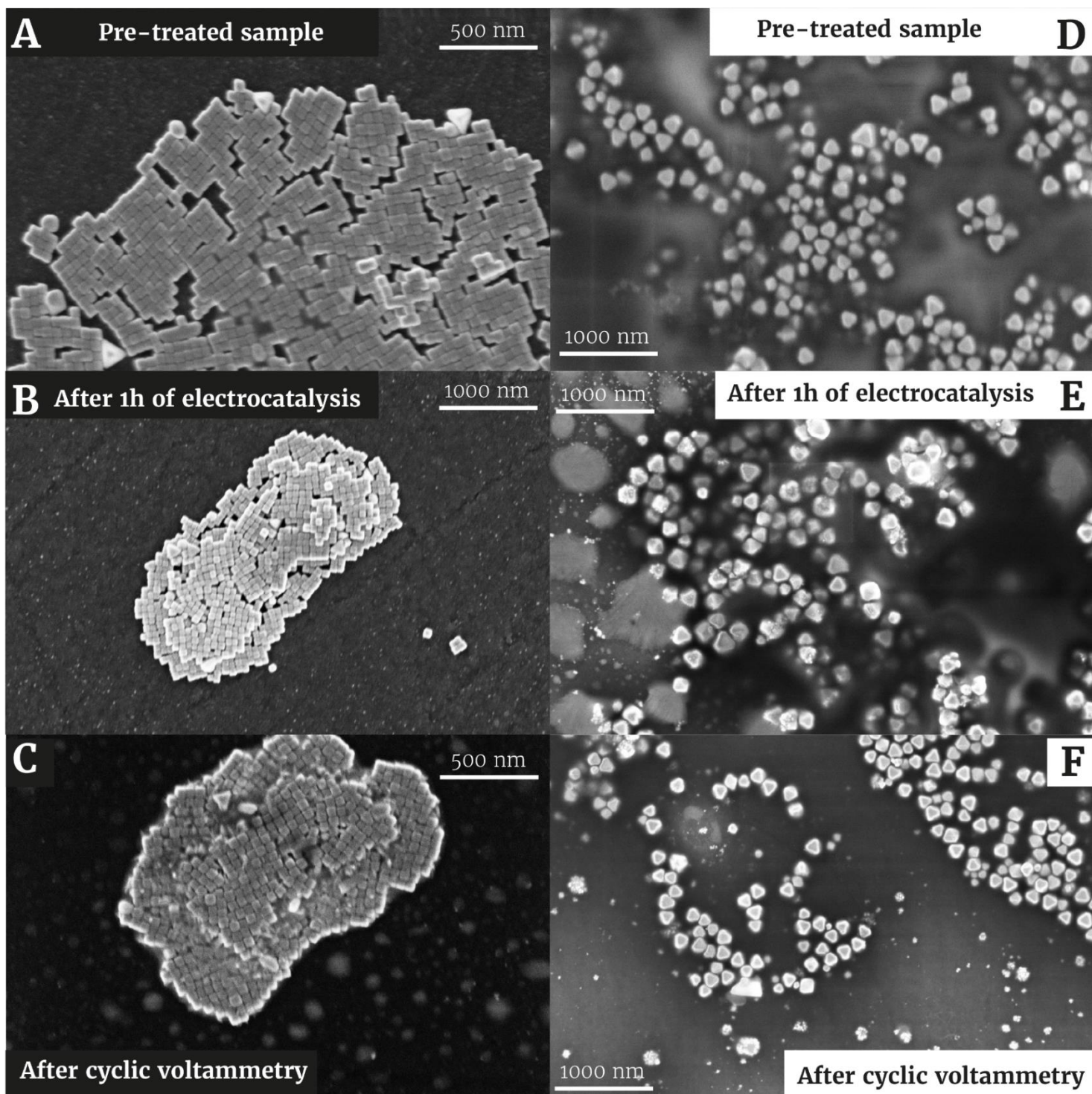*Figure 4.2: HR-SEM images of Cu cubes (A,B,C) and octahedrons (D,E,F) after: pre-treatment (A,D) pre-treatment + electrocatalysis for 1 hour under –1.6 $V_{Ag/Ag+}$ (B,E) pre-treatment + cyclic voltammetry program with a lower vortex potential of –1.7 $V_{Ag/Ag+}$ an upper potential of –1 $V_{Ag/Ag+}$ with a step size of 10 mV and a scanning rate of 3.33mV/s for 8 cycles (C,F)*
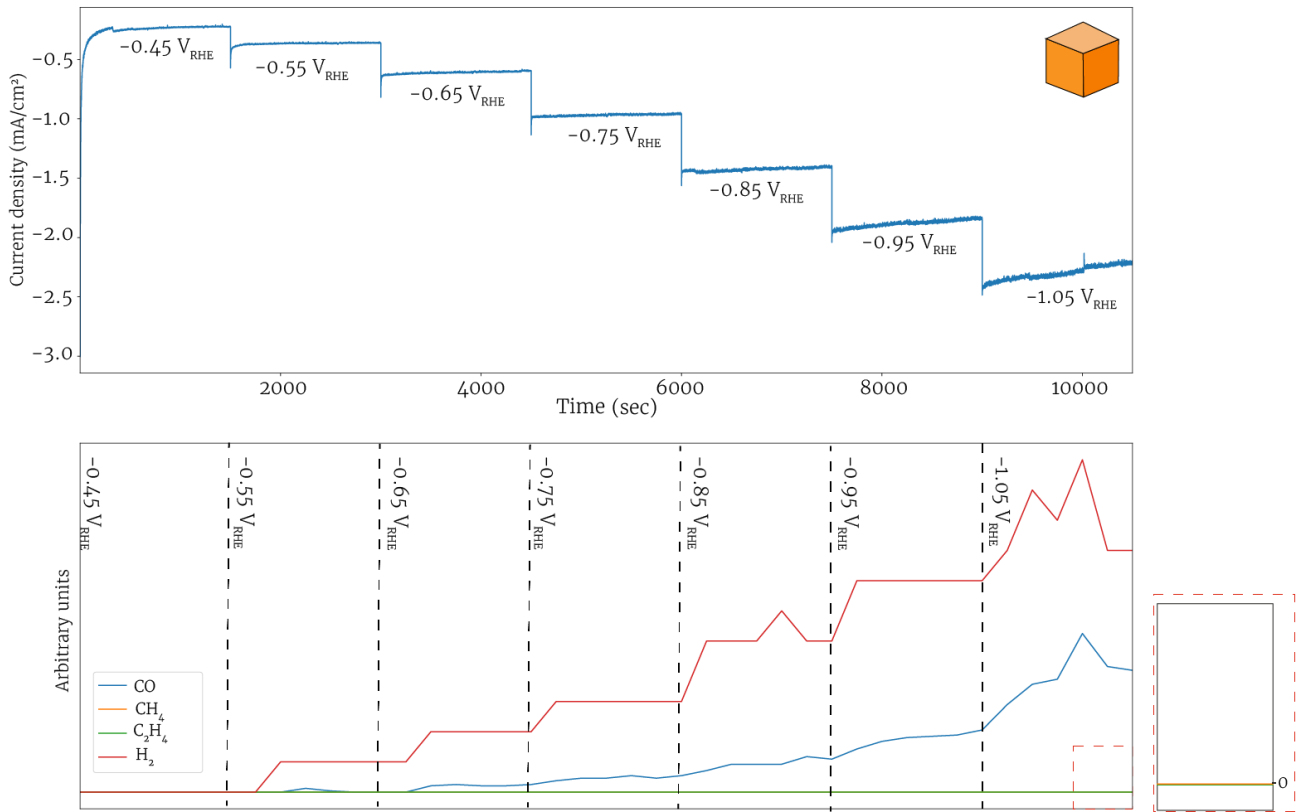
4.2 Catalytic performance

For the *in situ* spectroscopic analysis of these nanoparticles not only the morphology and the exposed facet are of importance, but also the catalytic activity. In order to make conclusions about the reaction mechanism, we need to know how our system behaves over time and under varying overpotentials. By comparing the temporal evolution and potential dependency of the spectroscopic data to its catalytic behaviour under the same conditions, different products might be linked to certain peaks.

Firstly it is good to compare the product distribution of the cubes and octahedra, to check if the preferential product formation observed in literature is also observed for these particles. Activity measurements carried out by Buonsanti et al.[39,40] (Appendix, Fig. A1) confirmed that the cubes produced more ethylene, while the octahedra produced more methane. These measurements also revealed that both particles had a different optimal potential, where most high value products were produced.

This means that both types of particles exhibit different potential dependent behaviour. In the introduction it was mentioned that a difference potential dependent behaviour has been observed in literature for the cubes and octahedra. Schouten et al.[34] showed that the cubes and octahedra have different onset potentials for different products. A different (minimum) overpotential is thus required on different facets for the same product. The onset potential for different products can act as a valuable tool for the spectroscopic analysis in this thesis. By conducting *in situ* Raman experiments above and below the onset potentials and observing which peaks appear or disappear, links can be made between peaks and products. For instance if peak A increases in intensity when the production of product B increases, peak A might be related to the production of B.

Determining the onset potentials was done by conducting Chrono-amperometry (CA) experiments at different potentials and observing the product formation at these potentials. In a CA experiment current is measured against time, at controlled potentials. The least cathodic overpotential at which a product would appear was assigned as the onset potential. The results of these experiments are given in the Figure 4.3.

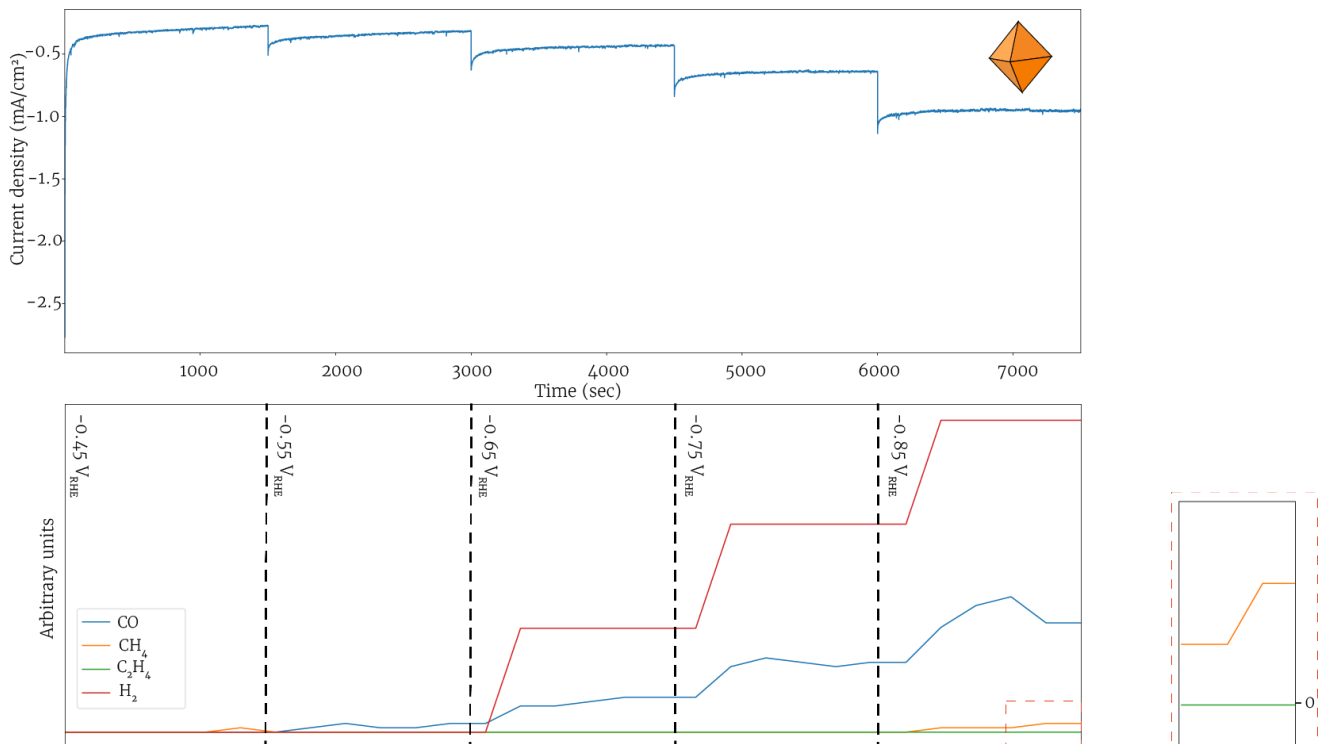*Figure 4.3: Stepped Chrono-Amperometry measurement on octahedra (bottom, -0.45 V_{RHE} to -0.85 V_{RHE}.) and cubes (top, -0.45 V_{RHE} to −1.05 V_{RHE}) . Measured in an H-cell in CO_2 sat. 0.1M $KHCO_3$ electrolyte.*

The results above seem to suggest that the onset potential for methane on the octahedrons lies at –0.85 V_{RHE}, which is close to the literature value.[42,43] The data also

suggests that the onset potential of ethylene lies at a more negative potential than –0.85 V_{RHE}. However, in literature, Cu(111) is shown to have similar onset potentials for methane and ethylene. A reason why ethylene is not observed at these overpotentials is that the amount of ethylene produced during this experiment lies below our detection limit.

The onset potential for both methane and ethylene on the cubes seems to lie at a potential more negative than –1.05 V_{RHE} according to this experiment. This also seems to be a consequence of the detection limit. As literature reports onset potentials between –0.6 and –0.7 V_{RHE} for ethylene formation, and for methane formation between –0.85 and –0.9 V_{RHE}.[42,43]

One way to make sure the detection limit of the GC is reached is to have a high catalyst loading. The catalyst loading for this experiment is quite low (60 $\mu g/cm^2$), which means the quantity of reaction product will also be. The loading wasn't increased for new experiments, since catalyst loading was found to influence not only the amount of products produced, but also the reaction distribution. [44]

For the in situ Raman measurements, the catalyst loading should not be too high since too much activity causes bubble formation, which blocks the Raman laser, causing severe drops in signal intensity. Since the main focus of this thesis is the *in situ* Raman measurements the decision was made to use a catalyst loading of ~15 $\mu g/cm^2$ and using onset potentials found in literature for similar systems.

In future experiments DEMS, or online electrochemical mass spectrometry (OLEMS), which are much more sensitive techniques, might be used to find onset potentials and learn more about the relationship between vibrations and reaction products. DEMS experiments were attempted for this thesis, however due to unforeseen difficulties with the equipment they failed.

In Figure 4.3 temporal behaviour is also noticeable. Once a new potential is applied, it takes time for the product formation to reach a steady state. For the (111) facet the CO formation increases and then plateaus after applying a more cathodic overpotential. This effect is most pronounced when -0.75 V_{RHE} is applied. For the (100) facet the CO formation keeps increasing and has not plateaued before a new potential is applied. Time dependent catalytic behaviour has also been observed by Huang et al.[45] for copper nano cubes. They observed a varying product distribution for the first two hours of the reaction, before the reaction reaches a steady state (Appendix, Fig A2). During these two hours, ethylene and methane production was observed to increase.

Both the temporal evolution of reaction product distribution, as well as the onset potential values found in literature are important for the analysis of the *in situ* Raman data in the next section of the thesis. These features allow for a comparison between the observed peaks and reaction products.

4.3 Raman spectroscopy

Overview of Raman spectroscopy on eCO2RR on Cu nanoparticles

In this thesis we use *in situ* Raman spectroscopy to help elucidate the reaction mechanism. In the theory section (Ch 2.2) an overview was given about the different types of vibrations observed on pc-Cu. In this section a more complete overview of the different types of vibrations and their place in the spectrum is provided, before going into a detailed analysis of the spectra. In Figure 4.4 an overview of the Raman spectra of the copper nano cubes and octahedrons is given alongside a spectrum on pc-Cu. The spectra are divided into 4 different regions: the metal-adsorbate vibrations region (<600 cm^{-1}), the electrolyte, glassy carbon & ligand vibrations region (1000–1650 cm^{-1}), the C-O stretching vibration region (1700-2100 cm^{-1}) and the C-H stretching vibration region ($\sim$2850 cm^{-1}).
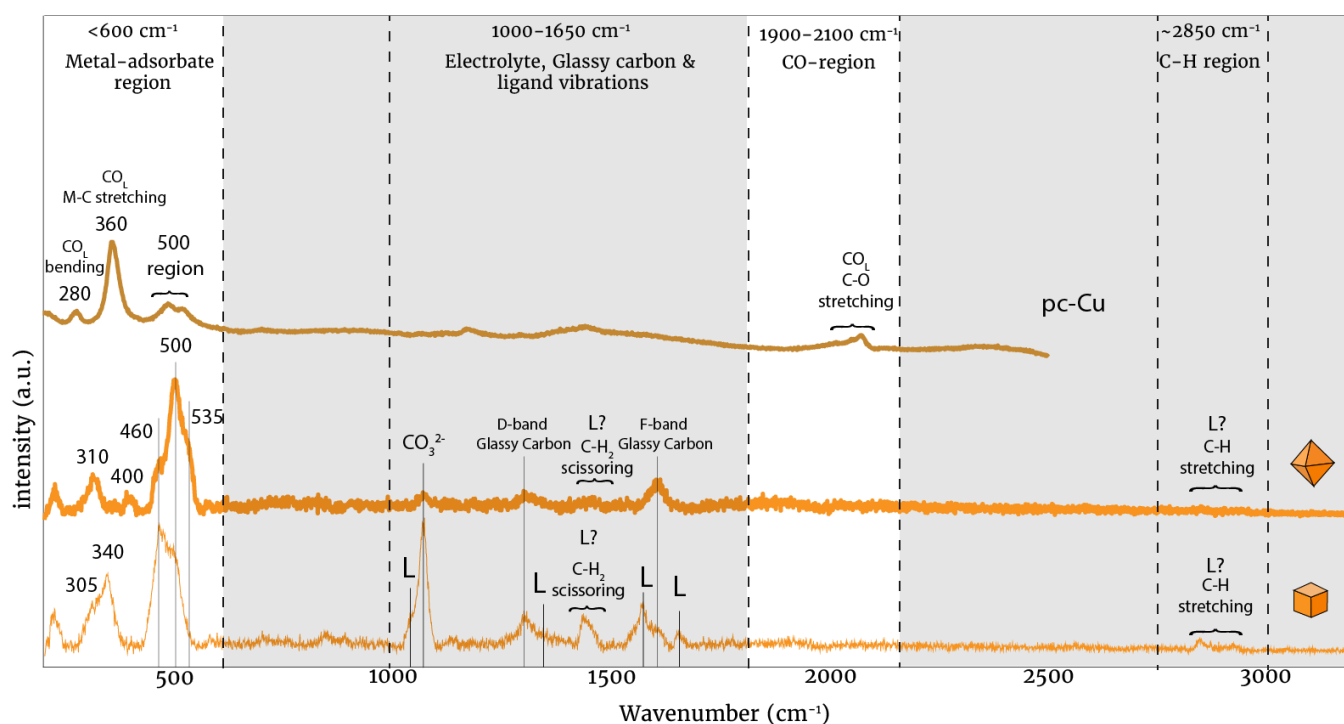
Figure 4.4: A comparison and overview of the Raman spectra form the nano cubes and octahedra. Measured at –0.85 V$_{RHE}$ (Cubes an octahedra) and –1.05 V$_{RHE}$ (pc-Cu) in 0.1M KHCO$_{3r}$. Vibrational modes which originate from ligand species are tagged with an "L"

Vibrational modes belonging to intermediates or other species that are expected to play an important role in the reaction mechanism are the vibrational modes of interest in this thesis. Regions where peaks are present which can be assigned to ligands or glassy carbon are therefore omitted, since the peaks in this region cannot be attributed to intermediate species with certainty. In the 1000–1650 cm^{-1} region both the ligands as well as the glassy carbon exhibit vibrational modes (Appendix, Fig A3). The same goes for the vibrational modes in the C-H region. Even though certain peaks (C-H stretching vibrations (v_{C-H}) at $\sim$2850 cm^{-1}, C-H$_2$ scissoring vibrations ($v_{scissoring}$) at $\sim$1440 cm^{-1}) have also been observed on a Cu foil system, which is free from ligands, in this work they will not be discussed in detail.

The C-O stretching vibration (v_{C-O}) region is studied in this thesis. As mentioned before, CO is regarded as an important intermediate for the eCO$_2$RR, which makes this region not only interesting but also important for elucidating the reaction dynamics. In this region the nanoparticle electrodes again show differences to the pc-Cu electrode: the v_{C-O} of CO$_L$ which is present on the pc-Cu, is absent on both nanoparticle electrodes.

The main focus of this thesis will lie on the lower end of the spectrum: the metal-adsorbate region. Since in heterogeneous catalysis the reaction occurs at the surface of the catalyst, the origin of the vibrations in this region might be different intermediates involved in the eCO$_2$RR.

The metal-adsorbate region can be further divided into 2 subregions: the 300 region (280-400 cm^{-1}) and the 500 region (450-540 cm^{-1}).

In the 300 region two known vibrations are present on pc-Cu: the 280 and 360 cm^{-1} vibration, which are attributed to the bending (v_{bend}) and M-C stretching (v_{M-C}) vibration of linear CO (CO$_L$).[31,46,47] These two vibrations are absent on the single facetted nanoparticles. Instead a 340 and 305 cm^{-1} vibration are present on the cubes and a 310 and 400 cm^{-1} vibration on the octahedra in the 300 region. These vibrations have not yet been observed in literature and their origin is therefore unknown.

The 500 region is characterized by 3 different peaks, present on both types of particles: 460, 500 and 535 cm^{-1}. These peaks are also present on pc-Cu. The origin of these peaks remains under debate in literature. Scientists have assigned these peaks to the vibrational modes of different species: the vibrational modes of CuO$_x$/(OH)$_y$[21,22], a Cu$_2$(OH)$_2$CO$_3$[23] phase or intermediates beyond CO.[20]

It should be noted that the exact position of the peaks in the 300 and 500 region shifts slightly depending on the facet and the applied potential. In the next section the time and potential dependent behaviour of the Raman spectra is compared to the catalytic behaviour under the same conditions. On the basis of this comparison proposals are made about the origin of the peaks in the 300 and 500 region.

Potential dependency

To discover more about the relationship between the peaks in the metal-adsorbate region and the formation of different products, potential dependent Raman measurements were carried out. Raman spectra measured above and below the onset potentials for ethylene and methane are compared, in order to investigate the connection between these products and different peaks.

Octahedrons

For the octahedrons an in situ Raman experiment was carried out at –0.55 V_{RHE}, which is well above the found onset potential of methane (∼–0.9 V_{RHE}) and ethylene (∼–0.9 V_{RHE}). This spectrum is compared to a spectrum measured at –0.95 V_{RHE}, which is just below the same onset potentials. (Fig 4.5)

Figure 4.5: In situ Raman experiment of the octahedrons on two different overpotentials: –0.55 V_{RHE} and –0.95 V_{RHE}. Measured in CO_2 sat. 0.1M $KHCO_3$.

At –0.55 V_{RHE} the ν_{C-O} of CO_L is observable around 2025 cm^{-1}. The observation of this vibrational mode is expected, since –0.55 V_{RHE} lies below the onset potential of CO.[42,43] In the metal-adsorbate vibration region two peaks can be observed at this overpotential: ~280 cm^{-1} and ~325 cm^{-1}. These vibrational modes have not yet been observed in literature. The 280 cm^{-1} vibration has been observed on pc-Cu systems as the ν_{bend} of CO_L,

however this peak is always accompanied by a $v_{M\text{-}C}$ peak at 360 cm^{-1}. This means that this 280 peak is not the same 280 peak that is observed on pc-Cu, since the 360 peak is absent on Cu(111). That is not to say that the 280 peak cannot be attributed to a CO$_L$ species on Cu(111), it could be the case that the energy of the vibrational modes of CO$_L$ change dependent on the exposed facet of the Cu electrode. The presence of the 280 and 325 cm^{-1} peak simultaneously with the the $v_{C\text{-}O}$ of CO$_L$, suggests that these vibrations might belong to the v_{bend} and $v_{M\text{-}C}$ of CO$_L$, respectively.

When measuring at a potential which lies below the onset potential for methane and ethylene (–0.95 V$_{RHE}$), the Raman signal is evidently different. In the metal-adsorbate the 325 and 280 cm^{-1} peak have disappeared, while the 310 and 400 cm^{-1} appeared in the 300 region. New peaks also appear in the 500 region a trio of vibrations around 500 cm^{-1} (460, 500, 535 cm^{-1}). At the same time, in the CO region between 1800–1900 cm^{-1}, a big bump appears, while the 2025 cm^{-1} peak remains visible.

In literature the vibrations in the 1800–1900 cm^{-1} have been assigned to the $v_{C\text{-}O}$ of bridged or multiple-bound CO (CO$_B$).[48,49] If the $v_{C\text{-}O}$ of CO$_B$ are present, the $v_{M\text{-}C}$ of CO$_B$ is to be expected in the metal-adsorbate region. Since the 400 cm^{-1} vibration appears simultaneously with the $v_{C\text{-}O}$ of CO$_B$ at 1850 cm^{-1} , a possible assignment for this vibration is the $v_{M\text{-}C}$ of CO$_B$. In literature it has been observed that, with more cathodic overpotential the adsorption strength of the CO$_B$ intermediate becomes higher[48], which could explain why the $v_{M\text{-}C}$ of CO$_B$ has a higher energy than the $v_{M\text{-}C}$ of CO$_L$. A possible assignment for the 310 peak would then be the v_{bend} of CO$_B$.

This experiment seems to suggest that the peaks in the 500 region might be related to the formation of ethylene and/or methane, as the peaks are only observable below the onset potential for those products. However more evidence is needed to link the formation of ethylene and/or methane to the peaks in the 500 region.

Cubes

For the cubic nanoparticles a similar experiment was carried out in order to gain information about the relationship between reaction products (ethylene and methane) and peak evolution. *In situ* Raman experiments were carried out above and below the onset potential for ethylene and methane on the cubes. The Raman spectra from these experiments are given in Figure 4.6
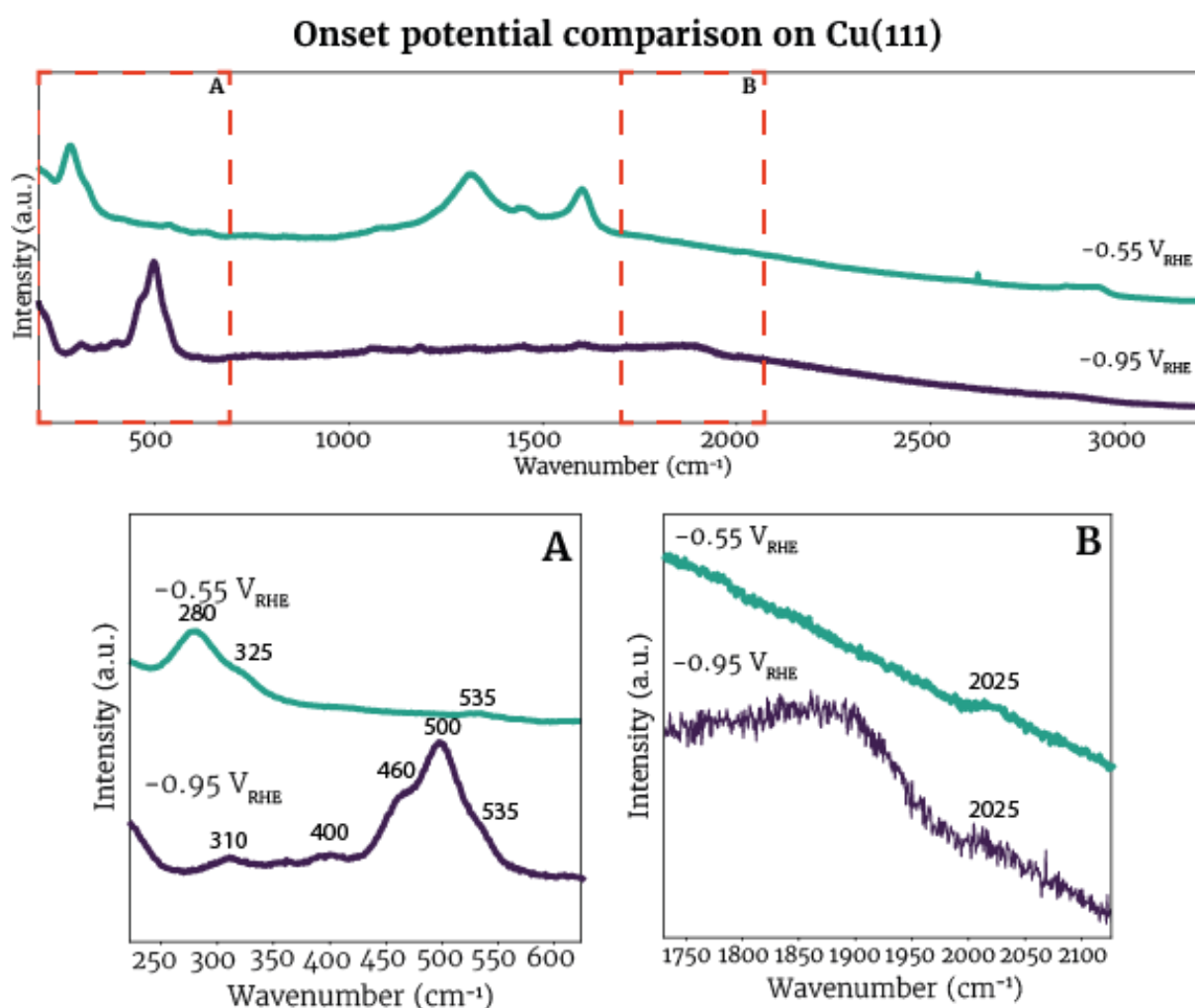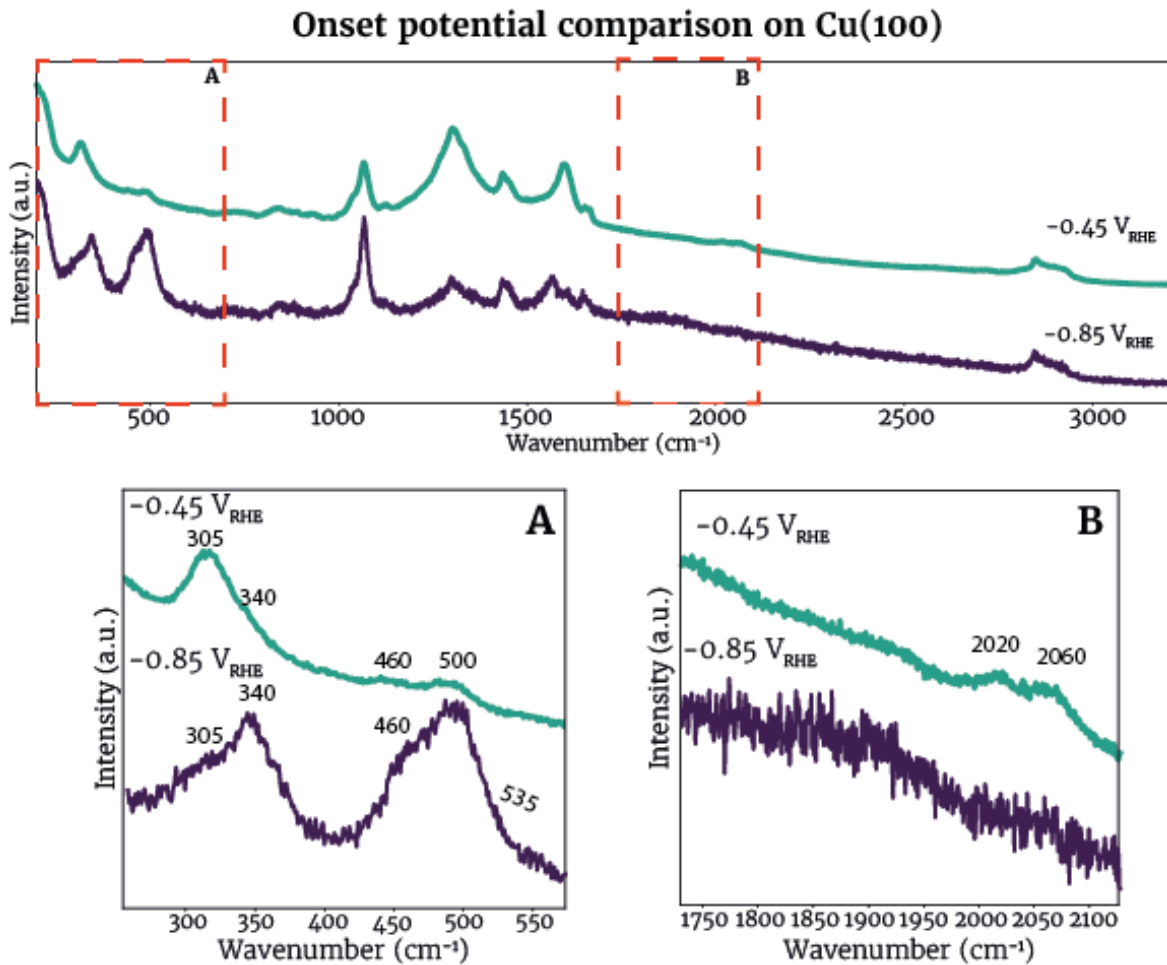
Figure 4.6: In situ Raman experiment of the cubes on two different overpotentials: –0.45 V_{RHE} and –0.85 V_{RHE}. Measured in CO_2 sat. 0.1M $KHCO_3$.

At –0.45 V_{RHE} the v_{C-O} of CO_L can be observed at 2020 and 2060 cm^{-1}. This observation is expected, since –0.45 V_{RHE} lies below the onset potential of CO.[42,43] The observation of two bands for the v_{C-O} of CO_L has also been observed in literature. Hongyu et al[30] describe the presence of a low frequency band (LFB) and high frequency band (HFB) CO at 2050 and 2090 cm^{-1} respectively. The difference in vibrational energy for the CO_L vibrations observed in this experiment and in the paper by Hongyu, et al, strengthens the suspicion of the previous section: the energy of CO_L vibrations is facet dependent.

In the metal-adsorbate region one high intensity peak is present around ~305 cm^{-1}. However this peak seems quite broad and might have a shoulder peak at ~340 cm^{-1}. Two very low intensity peaks are also present: 460, 500 cm^{-1}.

The presence of these last two peaks seems counter the assignments of these vibrations to intermediates that promote ethylene or methane formation. Since –0.45 V_{RHE} lies above the onset potential for ethylene or methane on the cubes, no methane or ethylene directing species should be expected at the surface. However, while these vibrations are visible, their low relative intensity might suggest a low concentration of the intermediates belonging to these vibrations. A possible explanation could be that at less cathodic overpotentials, some ethylene or methane directing intermediates can be formed, but

cannot be converted into these products until a more cathodic potential is applied. Another explanation for the observation of these peaks is that these peaks belong to the vibrational modes of a spectator species, which doesn't contribute to the reaction.

At –0.85 V_{RHE} the 460 and 500 cm^{-1} vibrations have gained a lot of intensity. Furthermore the 340 cm^{-1} seems to have overtaken the 305 cm^{-1} peak in intensity. In the CO region the v_{C-O} of CO_L have disappeared, while a bump (similar to the octahedrons) appears. It should be noted that the bump is much smaller in intensity on (100) than on (111) and is therefore more difficult to observe.

The 305 cm^{-1} vibration might be attributed to the v_{M-C} of CO_L on (100), since this vibration has a high intensity when the v_{C-O} of CO_L is present in de CO region. As mentioned before, the v_{C-O} of CO_L has a different energy on the (100) facet than on pc-Cu. It is therefore reasonable to assume that the v_{M-C} of CO_L on (100) might have a different energy than the v_{M-C} of CO_L on pc-Cu. The 340 cm^{-1} vibration might then be attributed to the v_{M-C} of CO_B.

In Table 4.1 a summary is given of the possible assignments of the different vibrations on the basis of their potential dependent behaviour

Table 4.1: Possible assignments for vibrations on Cu(100) and Cu(111) on the basis of the potential dependency

Peak position	Facet	Assigned vibration
280 cm^{-1}	(111)	V_{bend} CO_L
305 cm^{-1}	(100)	v_{M-C} CO_L
310 cm^{-1}	(111)	V_{bend} CO_B
325 cm^{-1}	(111)	v_{M-C} CO_L
340 cm^{-1}	(100)	v_{M-C} CO_B
400 cm^{-1}	(111)	v_{M-C} CO_B
460, 500, 535 cm^{-1}	(100), (111)	Ethylene/methane promoting vibrations Or Spectator vibrations
1800–1900 cm^{-1}	(100), (111)	v_{C-O} CO_B
2000-2100 cm^{-1}	(100), (111)	v_{C-O} CO_L

The potential dependent behaviour of the Raman spectra has given some insights into the possible origin of peaks that are present. However the assignments made in Table 4.1, based on the potential dependency alone, are not conclusive. More information is needed on how these peaks behave under various conditions, to give strength to these

assignments. It is known that the catalytic activity of the nanoparticles is time-dependent, so it will be worthwhile to study the time-dependent behaviour of the Raman spectra as well.

Time dependency

In chapter 4.2 it was mentioned that it takes a while for the eCO_2RR to reach a steady state. Before the reaction reaches this steady state, the product distribution varies over time. In literature it has been observed that when performing electrocatalysis at $-1.1\ V_{RHE}$ on copper nanocubes for the first hour of the reaction, ethylene and methane production increases (Appendix, Fig A2). This temporal catalytic behaviour can be compared to temporal peak evolution, in order to gain more insight into the origin of the peaks in the Raman spectra.

An *in situ* Raman experiment was performed on both types of particles are measured for 1.5 h at $-0.85\ V_{RHE}$, which lies around or below the onset potential for methane and ethylene (Fig 4.7).
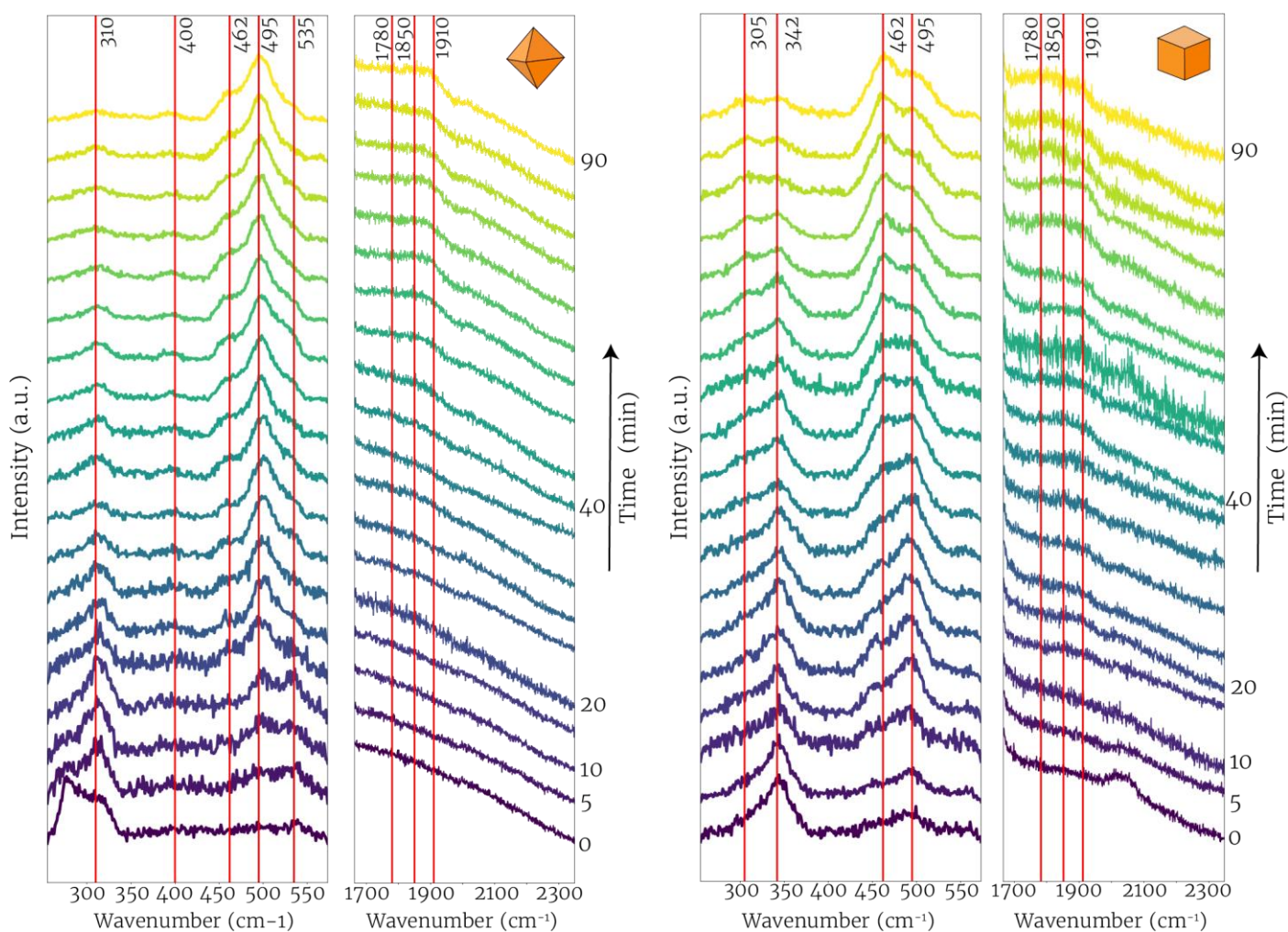

Figure 4.7: *Temporal evolution of the in situ Raman signal of the Cubes (right) and Octahedrons (left) . The 500 region was baseline corrected. Measurement was carried out at -0.85 V_{RHE} in CO_2 sat. 0.1 M $KHCO_3$. electrolyte*

Both types of particles show clear time-dependent behaviour. On both particles the v_{C-O} of CO_B develops over time. The peaks in the metal-adsorbate region also evolve over time and the ratio between the peaks in this region changes. A connection can be made between the evolution of the peaks in the 500 cm^{-1} region and the previously described temporal reaction product evolution. As mentioned before in the first hour of the reaction the methane and ethylene formation increases. The peaks in the 500 region also increase in intensity during the first hour. This temporal behaviour suggests a link between the vibrations around 500 cm^{-1} and ethylene and methane formation.

However an increase in Raman signal could also be evidence of a poisonous/spectator species. If poisonous/spectator species are present during the reaction and possess Raman-active vibrational modes, they are expected to show up in the Raman spectra and their intensity is expected to increase over time. These types of species are not converted to other products and therefore their concentration on the surface ever increases. In literature poisoning of Cu electrocatalysts have been observed and explained by the accumulation of carbonaceous species.[50]. The peaks in the 500 region might therefore originate from these carbonaceous species. Another possibility is that these vibrations could be attributed to OH$^-$ species, since the local pH also increases over time, due to the nature of the half reactions occurring at the cathode (eq 1.1, 1.3). Bridged CO[48] and HCO[51] have also been proposed as possible poisoning/inactive intermediates in literature.

From Figure 4.7 it might also be concluded that the cubes and octahedrons show distinct differences in the 500 peak ratio evolution. However, the ratio between the peaks in the 500 region differs per experiment (Appendix, Fig. A4). A possible explanation for this behaviour is that the system we are measuring is very delicate, small changes in reaction conditions can have big consequences for the Raman signal. Local environment also plays an important role. When measuring at the same potential on the same sample, but on a different spot, differences in peak ratio can be visible (appendix, Fig A5).

That said, some overarching conclusions can be made about the temporal evolution of the peaks on the nanoparticles. One constant is that the 460 to 500 peak ratio increases over time, for both the cubes and the octahedrons. This is illustrated in Figure 4.8 where the intensity of the 500 and 460 peak as well as the aforementioned ratio are plotted against time.
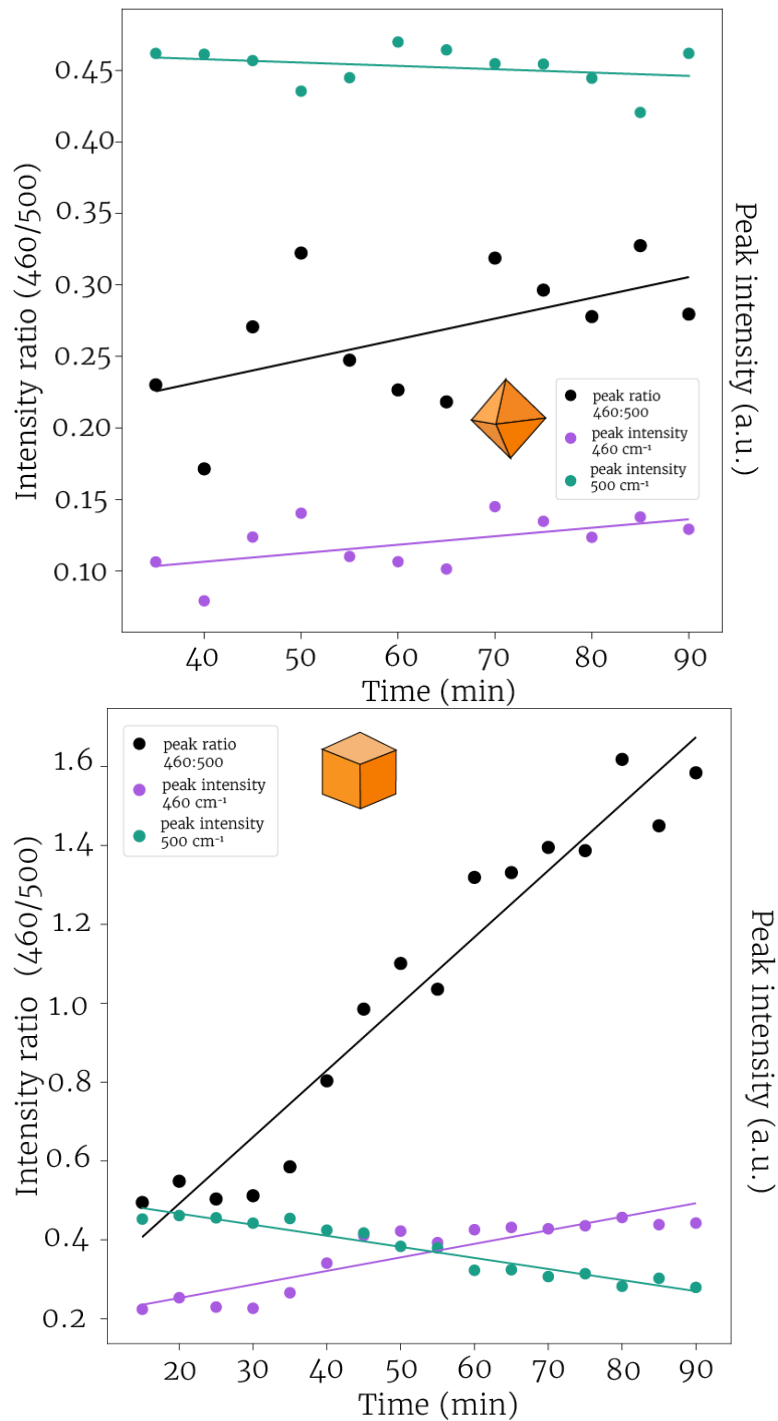
Figure 4.8: Temporal evolution of the peak intensity ratio between the 460 and the 500 peak for the octahedrons (left) and the cubes (right) from the Raman spectra in Figure 4.7.

To achieve the plots in Figure 4.8 the 500 region was fitted using the scipy.optimize function and three Lorentzians, with one set of boundary conditions. One drawback of this analysis method is that in order to fit the 500 region to the three different Lorentzians, the intensities of the peaks present must be significantly large, for scipy to recognize the peaks. This is also why, in Figure 4.8, the ratio plot for the octahedra start at a later point in time than the ratio plot for the cubes. Another drawback is that the peak fitting is not always optimal, sometimes scipy.optimize gets it wrong. However, by adding a trend line through the points, an increase in the 460:500 over time is visible. It should be noted that

the trend for the cubes is much clearer than the trend for the octahedra in this experiment.

The temporal evolution of the 460 to 500 peak intensity ratio can be linked to the temporal product distribution mentioned in chapter 4.2, but it can also be evidence of a spectator/poisonous species. It could be possible that the 460 peak could be ascribed to a HCO peak, which initially causes an increase in methane and ethylene formation, but eventually poisons the surface overtime.

Until now we have looked at the increase/appearance or decrease/disappearance of different peaks in the *in situ* Raman spectra and linked them to the activity of the catalyst. On the basis of this comparison we assigned different peaks to different intermediates. However, peaks are not only able to increase/appear or decrease/disappear, the peak positions are also able to shift. The shifting of the peak position with a change in potential is called a Stark shift (see Ch 2.2). In the next section the Stark shifts that are observed in our Raman spectra are explored and the consequences for the assignments discussed.

4.4 Stark tuning rate

The electrochemical Stark shift or the Stark tuning rate can act as a tool to strengthen our previously made assignments. The direction of the peak shift under a change in potential can be characteristic for different types of intermediates (see Ch 2.2). In this section Stark tuning rates are calculated by applying CV program and monitoring the peak positions.

The CV experiment was carried out on the cubes as well as octahedrons to determine the Stark shift of peaks in the metal-adsorbate region. With an upper vortex potential of –1.55 V_{RHE} and a lower vortex potential of –0.35 V_{RHE}, a step potential of –10 mV and a scan rate of 10 mV/s, which resulted in an interval time of 1 s. During this program a static Raman signal was recorded in the metal-adsorbate region, with a laser power at 10% and an exposure time of 1 s.

In the Figures 4.9 and 4.10 the voltammograms and the *in situ* Raman heatmaps are plotted above each other, first for the octahedra then for the cubes. In the Raman heatmap the wavenumbers are presented on the y-axis, while the real time is presented on the x-axis. Each vertical line on the heatmap represents a Raman spectrum, the colours on each line represent the intensity of the spectrum at that wavenumber, where more yellow represents a higher intensity.
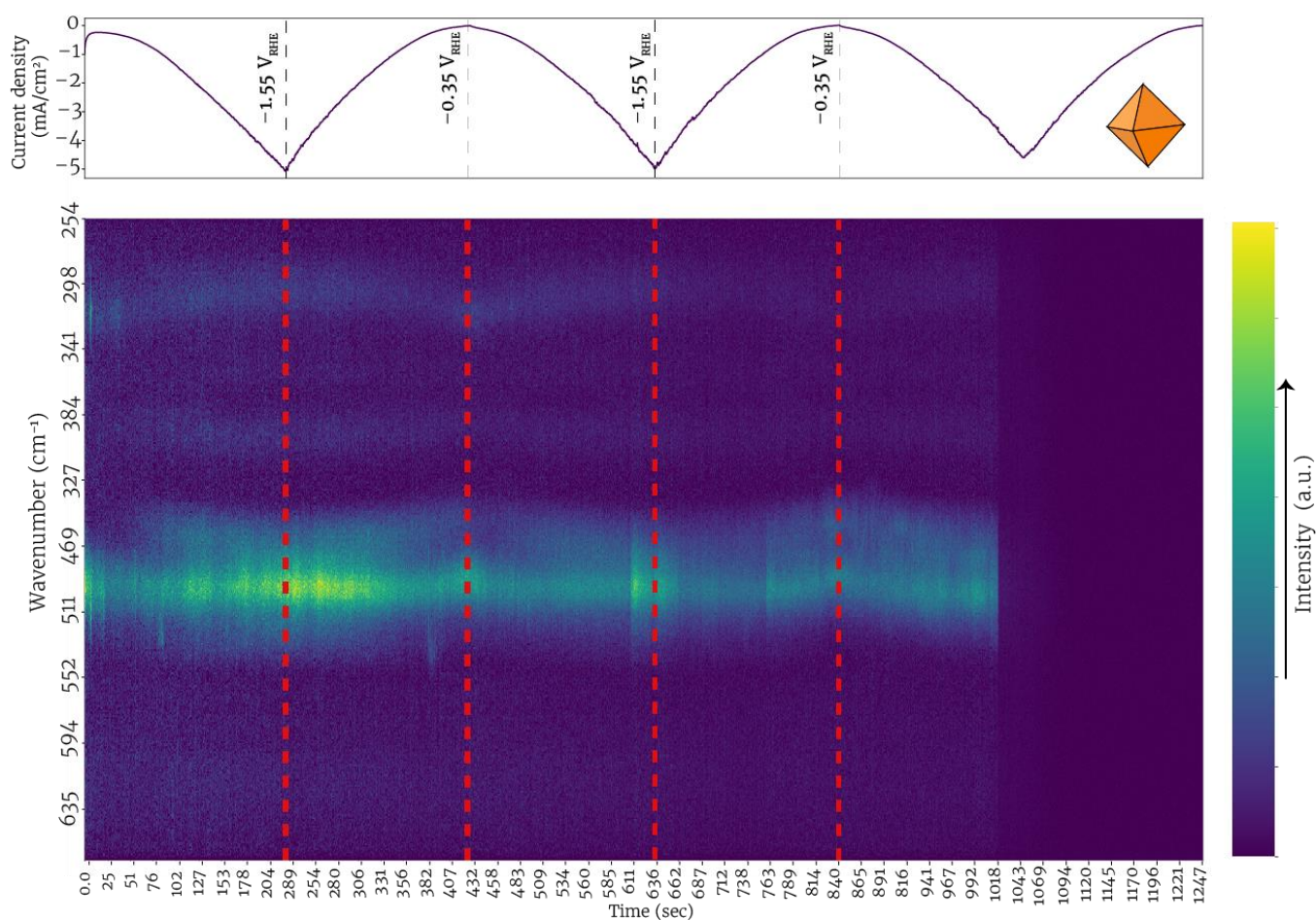
Figure 4.9: Cyclic voltammetry experiment on the octahedrons and an in situ Raman heatmap.
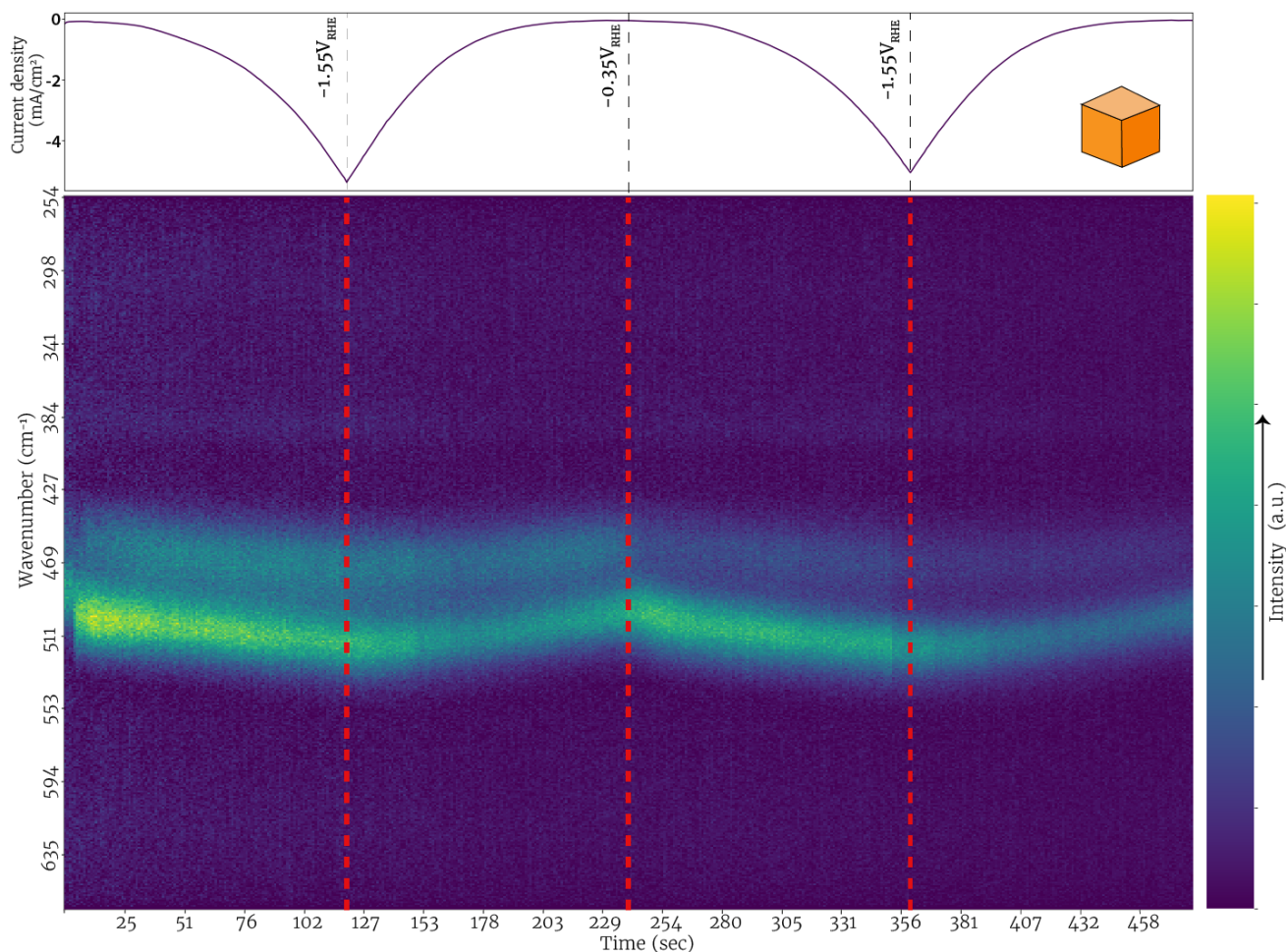
Figure 4.10: Cyclic voltammetry experiment on the cubes and an in situ Raman heatmap

In these experiments it is clear that Stark tuning rates can be observed for the peaks in the metal-adsorbate region. The peaks in the 500 region show a negative tuning rates on both types of particles: this means that their vibrational frequencies move up with increasing cathodic potential. While all the peaks exhibit negative tuning rates, their absolute values differ (Table 4.2). The existence of these negative tuning rates is a novel discovery that has not yet been reported in literature.

For the peaks in the 300 region on the octahedra two different tuning rates can be observed: a positive shift for the 310 cm^{-1} vibration and a negative shift for the 400 cm^{-1}. The peaks in the 300 region for the cubes :the 305 and 340 cm^{-1} vibration which we would expect for the cubes are unexpectedly absent in this experiment. Due to time restrictions the Cyclic voltammetry experiment on the cubes could not be repeated.

Not only the direction of the tuning rates can be determined from this experiment, but also the value. This was done by plotting the Raman spectra at the most and least cathodic potential and using scipy to fit these spectra to Lorentzian functions. The peak position difference of these Lorentzians was consequently divided by the difference in overpotential to yield a tuning rate expressed in cm^{-1} V^{-1}. In Figure 4.11 and 4.12 the fitting of the peaks is visualised. The calculated Stark tuning rate values are summarised in Table 4.2
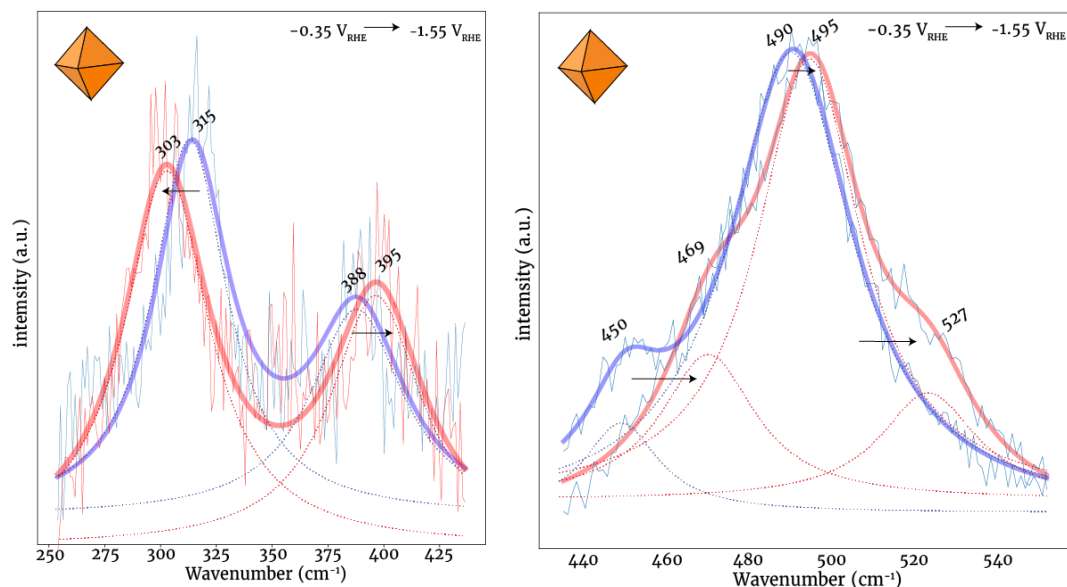
Figure 4.11: Baseline-corrected Raman spectra on the highest and lowest potential in the cyclic voltammetry for the octahedra. The left spectra were fitted using two Lorentzians and the right spectra were fitted using three Lorentzians.
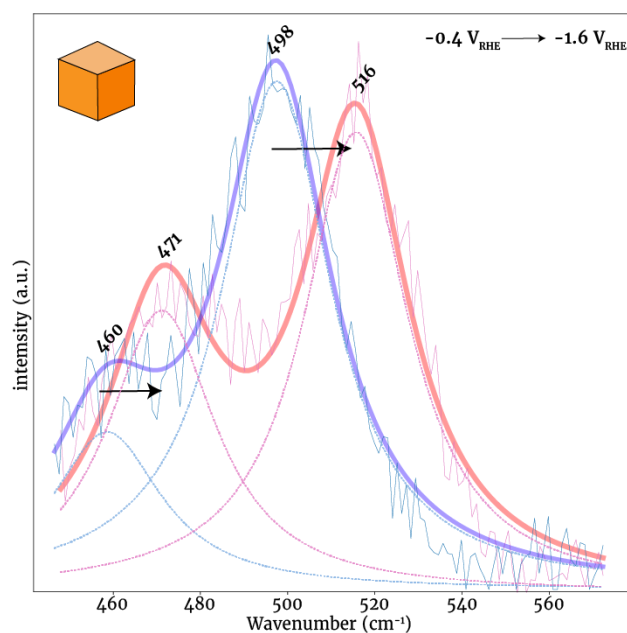
Figure 4.12: Baseline-corrected Raman spectra on the highest and lowest potential in the cyclic voltammetry for the Cubes.

Table 4.2: Observed Stark tuning rates of the peaks in the metal-adsorbate region

Peak position	facet	Tuning rate
310 cm^{-1}	(111)	+10.8 cm^{-1} V^{-1}
400 cm^{-1}	(111)	-8.3 cm^{-1} V^{-1}
460 cm^{-1}	(100)	-9.2 cm^{-1} V^{-1}
460 cm^{-1}	(111)	–13.3 cm^{-1} V^{-1}
500 cm^{-1}	(100)	–15 cm^{-1} V^{-1}
500 cm^{-1}	(111)	-3.3 cm^{-1} V^{-1}

An important thing to note from Table 4.2, is the absence of the Stark shift of the 535 cm⁻¹ peak. The value of stark shift of the 535 peak is difficult to assess, since at the maximum overpotential (-0.35 V_{RHE}) this peak is no longer visible. Which also meant that the no peak was recognised in this area by scipy. It is possible that this peak is swallowed by the 500 peak at lower potentials.

Furthermore it is good to note that the all the peaks in the 500 region show different tuning rates on different facets. This is not surprising, since the Stark effect (and vibrations in general) are heavily dependent on the local environment. The direction of the Stark shift is the same on both facets however, which is important since the direction of the Stark shift can provide information about the structure of the intermediate.

Negative Stark tuning rates have been observed in literature for the v_{M-C} vibrations of linear CO.[26] In the same paper by Zou et al. they observe a positive tuning rate for the v_{C-O} vibrations of linear CO. As explained in the theory section the true nature of the Stark effect is still debated. However one way to explain the opposite sign of both tuning rates is via the chemical binding model[52]: with increasing cathodic potential the metal donates more electron density to the antibonding π^*-orbital (LUMO) of the CO molecule (Fig. 4.13). This backdonation from the metal weakens the bond strength between the carbon and oxygen atom, decreasing its vibrational frequency. The opposite is true for the M-C bond where the donation of filled σ-orbital (HOMO) from C to an empty d-orbital on the metal, increases the bonds strength between the metal and carbon atom, increasing its vibrational frequency. Lambert et al.[53] showed that this explanation is equivalent to the electric field approach as discussed in the theory section. Using this chemical bond theory, we can theorize about the origin of the 310 , 400, 460 and 500 cm⁻¹ peak.
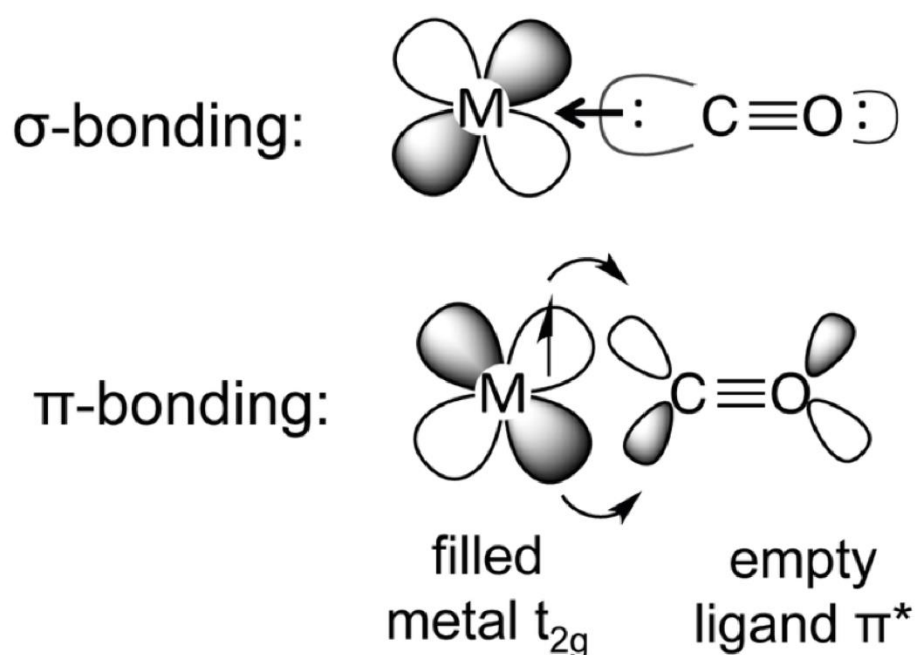
Figure 4.13: Schematic representation of the bonding – back bonding model[54]

Firstly the positive stark tuning rate of the 310 cm^{-1} peak suggests that this vibration does not belong to the v_{M-C} of CO_L, since these vibrations characteristically show a negative stark tuning rate. According to the chemical bond theory this peak belongs to an intermediate which bond strength decreases with increasing potential.

The 400 cm^{-1} peak, which was previously assigned to the v_{M-C} of CO_B, shows a negative tuning rate. Since CO_L and CO_B are the same intermediate, just adsorbed on a different site, similar tuning rates might be expected for v_{M-C} of CO_L and CO_B. This would mean that the experiments in this section could function as an extra argument for this assignment. However calculations have shown that tuning rates are dependent on the adsorption site of the intermediate, this is further explored in chapter 4.5.

The peaks in the 500 region all showed negative Stark tuning rates. If these peaks originate from Metal-adsorbate vibrations, then it would mean that the bond strength between the metal and the adsorbate increases with increasing potential. A possibility is that these are CO-like in the sense that they possess empty π^*-orbitals as LUMO, which can accept electron density from the metal and filled σ-orbital as HOMO that can donate electron density to the metal. Intermediates that have a similar orbital configuration to CO: HCO and COH are candidates that might fit this description. However the peaks in the 500 region cannot be assigned to these intermediates solely based on the Stark shift

In this thesis thus far peaks have been assigned to the vibrational modes of different intermediates on the basis of experimental evidence and different assumptions. Valuable insights were obtained with the conducted experiments, however not enough evidence was obtained to assign peaks with certainty to different intermediates. An overview of the assignments on the basis of the experimental evidence is given in the Table 4.3.

Table 4.3: possible assignments for vibrations and their Stark tuning rates on Cu(100) and Cu(111) on the basis of experimental evidence

Peak position	Facet	Assigned vibration	Stark Tuning Rate
280 cm^{-1}	(111)	V_{bend} CO$_L$	~
305 cm^{-1}	(100)	v_{M-C} CO$_L$	~
310 cm^{-1}	(111)	V_{bend} CO$_B$	+10.8 cm^{-1} V^{-1}
325 cm^{-1}	(111)	v_{M-C} CO$_L$	~
340 cm^{-1}	(100)	v_{M-C} CO$_B$	~
400 cm^{-1}	(111)	v_{M-C} CO$_B$	-8.3 cm^{-1} V^{-1}
460 cm^{-1}	(100), (111)	Ethylene/methane promoting or poisonous species	(100): -9.2 cm^{-1} V^{-1} (111): –13.3 cm^{-1} V^{-1}
500 cm^{-1}	(100),(111)	Ethylene/methane promoting or poisonous species	(100): –15 cm^{-1} V^{-1} (111): -3.3 cm^{-1} V^{-1}
535 cm^{-1}	(100),(111)	Ethylene/methane promoting or poisonous species	inconclusive
1800–1900 cm^{-1}	(100), (111)	v_{C-O} CO$_B$	~
2000-2100 cm^{-1}	(100), (111)	v_{C-O} CO$_L$	~

To strengthen the assignments made until now, DFT calculations can be performed. Using DFT the vibrational modes of different intermediates on the two facets can be calculated. If these calculated vibrational modes are similar to the ones present in the Raman spectra, the assignments made in Table 4.3 become much more certain. In the next section the results of our DFT calculations are shown and the consequences for the assignments discussed.

4.5 DFT vibrations calculations

Overview adsorption sites

The VASP-package allows its users to calculate vibrational modes of molecular adsorbates on metallic slabs in vacuum using DFT. This is very useful in the context of this thesis, as it can act as a check that the previous intermediate assignments do exhibit vibrational modes in the energy-region they are assigned to.

In this section calculations are performed on various on different adsorption sites. In Figure 4.14 an overview of the different adsorption sites on Cu(100) and Cu(111) is provided, with their corresponding codes which are used in the following sections.

① Top site (T)　② Bridge site (B)　③ Fourfold site (F)　④ HCP Threefold Site (T_h)　⑤ FCC Threefold Site (T_f)
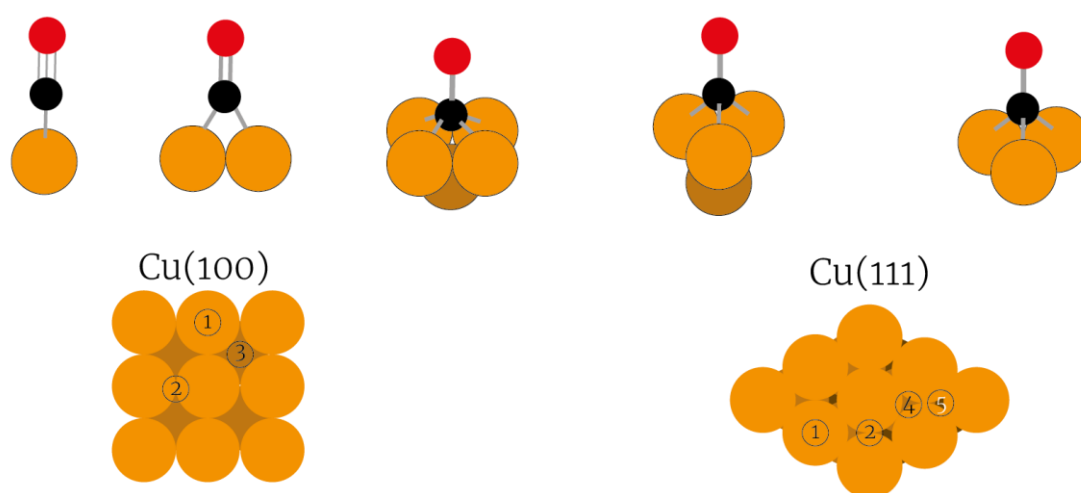
Figure 4.14 an overview of the different adsorption sites on the (100) and (111) facet

Geometry optimisations

The first step in calculating vibrational frequencies of intermediates is the geometry optimisation of the intermediate at different adsorption sites. As explained in previous sections the vibrational modes of a single intermediate can differ vastly in energy depending on its adsorption site. It is therefore important that multiple adsorption sites are investigated for each intermediate.

In view of time, the amount of intermediates used in the calculations is very limited. The CO intermediate is used as it is known to be a vital intermediate in the eCO$_2$RR process. The HCO intermediate, because it is a possible intermediate that can assigned to the 500 region in this thesis. Finally the OH$^-$ intermediate is used in calculations because it has been assigned to the 500 region in literature.

Before discussing the calculated adsorption energies it is important to reiterate that the "true" adsorption energy values differ from the ones calculated here. Firstly, our system is not present in vacuum, but in an aqueous solution with an electrolyte, which influences the adsorption energy. Secondly it is known that an applied potential can have huge consequences for the energy landscape, meaning we should be careful when using

adsorption energies as an argument for a reaction mechanism. That said, trends in adsorption energies can give insights into the energy landscape and function as supporting arguments.

In the Figure 4.15 the adsorption energies for the HCO, CO and OH are plotted for their preferred adsorption site on the (100) and (111) facet. In Figure A6 in the appendix a complete overview of all the optimised geometries is provided.
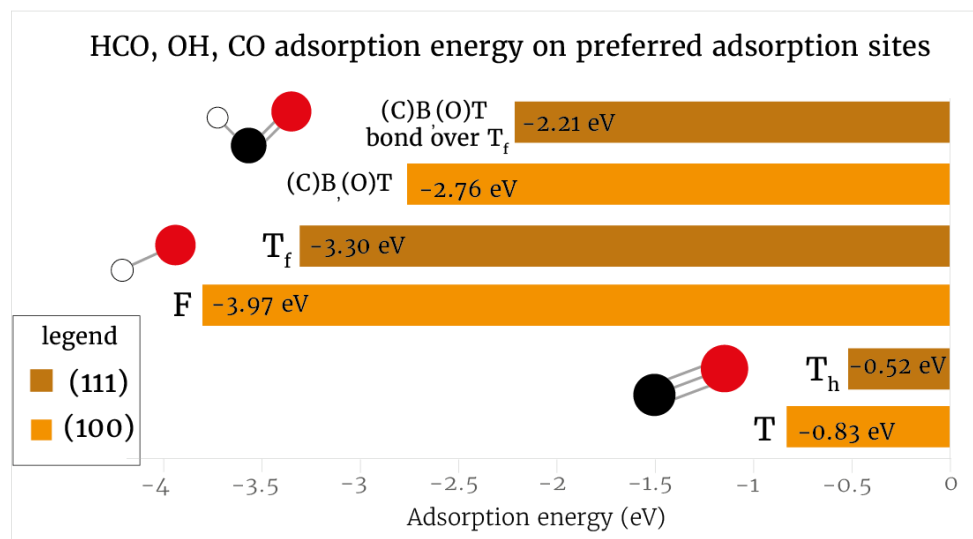
Figure 4.15: Adsorption energies of the HCO, OH and CO intermediate on their preferred adsorption sites on Cu(111) and Cu(100).

For all intermediates the adsorption energy on the cubes is larger than on the octahedra. The fact that the CO intermediate has the top (T) site as its preferred adsorption site on the (100) facet, clashes with previous experimental observations (Fig 4.7), where almost no top-adsorbed (or linear) v_{C-O} modes are observed. However, as explained before, the preferred adsorption site can change depending on the applied potential. In the appendix Figures A6-8 it is shown that the difference in adsorption energy for the different sites on CO is very small, so it is not unthinkable that the preferred adsorption site of CO changes to a B or F site when a potential is applied.

According to the calculations the OH$^-$ intermediate prefers a binding site where the most Cu atoms contribute to the M-O bond on both facets: A T_f site on the octahedra and a F site on the cubes (Appendix, Fig A6-7). For the HCO intermediate it was found that the preferred binding mode is with both the carbon atom as well as the oxygen atom to the metal surface.

Vibrations

The optimized geometries of the previous section were consequently used to calculate the vibrational modes of the corresponding intermediates. The complete result of these calculations is given in the appendix Table A1. In this section the trends from these vibrational modes are discussed.

CO vibrations

In order to discuss the validity of the calculated vibrations, CO_L (= CO_T) might be used as a model system, since the values for the v_{C-O}, the v_{M-C} and v_{bend} are known to be 360, 280 and 2090 cm^{-1} respectively. However, the 360 and 280 cm^{-1} are not present during experiments on neither the cubes or octahedra. Only once the cubes start to deteriorate (lose their morphology), these vibrations would appear in the Raman spectra (see appendix Fig. A8). Therefore it can be concluded that the 360 and 280 vibrations appear only on defect sites and not on the (100) or (111) facet, making them unfit for a direct comparison to the calculated values. It is however reasonable to assume that the calculated v_{C-O}, the v_{M-C} and $v_{bending}$ of CO_L on the (100) and (111) facet should have an energy somewhere close to the aforementioned values measured on pc-Cu, since they are a similarly adsorbed intermediate on the same metal. In Table 4.4 the calculated vibrational modes are tabulated alongside the measured vibrational modes measured on pc-Cu.

Table 4.4: Comparison between the calculated vibrational modes of CO on (100) and (111) and the experimentally measured values on pc-Cu

CO vibrations (cm^{-1})	T (pc-Cu) (exp)	T (100) (calc)	T (111) (calc)	B (100) (calc)	B (111) (calc)	F (100) (calc)	T_f (111) (calc)	T_h (111) (calc)
V_{M-C}	360	393	388	323	326	259	308	315
V_{C-O}	2090	2020	2016	1883	1869	1695	1821	1815
V_{bend}	280	267/274	266/273	293	258	234	227/240	237/244
Δ_{M-b} (V_{M-C} - V_{bend})	60 (med)	126–119 (high)	122–115 (high)	30 (low)	68 (med)	25 (low)	81-68 (med)	78-71 (Med)

The calculated vibrational frequencies of the CO on the Top sites on (100) and (111) , come close to the observed values on pc-Cu. This argues for the validity of the calculated vibrations. However it should be restated that for the comparative analysis between the DFT and experimental results, we are not looking for absolute values but for trends.

In Table 4.4 not only the values of the calculated vibrations are tabulated, but also the difference in energy between the V_{M-C} and V_{bend} mode (Δ_{M-b}). This difference is dependent on the adsorption site of the CO. The Δ_{M-b} value is classified as belonging to one of three different ranges: high (>100), med (50–100) and low (<50). By comparing the difference between peaks in the Raman spectra to these Δ_{M-b} values, peaks can be theoretically assigned to the V_{M-C} and V_{bend} modes of differently adsorbed CO.

The difference between the peaks in the 300 region for the (100) facet is ~37 cm^{-1} (342 – 305). The $\Delta_{Metal-bend}$ on the B and F site closely resembles the peak difference with values of 30 and 25 cm^{-1} respectively. While the absolute values do not line up with the experiment it has been found in literature that especially for the Bridged and Fourfold site the adsorption strength becomes larger with increasing cathodic potential and a stronger adsorption leads to a higher energy v_{M-C}.[48]

The difference between the peaks in the 300 region for the (111) facet is ~70-90 cm^{-1} (395/388 – 315/303). The $\Delta_{Metal-bend}$ on the Bridge and Threefold sites closely resembles this peak difference with values of 68 and 78 cm^{-1} respectively. Which means we might be able to assign the 400 and 310 cm^{-1} peak to the V_{M-C} and V_{bend} of CO$_{Tf}$ respectively.

While the v_{C-O} modes of CO$_L$ are rarely observed for these systems, they are not never present. This is evidenced by figure 4.7 where the Raman spectrum taken at 0 min for the cubes clearly shows a v_{C-O} modes of CO$_L$. If this vibration is observed in the CO-region, the v_{M-C} and $v_{bending}$ of CO$_L$ are to be expected in the 300 region. In this region in only one peak seems to be present: 342 cm^{-1}. Suppose that this vibration is the v_{M-C} of CO$_L$, then on the basis of the calculated $\Delta_{Metal-bend}$ value its corresponding bending vibration should be between 214-222 (340- 126/119). Vibrational modes in this region are however difficult to detect, since there is a lot of background signal at these wavenumbers. Our measurements remain therefore inconclusive about the existence of a v_{bend} vibration at those wavenumbers.

Now that all possible adsorption sites for CO have been assigned for the (100) facet, it is also worthwhile to revisit the experiments on the (111) facet. In the onset potential experiment (Fig. 4.5) and the temporal evolution experiment (Figure 4.7) two peaks are present, which both need a (new) assignment: ~325 cm^{-1} and ~280 cm^{-1}. Their peak difference is ~50 cm^{-1}, which comes close of the calculated $\Delta_{Metal-bend}$ of the CO$_B$ (68 cm^{-1}). If we were to assign the 325 and 275 peak to the V_{M-C} and the V_{bend} of CO$_B$, then the 400 and the 310 peak are the V_{M-C} and V_{bend} of threefold site CO (CO$_{Tf}$).

In the Table below an overview is given of the assignments of the peaks in the 300 region on both the cubes and the octahedra.

Table 4.5: Possible assignments peaks in the 300 cm^{-1} region for the octahedrons and cubes

Peak (cm^{-1})	facet	Vibration type
235	(100)	V_{bend} CO$_L$
275	(111)	V_{bend} CO$_B$
305	(100)	V_{bend} CO$_B$/CO$_F$
310	(111)	V_{bend} CO$_{Tf}$
325	(111)	V_{M-C} CO$_B$
340	(100)	V_{M-C} CO$_B$/CO$_F$ Or V_{M-C} CO$_L$
400	(111)	V_{M-C} CO$_{Tf}$

OH and HCO vibrations: the 500 region

The assignment of peaks in the 300 region to different binding modes of CO begs the question what the origin is of the peaks in the 500 region. The previous chapters suggest that the peaks in the 500 region can be ascribed to intermediates that promote ethylene/methane production (Ch 4.2) and that they perhaps possess a σ-orbital as

HOMO and a π^*-orbital as LUMO (Ch 4.4). One intermediate that fits both these descriptions is HCO. In Chapter 4.3 it was also theorized that the peaks in the 500 region might belong to a poisonous or spectator species, specifically OH$^-$. It is therefore useful to calculate the vibrational modes for these intermediates, to see if these species can be responsible for the peaks in the 500 region. In Table 4.6 and 4.7 an overview of the vibrational modes of HCO and OH on multiple adsorption sites on Cu(111) and Cu(100) is given. A visualisation of the optimized geometries is provided in the appendix Fig A6

Table 4.6: The calculated vibrational modes of HCO on Cu(100) and Cu(111)

HCO	T (100)	T (111)	**BT (100)**	**B, T, over T$_f$ (111)**	B,T over T$_h$ (111)
E_{ads} (eV)	-2.53	-2.12	-2.76	-2.21	-2.18

Vibrations (cm^{-1})	T	T	**BT**	**B, T, over T$_f$**	B,T over T$_h$
$V_{M\text{-adsorbate}}$	427	430	434	429	401
$V_{C\text{-O}}$	1670	1674	1352	1396	1405
$V_{wagging}$	656	676	630	604	589
$V_{sciccoring}$	1181	1186	1243	1235	1227
$V_{C\text{-H}}$	2750	2784	2827	2856	2842
Δ_{M-w} ($V_{wagging}$ - $V_{M\text{-adsorbate}}$)	229	246	196	175	188

Table 4.7: The calculated vibrational modes of OH on Cu(100) and Cu(111)

OH	B (100)	**F (100)**	**T$_f$ (111)**	T$_h$ (111)
E_{ads} (eV)	-3.62	-3.79	-3.30	-3.26

Vibrations (cm^{-1})	B (100)	**F (100)**	**T$_f$ (111)**	T$_h$ (111)
$V_{M\text{-O}}$	433	322	398	397
$V_{O\text{-H}}$	3755	3650	3708	3693
$V_{rocking}$	363	181	264	249
V_{bend}	616	595	455-480	455-471
Δ_{M-b} ($V_{bending}$ - $V_{M\text{-O}}$)	183	273	57-87	58-74

The $V_{M\text{-adsorbate}}$ mode of HCO come close to the experimentally measured 462 cm^{-1} vibration. However if any of the peaks in the 500 region were to be assigned to the $V_{M\text{-adsorbate}}$ of HCO, a peak in the region of ~600-700 cm^{-1} is to be expected as the corresponding $V_{wagging}$ mode on the basis of the Δ_{M-w}. Since neither the ligands nor glassy carbon show vibrational modes in the 600 cm^{-1} region (appendix, Fig. A3), any peaks in this region could function as evidence for the assignment of one of the peaks in the 500 region to the $V_{M\text{-adsorbate}}$ mode of HCO. No peaks can be observed in this region, which would suggest that the peaks in the 500 region do not belong to HCO species. However it could be the case that the $V_{wagging}$ are not-Raman active, meaning that they do occur,

they are just not visible. It it is therefore unclear if the peaks in the 500 region belong to the $V_{\text{M-adsorbate}}$ mode of HCO.

At first glance the $V_{\text{M-O}}$ and the V_{bend} for the OH intermediate come close to the peak positions in the 500 region. Similarly to CO, a Δ_{M-b} analysis could be used to test the validity of the assignment to OH⁻. There are three peaks in the 500 region: ~460, ~500, and ~535 cm⁻¹ each of these peaks could possibly be assigned to either the $V_{\text{M-O}}$ or the V_{bend} of OH⁻.

Using the Δ_{M-b}, it can be theorized that on the (100) facet the peaks in the 500 region cannot belong to $V_{\text{M-O}}$ since that would require peaks between ~600-700 cm⁻¹, which are not present. If the peaks in the 500 region belonged to the V_{bend} mode of OH⁻, peaks around ~250-360 should be present, which correlate with the peaks in the 500 region. A 340 and 305 vibration are present on the (100) facet, so this is a possibility. However it is important to keep in mind that these peaks have been assigned to vibrational modes of CO species prior in this thesis.

This same Δ_{M-b} analysis on the (111) facet is more difficult, since the Δ_{M-b} is much smaller. The 460 peak may belong to the $V_{\text{M-O}}$, of OH with the 535 peak as its corresponding V_{bend}. The 460 peak, according to this analysis, might also belong to the V_{bend} mode of OH and its corresponding $V_{\text{M-O}}$ might then be the 400 cm⁻¹ peak. The Δ_{M-b} analysis does therefore not rule out that the peaks in the 500 region might belong to vibrational modes of OH⁻ on Cu(111). However the OH intermediate does not possess a σ-orbital as HOMO and a π*-orbital as LUMO, but the other way around: a σ*-orbital as LUMO and a π-orbital as HOMO. This might have consequences for the direction of the Stark shift of the OH intermediate.

In the next section the direction of the Stark shifts for different intermediates are calculated and the consequences for the assignments discussed.

Stark shifts

Starks shifts were calculated by placing a single molecule on a molecular slab. Three different molecular dynamics calculations were carried out for this system: one where no potential was applied, one were a positive potential was applied, one were a negative potential was applied. The goal of these calculations was to calculate the direction of the Stark shift, not the absolute value. The reason for this was that it was unclear how the applied potential relates to the local electric field. However, the sign of the electric field was clear, which made the direction of the Stark shift also clear.

CO_L might be used as a model system for the Stark shift calculations, since the directions of its stark shifts are known:[26] a negative shift for the $v_{\text{M-C}}$ and a positive shift for the $v_{\text{C-O}}$ In Table 4.8 the calculated vibrations at the different applied potentials for linear CO on Cu(100) and Cu(111) are shown. Note that the vibrations where no potential was applied differ from the calculated values in the previous sections, this is due to the fact that a different program was used to carry out the calculations. A different program was needed due to the fact that VASP is periodic in all dimensions, but in order to apply a static electric field the program needed to be periodic in all dimensions except the dimension in which

the electric field was applied. GPAW was therefore used to carry out the Stark shift calculations.

Table 4.8: Calculated Stark shifts for CO$_L$ on the (100) and the (111) facet

CO$_L$	(100) 0	(100) + (↑)	(100) - (↓)	(111) 0	(111) +(↑)	(111) - (↓)
V$_{M-C}$	397.6	370.6 ↓	404.1 ↑	393	385 ↓	415 ↑
V$_{C-O}$	2027	2079 ↑	1967 ↓	2031	2076 ↑	1984 ↓
V$_{bend}$	297.2	293.4 ↓	312 ↑	336	286 ↓	347 ↑

The directions of the shifts for the V$_{M-C}$ and the V$_{C-O}$ are identical to the directions found in literature: negative and positive respectively. The V$_{bend}$, however has not been observed to shift.[20] A possible explanation for this could be that the bending vibration occurs in all directions, and is consequently cancelled out. Another explanation could be that, as discussed in earlier sections, the CO$_L$ measured by De Ruiter et al.[20] is not present on the (100) or (111) but on another facet and the direction of the shift of the bending vibration is facet dependent. The model system shows that we are capable of calculating the direction of the Stark shift accurately. These type of calculations could be used as a check that vibrations are assigned correctly.

Table 4.9: Calculated Stark shifts for OH and HCO on the (100) and the (111) facet

OH	(100) 0	(100) + (↑)	(100) - (↓)	(111) 0	(111) + (↑)	(111) - (↓)
V$_{M-O}$	323	346 ↑	276 ↓	391	390 ~	345 ↓
V$_{O-H}$	3636	3629 ↓	3609 ↓	3696	3676 ↓	3689 ↓
V$_{bending}$	505	641 ↑	374 ↓	418.6	467 ↑	380 ↓

HCO	(100) 0	(100) + (↑)	(100) - (↓)	(111) 0	(111) + (↑)	(111) - (↓)
V$_{M-adsorbate}$	377	456 ↑	448 ↑	366	422 ↑	390 ↑
V$_{C-O}$	1374	1388 ↑	1322 ↓	1431	1456 ↑	1404 ↓
V$_{wagging}$	529	522 ↓	546 ↑	436	550 ↑	475 ↑
V$_{sciccoring}$	1176	1153 ↓	1162 ↓	1161	1151 ↓	1162 ~
V$_{C-H}$	2799	2829 ↑	2736 ↓	2828	2866 ↑	2766 ↓

The V$_{M-O}$ and V$_{bending}$ of OH$^-$ both possess a positive stark tuning rate, while the tuning rate observed for the peaks in the 500 region is negative. This means that these peaks do not belong to a chemisorbed OH intermediate, because the direction of the stark shifts do not align.

The conclusions that can be made on the basis of the calculated HCO vibrations are much less straightforward. The vibrations in the ~500 region (V$_{M-adsorbate}$, V$_{wagging}$) exhibit both a negative and a positive stark tuning rate: independent of the sign of the electric field these vibrations increase in energy. This suggests that the interaction of these vibrations with

the electric field is more complex than the relatively simple bonding-back bonding theory that was discussed before. There might not even be a linear dependence in this case. This makes it difficult to make conclusions on the basis of these calculated shifts.

In the experiments where the Stark tuning rate was observed, the potential remained negative, as a positive overpotential would result in the formation of CuO. Not only the Cu surface would be oxidized at positive potentials, but also the intermediates that are present on the surface. It is therefore impossible to the best of my knowledge to observe the stark tuning rates for most intermediates under oxidizing (positive) potentials.

The $V_{wagging}$ and $V_{M-adsorbate}$ of the HCO intermediate do show a negative tuning rate under a negative potential. The peaks in the 500 region might therefore be ascribed to the HCO intermediate on the basis of their tuning rate, however the $\Delta_{Metal-bend}$ in the previous section does exclude HCO as a possible intermediate.

It is also useful to check to see if the assignments of the peaks in the 300 region hold true on the basis of their observed Stark shift and the calculated Stark shift.

In section 4.3 two Stark shifts are observed in the 300 region of the (111) facet: a positive Stark shift for the 310 peak and a negative Stark shift for the 400 peak. This peaks have been ascribed to a V_{bend} and a V_{M-C} vibration of $CO_{Tf/h}$ respectively.

Table 4.10: Calculated Stark tuning rate for CO$_{Tf/h}$ on the (111) facet

	T_f	T_f	T_f	T_h	T_h	T_h
CO	0	+ (↑)	- (↓)	0	+ (↑)	- (↓)
V_{M-C}	314	311 ↓	316 ↑	320	311 ↓	314 ↓
V_{C-O}	1829	1905 ↑	1772 ↓	1823	1897 ↑	1786 ↓
V_{bend}	201	215 ↑	206 ↑	252	211 ↓	287 ↑

For the CO$_{Tf}$ the V_{M-C} does exhibit a negative Stark shift, the bend vibration however always shifts up independent of the direction of the applied electric field. The reason for this behaviour is unclear. The conclusion about the assignment to these peaks as belonging to CO$_{Tf}$ is therefore inconclusive.

It should be noted that the T_h V_{M-C} vibration behaves unexpectedly: the energy of this vibration becomes lower independent of the sign of the applied electric field. We expect that this is an outlier, as all the V_{M-C} vibrations on all other facets and all their adsorption sites show a negative stark tuning rate (Appendix, Table A2&3).

Summary

Combining experimental evidence and DFT calculations several Raman peaks have been assigned to various vibrations of different intermediates. The peaks in the 300 region, were assigned to the v_{bend} and v_{M-C} of CO_B on the cubes and to the v_{bend} and v_{M-C} of CO_{Tf} on the octahedrons. These assignments have a consequence for the reaction mechanism of eCO_2RR. They suggest that the dimerization pathways on both the cubes and the octahedrons include at least one multiple bound CO molecule, since that appears to be the only site at which the CO intermediate is stabilized.

The assignments for the peaks in the 500 region is inconclusive. On the basis of the calculated and observed stark tuning rate, the OH^- intermediate could be excluded as possible origin. While the experimental data suggested that peaks in this region could be ascribed to a HCO intermediate, the calculations remained unclear about this assignment. Other assignments are imaginable to the peaks in this region: COH*, or OCCOH*, which are further explored in the outlook section (Ch 6). In Figure 4.16 an overview of the reaction pathways on Cu(111) and Cu(100) on the basis of the literature, experiments and calculations is given, along with the observed vibrations.

Proposed dimerization pathways on Cu(111) and Cu(100)

v_{bend} = 305 cm^{-1}
v_{M-C} = 340 cm^{-1}

(100)

v_{bend} = 310 cm^{-1}
v_{M-C} = 400 cm^{-1}

+ CO_B

or

+ H^+ + e^-

*$v_{M-adsorbate}$ = 460 cm^{-1}

+ H^+ + e^-

*$v_{M-adsorbate}$ = 460 cm^{-1}

+ H^+ + e^-

+ CO_B

+ CO_{Tf}

*$v_?$ = 460/500/535 cm^{-1}

(111)

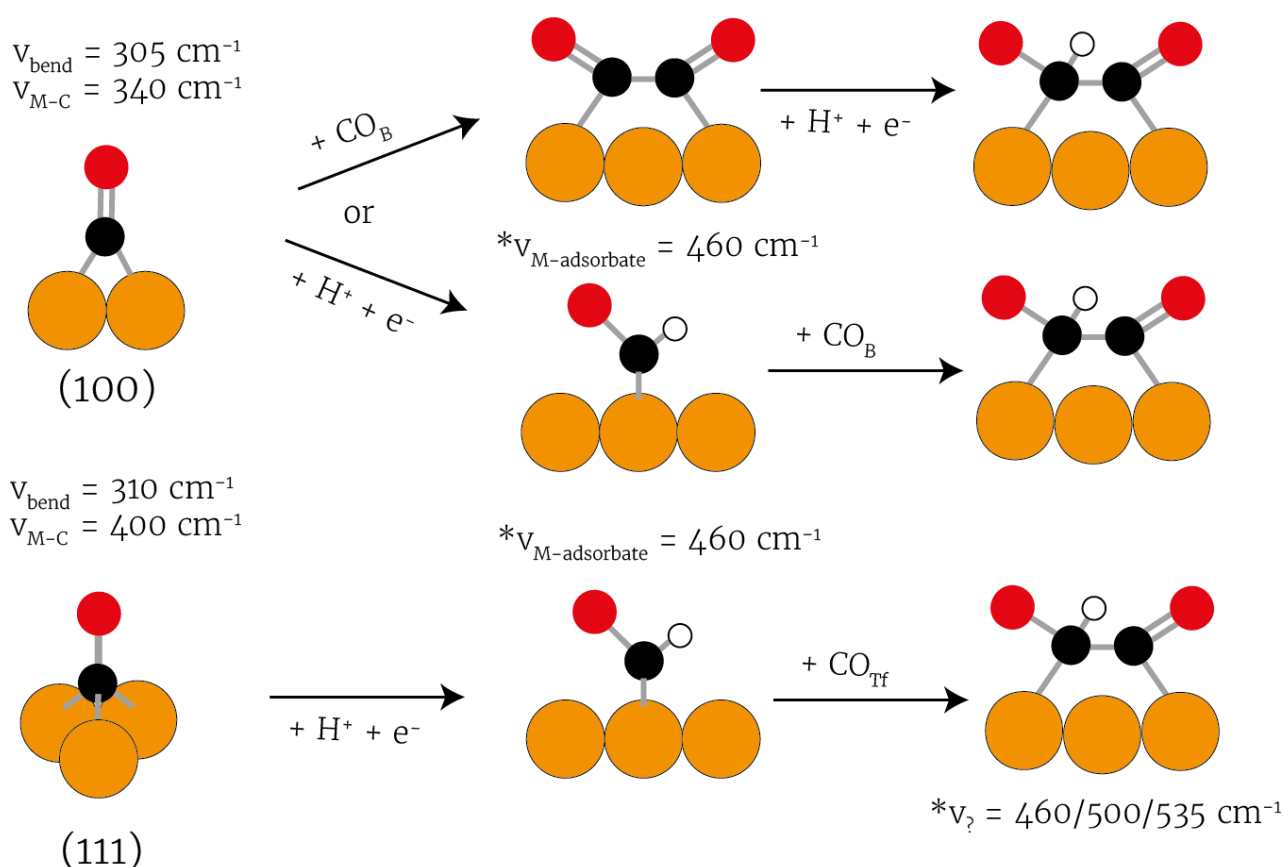*Figure 4.16: Overview of the proposed dimerization pathways on Cu(111) and Cu(100), the vibrations with an asterisks are uncertain*

5. Conclusions

This thesis describes a spectroscopic study on the reaction mechanism of the electrochemical CO_2 reduction reaction, using single facetted Cu nanoparticles as the catalyst. Nano octahedrons, and nano cubes which have the (111) and (100) facet exposed .These particles were consequently used to make single facet Cu electrodes, by drop casting a solution of them on glassy carbon and drying it overnight under inert atmosphere.

The *in situ* Raman signal was revealed to be facet dependent: the 400 cm^{-1} was unique for the (111) facet and the ~340 cm^{-1} was unique for the (100) facet. However most vibrations were present on both facets, such as the vibrations in the 500 region.

Potential dependent Raman experiments revealed a triplet of peaks: ~460, ~495 & ~535 cm^{-1}, which are present on both facets. These peaks appeared to be absent at overpotentials which lie under the onset potentials for CH_4 and C_2H_4 , suggesting that these peaks might be related to the formation of these products. Time dependant experiments revealed that these peaks increase in intensity overtime. This temporal behaviour was linked to the increase of C_2H_4 and CH_4 in the first hour of the reaction which has been observed in literature, to further argue for the assignment of these peaks to CH_4/C_2H_4 promoting species. However the temporal behaviour was also argued to be evidence of poisonous/spectator species.

During cyclic voltammetry experiments it was clear that the peaks in the metal-adsorbate region exhibited Stark shifts. The peaks in the 500 region showed a negative Stark tuning rate on both the cubes as well as the octahedrons. The 400 peak on the octahedrons also exhibited a negative shift, but for the 310 peak a positive tuning rate was observed. Unfortunately, experiments that attempted to reveal the tuning rate of the peaks in the 300 region on the cubes failed. On the basis of the direction of the shift, it was theorized that the peaks in the 500 region might possess a σ-orbital as HOMO and a π^*-orbital as LUMO, similar to CO. The direction of the shift of the 310 peak was evidence of this peak not belonging to a v_{M-C} vibration, since these vibrations characteristically show a negative tuning rate.

Exploratory DFT calculations were carried out to see if the assignments based on the experiments were able to hold their ground. CO, HCO and OH were placed on different adsorption sites on the (100) and (111) facet and their adsorption energies were calculated. The most favoured adsorption sites on each facet, were then used to calculate the vibrational modes for HCO and OH. For CO the vibrational modes were calculated on all adsorption sites on both facets. On the basis of the difference in energy for the bend and M-adsorbate vibration the peaks in the 300 region and the 400 peak were assigned to vibrational modes of bridge or multiple bound CO. Furthermore, the same analysis done for HCO and OH remained inconclusive over the fact that the peaks in the 500 region could be ascribed to these intermediates.

DFT calculations were also carried out to calculate the direction of the Stark shifts of different intermediates. These calculations revealed that the M-O and bending vibration of the OH intermediate show a positive Stark shift, which reveiled that the peaks in the 500 region do not belong to OH$^-$. For the HCO intermediate, the vibrations of interest did show a negative tuning rate, similar to the ones in the 500 region. Finally the calculated Stark shift was used to confirm the assignment of the 310 and the 400 peak on the octahedrons towards the v_{bend} and v_{M-C} of CO$_{Tf}$, however the result of the Stark shift calculation remained inconclusive.

It was shown with HR-SEM that the particles retained their morphology after the pre-treatment and mostly retained it after 1 hour of electrocatalysis. A cyclic voltammetry program was found to have a bigger influence on the stability of the nanoparticle electrode, leading to a higher degree of degradation. It was also shown with TEM analysis that the particles degraded over time on the shelf. The absence of a 360 and 280 peak could be used as an indication of particle stability, as these vibrations occur only on defect sites and not on the (100) or (111) facet. The fact that the 360 and 280 vibration were absent on the measured Raman spectra lead to the conclusion that the vibrations that were measured during *in situ* Raman spectroscopy experiments were vibrations on well-defined (100) and (111) facets, containing little defect sites.

The goal of this thesis was to elucidate the mechanism of the eCO$_2$RR on Cu (100) and Cu(111) facet. On the basis of the assignment of the peaks in the 300 region, it can be concluded that the dimerization of carbon based intermediates, probably occurs between a bridged or multiple bound CO (not a linear CO species) and another carbon based intermediate on Cu(100) and Cu(111), such as CO, HCO or COH. The peaks in the 500 region might belong to either another carbon based intermediate, or a dimer.

6. Outlook

In this thesis, the in *situ* Raman signal on Cu nano cubes and octahedra are compared and in *silico* DFT experiments were carried out in order to assign peaks to the vibrational modes of different intermediates. The assignments which are made are however not final, more experiments (both *in situ* and *in silico*) need to be done to be more certain of the assignment of the different peaks. Further, the origin of the peaks in the 500 region remain unknown.

Since we are able to calculate the direction of the Stark shift, more intermediates should be tested to see if the direction of their Stark shifts lines up with the tuning rate observed for the peaks in the 500 region. Especially the hydrogenated dimer (OCCOH*), mentioned in the introduction should be used for Stark shift calculations, as Pérez-Gallent et al.[38] claim to have found spectroscopic evidence for this intermediate using FTIR. If calculations show that this intermediate also has vibrations in the ~500 cm^{-1} region and that these vibrations show a negative Stark shift, it might solve the question on the elusive 500 vibrations. Another intermediate that could be of interest is the *COH intermediate, as it is mentioned in literature as the possible first reduced intermediate after CO alongside with *HCO.

It is also important that the cyclic voltammetry experiment on the nano cubes is repeated in order to find the tuning rates In the 300 region. The direction of these tuning rates might then function as another argument for the assignments made in this thesis.

For this thesis, onset potential values for different products were taken from literature. It would be more accurate to find the onset values for this system specifically by making use of more sensitive techniques such as differential electrochemical mass spectrometry (DEMS) or online electrochemical mass spectrometry (OLEMS). This would help in finding a more accurate relationship between overpotential and product formation which would ultimately aid in determining more correct links between Raman peaks and certain products. For the most accurate relationship between the reaction product and Raman signal, operando measurements should be carried out. During operando measurements spectroscopic information is gained simultaneously with activity information.

It is important to be certain that the particles and the exposed facet remain stable during *in situ* Raman measurements, so that any peaks can be assigned to a specific facet with certainty. Because of the low loading of the catalyst, ex situ grazing incidence XRD (GI-XRD) is the best bet for observing any possible change in exposed facet. Since normal XRD measurements suffer from poor signal to noise ratio due to a lot of background signal from the glassy carbon substrate.

Finally labelling experiments with C^{13} and O^{17} could be carried out to see if the peaks measured are carbon or oxygen related. If peaks shift in energy when only the isotope is present in the system, it could be concluded that the intermediate responsible for this vibration contains at least one atom of this isotope.

7. References

(1)   IPCC. *Sixth Assessment Report, Climate Change 2022: Mitigation of Climate Change*; 2021.

(2)   Minx, J. C.; et al. A Comprehensive and Synthetic Dataset for Global, Regional, and National Greenhouse Gas Emissions by Sector 1970–2018 with an Extension to 2019. *Earth Syst. Sci. Data* **2021**, *13*, 5213–5252,. https://doi.org/https://doi.org/10.5194/essd-13-5213-2021.

(3)   Artz, J.; Müller, T. E.; Thenert, K.; Kleinekorte, J.; Meys, R.; Sternberg, A.; Bardow, A.; Leitner, W. Sustainable Conversion of Carbon Dioxide: An Integrated Review of Catalysis and Life Cycle Assessment. *Chem. Rev.* **2018**, *118* (2), 434–504. https://doi.org/10.1021/acs.chemrev.7b00435.

(4)   Whipple, D. T.; Kenis, P. J. A. Prospects of CO2 Utilization via Direct Heterogeneous Electrochemical Reduction. *J. Phys. Chem. Lett.* **2010**, *1* (24), 3451–3458. https://doi.org/10.1021/jz1012627.

(5)   Britannica, T. E. of E. Electrochemistry. Encyclopedia Britannica. **2016**.

(6)   Nitopi, S.; Bertheussen, E.; Scott, S. B.; Liu, X.; Engstfeld, A. K.; Horch, S.; Seger, B.; Stephens, I. E. L.; Chan, K.; Hahn, C.; Nørskov, J. K.; Jaramillo, T. F.; Chorkendorff, I. Progress and Perspectives of Electrochemical CO2 Reduction on Copper in Aqueous Electrolyte. *Chem. Rev.* **2019**, *119* (12), 7610–7672. https://doi.org/10.1021/acs.chemrev.8b00705.

(7)   Koolmeijer, K. The Electrocatalytic Reduction of CO2 on Cu and Ag Based Nanoparticle Electrodes, Utrecht University, 2021.

(8)   Hori, Y. K.; Katsuhei SUZUKI, S. Production of CO and CH4 in Electrochemical Reduction of CO2 at Metal Electrodes in Aqueous Hydrogencarbonate Solution. *Chem. Lett.* **1985**, 1695–1698. https://doi.org/https://doi.org/10.1246/cl.1985.1695.

(9)   Bagger, A.; Ju, W.; Varela, A. S.; Strasser, P.; Rossmeisl, J. Electrochemical CO2 Reduction: A Classification Problem. *ChemPhysChem* **2017**, *18* (22), 3266–3273. https://doi.org/10.1002/cphc.201700736.

(10)   Hori, Y.; Murata, A.; Takahashi, R. Formation of Hydrocarbons in the Electrochemical Reduction of Carbon Dioxide at a Copper Electrode in Aqueous Solution. *J. Chem. Soc. Faraday Trans. 1 Phys. Chem. Condens. Phases* **1989**, *85* (8), 2309–2326. https://doi.org/10.1039/F19898502309.

(11)   Goodpaster, J. D.; Bell, A. T.; Head-Gordon, M. Identification of Possible Pathways for C-C Bond Formation during Electrochemical Reduction of CO2: New Theoretical Insights from an Improved Electrochemical Model. *J. Phys. Chem. Lett.* **2016**, *7* (8), 1471–1477. https://doi.org/10.1021/acs.jpclett.6b00358.

(12)   Hussain, J.; Skúlason, E.; Jónsson, H. Computational Study of Electrochemical CO2 Reduction at Transition Metal Electrodes. *Procedia Comput. Sci.* **2015**, *51* (1),

1865–1871. https://doi.org/10.1016/j.procs.2015.05.419.

(13)   Ou, L. Chemical and Electrochemical Hydrogenation of CO2 to Hydrocarbons on Cu Single Crystal Surfaces: Insights into the Mechanism and Selectivity from DFT Calculations. *RSC Adv.* **2015**, *5* (71), 57361–57371. https://doi.org/10.1039/c5ra09294a.

(14)   Hori, Y.; Takahashi, I.; Koga, O.; Hoshi, N. Electrochemical Reduction of Carbon Dioxide at Various Series of Copper Single Crystal Electrodes. *J. Mol. Catal. A Chem.* **2003**, *199* (1–2), 39–47. https://doi.org/10.1016/S1381-1169(03)00016-5.

(15)   Peterson, A. A.; Abild-Pedersen, F.; Studt, F.; Rossmeisl, J.; Nørskov, J. K. How Copper Catalyzes the Electroreduction of Carbon Dioxide into Hydrocarbon Fuels. *Energy Environ. Sci.* **2010**, *3* (9), 1311–1315. https://doi.org/10.1039/c0ee00071j.

(16)   Xiao, C.; Zhang, J. Architectural Design for Enhanced C2Product Selectivity in Electrochemical CO2Reduction Using Cu-Based Catalysts: A Review. *ACS Nano* **2021**, *15* (5), 7975–8000. https://doi.org/10.1021/acsnano.0c10697.

(17)   Sun, Z.; Ma, T.; Tao, H.; Fan, Q.; Han, B. Fundamentals and Challenges of Electrochemical CO 2 Reduction Using Two-Dimensional Materials. *CHEMPR* **2017**, *3* (4), 560–587. https://doi.org/10.1016/j.chempr.2017.09.009.

(18)   Bhatt, V. Thermodynamics and Kinetics of Complex Formation. In *essentials of coordination chemistry*; 2016; pp 111–137. https://doi.org/https://doi.org/10.1016/B978-0-12-803895-6.00004-5.

(19)   Atkins, P.; De Paula, J.; Keeler, J. *Physical Chemistry*, 11th editi.; 2018.

(20)   De Ruiter, J.; An, H.; Wu, L.; Gijsberg, Z.; Yang, S.; Hartman, T.; Weckhuysen, B. M.; Van Der Stam, W. Probing the Dynamics of Low-Overpotential CO2-to-CO Activation on Copper Electrodes with Time-Resolved Raman Spectroscopy. *J. Am. Chem. Soc.* **2022**, *144* (33), 15047–15058. https://doi.org/10.1021/jacs.2c03172.

(21)   Debbichi, L.; Marco De Lucas, M. C.; Pierson, J. F.; Krüger, P. Vibrational Properties of CuO and Cu 4O 3 from First-Principles Calculations, and Raman and Infrared Spectroscopy. *J. Phys. Chem. C* **2012**, *116* (18), 10232–10237. https://doi.org/10.1021/jp303096m.

(22)   Zhao, Y.; Chang, X.; Malkani, A. S.; Yang, X.; Thompson, L.; Jiao, F.; Xu, B. Speciation of Cu Surfaces during the Electrochemical CO Reduction Reaction. *J. Am. Chem. Soc.* **2020**, *142* (21), 9735–9743. https://doi.org/10.1021/jacs.0c02354.

(23)   Jiang, S.; D'Amario, L.; Dau, H. Copper Carbonate Hydroxide as Precursor of Interfacial CO in CO2 Electroreduction. *ChemSusChem* **2022**, *15* (8), 1–13. https://doi.org/10.1002/cssc.202102506.

(24)   Baiz, C. R.; Błasiak, B.; Bredenbeck, J.; Cho, M.; Choi, J. H.; Corcelli, S. A.; Dijkstra, A. G.; Feng, C. J.; Garrett-Roe, S.; Ge, N. H.; Hanson-Heine, M. W. D.; Hirst, J. D.; Jansen, T. L. C.; Kwac, K.; Kubarych, K. J.; Londergan, C. H.; Maekawa, H.; Reppert, M.; Saito, S.; Roy, S.; Skinner, J. L.; Stock, G.; Straub, J. E.; Thielges, M. C.; Tominaga, K.; Tokmakoff, A.; Torii, H.; Wang, L.; Webb, L. J.; Zanni, M. T. Vibrational

Spectroscopic Map, Vibrational Spectroscopy, and Intermolecular Interaction. *Chem. Rev.* **2020**, *120* (15), 7152–7218. https://doi.org/10.1021/acs.chemrev.9b00813.

(25) Bhattacharyya, D.; Videla, P. E.; Cattaneo, M.; Batista, V. S.; Lian, T.; Kubiak, C. P. Vibrational Stark Shift Spectroscopy of Catalysts under the Influence of Electric Fields at Electrode-Solution Interfaces. *Chem. Sci.* **2021**, *12* (30), 10131–10149. https://doi.org/10.1039/d1sc01876k.

(26) Zou, S.; Weaver, M. J. Potential-Dependent Metal-Adsorbate Stretching Frequencies for Carbon Monoxide on Transition-Metal Electrodes: Chemical Bonding versus Electrostatic Field Effects. *J. Phys. Chem.* **1996**, *100* (10), 4237–4242. https://doi.org/10.1021/jp9533178.

(27) Mamatkulov, M.; Filhol, J. S. An Ab Initio Study of Electrochemical vs. Electromechanical Properties: The Case of CO Adsorbed on a Pt(111) Surface. *Phys. Chem. Chem. Phys.* **2011**, *13* (17), 7675–7684. https://doi.org/10.1039/c0cp01444c.

(28) Hori, Y.; Takahashi, R.; Yoshinami, Y.; Murata, A. Electrochemical Reduction of CO at a Copper Electrode. *J. Phys. Chem. B* **1997**, *101* (36), 7075–7081. https://doi.org/10.1021/jp970284i.

(29) Wang, L.; Nitopi, S. A.; Bertheussen, E.; Orazov, M.; Morales-Guio, C. G.; Liu, X.; Higgins, D. C.; Chan, K.; Nørskov, J. K.; Hahn, C.; Jaramillo, T. F. Electrochemical Carbon Monoxide Reduction on Polycrystalline Copper: Effects of Potential, Pressure, and PH on Selectivity toward Multicarbon and Oxygenated Products. *ACS Catal.* **2018**, *8* (8), 7445–7454. https://doi.org/10.1021/acscatal.8b01200.

(30) An, H.; Wu, L.; Mandemaker, L. D. B.; Yang, S.; de Ruiter, J.; Wijten, J. H. J.; Janssens, J. C. L.; Hartman, T.; van der Stam, W.; Weckhuysen, B. M. Sub-Second Time-Resolved Surface-Enhanced Raman Spectroscopy Reveals Dynamic CO Intermediates during Electrochemical CO2 Reduction on Copper. *Angew. Chemie - Int. Ed.* **2021**, *60* (30), 16576–16584. https://doi.org/10.1002/anie.202104114.

(31) Chernyshova, I. V.; Somasundaran, P.; Ponnurangam, S. On the Origin of the Elusive First Intermediate of CO2 Electroreduction. *Proc. Natl. Acad. Sci. U. S. A.* **2018**, *115* (40), E9261–E9270. https://doi.org/10.1073/pnas.1802256115.

(32) Durand, W. J.; Peterson, A. A.; Studt, F.; Abild-Pedersen, F.; Nørskov, J. K. Structure Effects on the Energetics of the Electrochemical Reduction of CO2 by Copper Surfaces. *Surf. Sci.* **2011**, *605* (15–16), 1354–1359. https://doi.org/10.1016/j.susc.2011.04.028.

(33) Akhade, S. A.; Luo, W.; Nie, X.; Asthagiri, A.; Janik, M. J. Theoretical Insight on Reactivity Trends in CO2 Electroreduction across Transition Metals. *Catal. Sci. Technol.* **2016**, *6* (4), 1042–1053. https://doi.org/10.1039/c5cy01339a.

(34) Schouten, K. J. P.; Qin, Z.; Gallent, E. P.; Koper, M. T. M. Two Pathways for the Formation of Ethylene in CO Reduction on Single-Crystal Copper Electrodes. *J. Am. Chem. Soc.* **2012**, *134* (24), 9864–9867. https://doi.org/10.1021/ja302668n.

(35)   Xiao, H.; Cheng, T.; Goddard, W. A.; Sundararaman, R. Mechanistic Explanation of the PH Dependence and Onset Potentials for Hydrocarbon Products from Electrochemical Reduction of CO on Cu (111). *J. Am. Chem. Soc.* **2016**, *138* (2), 483–486. https://doi.org/10.1021/jacs.5b11390.

(36)   Garza, A. J.; Bell, A. T.; Head-Gordon, M. Mechanism of CO2 Reduction at Copper Surfaces: Pathways to C2 Products. *ACS Catal.* **2018**, *8* (2), 1490–1499. https://doi.org/10.1021/acscatal.7b03477.

(37)   Zhan, C.; Dattila, F.; Rettenmaier, C.; Bergmann, A.; Kühl, S.; García-Muelas, R.; López, N.; Roldan Cuenya, B. Revealing the CO Coverage-Driven C-C Coupling Mechanism for Electrochemical CO2Reduction on Cu2O Nanocubesvia OperandoRaman Spectroscopy. *ACS Catal.* **2021**, *11* (13), 7694–7701. https://doi.org/10.1021/acscatal.1c01478.

(38)   Pérez-Gallent, E.; Figueiredo, M. C.; Calle-Vallejo, F.; Koper, M. T. M. Spectroscopic Observation of a Hydrogenated CO Dimer Intermediate During CO Reduction on Cu(100) Electrodes. *Angew. Chemie* **2017**, *129* (13), 3675–3678. https://doi.org/10.1002/ange.201700580.

(39)   Iyengar, P.; Huang, J.; De Gregorio, G. L.; Gadiyar, C.; Buonsanti, R. Size Dependent Selectivity of Cu Nano-Octahedra Catalysts for the Electrochemical Reduction of CO2 to CH4. *Chem. Commun.* **2019**, *55* (60), 8796–8799. https://doi.org/10.1039/c9cc02522g.

(40)   Loiudice, A.; Lobaccaro, P.; Kamali, E. A.; Thao, T.; Huang, B. H.; Ager, J. W.; Buonsanti, R. Tailoring Copper Nanocrystals towards C2 Products in Electrochemical CO2 Reduction. *Angew. Chemie - Int. Ed.* **2016**, *55* (19), 5789–5792. https://doi.org/10.1002/anie.201601582.

(41)   If, C. G. R.; Clayton, E.; Griffin, W. L.; Sie, S. H.; I, D. C. SNIP, a Statistics-Sensitive Background Treatment for the Quantitative Analysis of PIXE Spectra in Geoscience Applications. *Nucl. Instruments Methods Phys. Res. Sect. B Beam Interact. with Mater. Atoms* **1988**, *34* (3), 396–402. https://doi.org/https://doi.org/10.1016/0168-583X(88)90063-8.

(42)   Huang, Y.; Handoko, A. D.; Hirunsit, P.; Yeo, B. S. Electrochemical Reduction of CO2 Using Copper Single-Crystal Surfaces: Effects of CO∗ Coverage on the Selective Formation of Ethylene. *ACS Catal.* **2017**, *7* (3), 1749–1756. https://doi.org/10.1021/acscatal.6b03147.

(43)   Roberts, F. S.; Kuhl, K. P.; Nilsson, A. High Selectivity for Ethylene from Carbon Dioxide Reduction over Copper Nanocube Electrocatalysts. *Angew. Chemie* **2015**, *127* (17), 5268–5271. https://doi.org/10.1002/ange.201412214.

(44)   De Gregorio, G. L.; Burdyny, T.; Loiudice, A.; Iyengar, P.; Smith, W. A.; Buonsanti, R. Facet-Dependent Selectivity of Cu Catalysts in Electrochemical CO2 Reduction at Commercially Viable Current Densities. *ACS Catal.* **2020**, *10* (9), 4854–4862. https://doi.org/10.1021/acscatal.0c00297.

(45)   Huang, J.; Hörmann, N.; Oveisi, E.; Loiudice, A.; De Gregorio, G. L.; Andreussi, O.;

Marzari, N.; Buonsanti, R. Potential-Induced Nanoclustering of Metallic Catalysts during Electrochemical CO2 Reduction. *Nat. Commun.* **2018**, *9* (1), 1–9. https://doi.org/10.1038/s41467-018-05544-3.

(46) Gunathunge, C. M.; Li, X.; Li, J.; Hicks, R. P.; Ovalle, V. J.; Waegele, M. M. Spectroscopic Observation of Reversible Surface Reconstruction of Copper Electrodes under CO2 Reduction. *J. Phys. Chem. C* **2017**, *121* (22), 12337–12344. https://doi.org/10.1021/acs.jpcc.7b03910.

(47) Li, H.; Wei, P.; Gao, D.; Wang, G. In Situ Raman Spectroscopy Studies for Electrochemical CO2 Reduction over Cu Catalysts. *Curr. Opin. Green Sustain. Chem.* **2022**, *34*, 100589. https://doi.org/10.1016/j.cogsc.2022.100589.

(48) Gunathunge, C. M.; Ovalle, V. J.; Li, Y.; Janik, M. J.; Waegele, M. M. Existence of an Electrochemically Inert CO Population on Cu Electrodes in Alkaline PH. *ACS Catal.* **2018**, *8* (8), 7507–7516. https://doi.org/10.1021/acscatal.8b01552.

(49) Dattila, F.; Seemakurthi, R. R.; Zhou, Y.; López, N. Modeling Operando Electrochemical CO2Reduction. *Chem. Rev.* **2022**, *122* (12), 11085–11130. https://doi.org/10.1021/acs.chemrev.1c00690.

(50) Weng, Z.; Zhang, X.; Wu, Y.; Huo, S.; Jiang, J.; Liu, W.; He, G.; Liang, Y.; Wang, H. Self-Cleaning Catalyst Electrodes for Stabilized CO 2 Reduction to Hydrocarbons Zuschriften Angewandte. **2017**, 13315–13319. https://doi.org/10.1002/ange.201707478.

(51) Kas, R.; Kortlever, R.; Yılmaz, H.; Koper, M. T. M.; Mul, G. Manipulating the Hydrocarbon Selectivity of Copper Nanoparticles in CO 2 Electroreduction by Process Conditions. **2015**, 354–358. https://doi.org/10.1002/celc.201402373.

(52) Korzeniewski, C.; Pons, S.; Schmidt, P. P.; Severson, M. W. A Theoretical Analysis of the Vibrational Spectrum of Carbon Monoxide on Platinum Metal Electrodes. *J. Chem. Phys.* **1986**, *85* (4153). https://doi.org/https://doi.org/10.1063/1.450888.

(53) Lambert, D. K. Vibrational Stark Effect of CO on Ni(100), and CO in the Aqueous Double Layer: Experiment, Theory, and Models. *J. Chem. Phys.* **1988**, *89* (3847). https://doi.org/https://doi.org/10.1063/1.454860.

(54) Chemistry, L. *π-Bonding between Metals and Ligands*. https://chem.libretexts.org/Bookshelves/Inorganic_Chemistry/Book%3A_Introduction_to_Inorganic_Chemistry_%28Wikibook%29/05%3A_Coordination_Chemistry_and_Crystal_Field_Theory/5.05%3A_-Bonding_between_Metals_and_Ligands (accessed 2023-01-17).
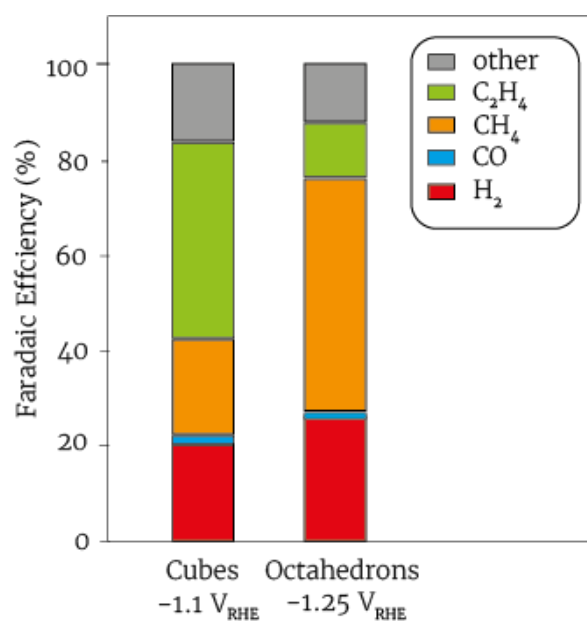
Figure A1: Activity measurements carried out on the copper nanoparticles measured in 0.1M KHCO₃ figure adapted from Buonsanti et al.[39,40]

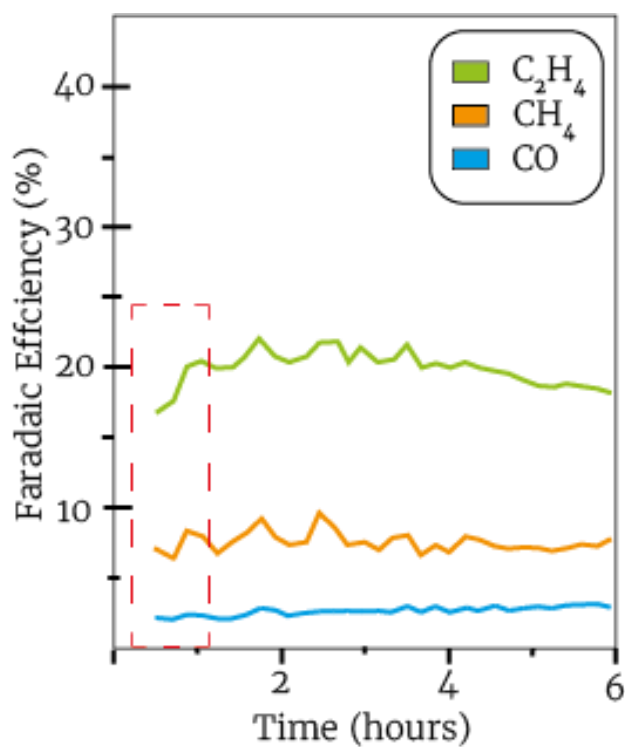Figure A2: Time-dependent activity for Cu nanoncubes of 41 nm under –1.1 V$_{RHE}$ in 0.1M KHCO₃ electrolyte, adapted from Huang et al[45]
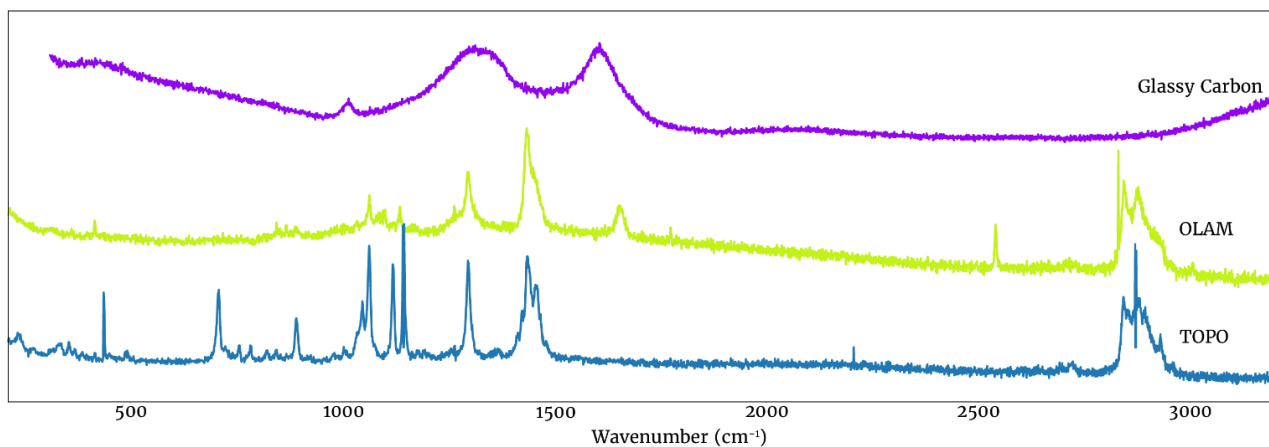
Figure A3: Raman spectra of ligand species and glassy carbon. Ligands were measured in powder form, glassy carbon in 0.1 M KHCO₃ electrolyte
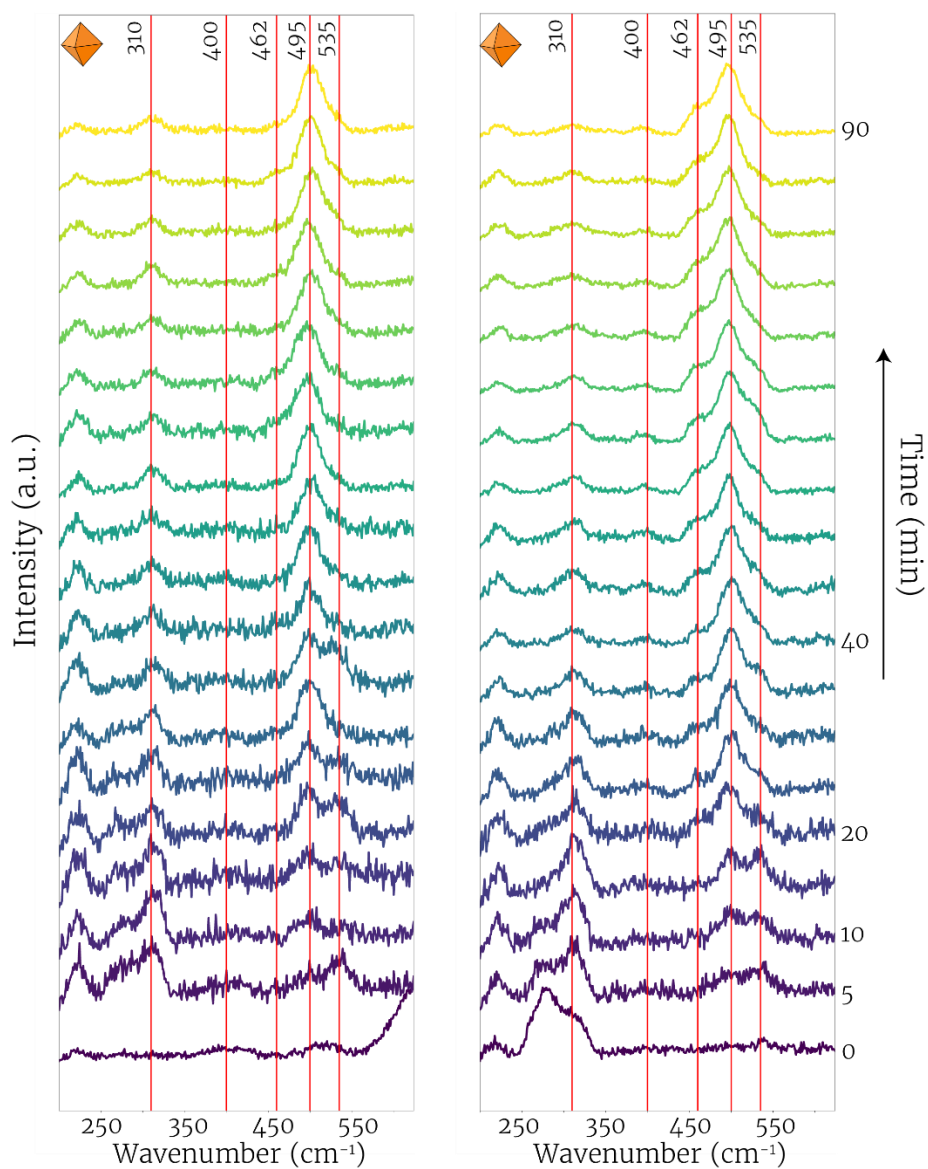

Figure A4: Two time-dependent Raman experiments of different octahedra electrodes measured at -0.85 V$_{RHE}$ in CO$_2$ saturated 0.1 M KHCO₃ electrolyte
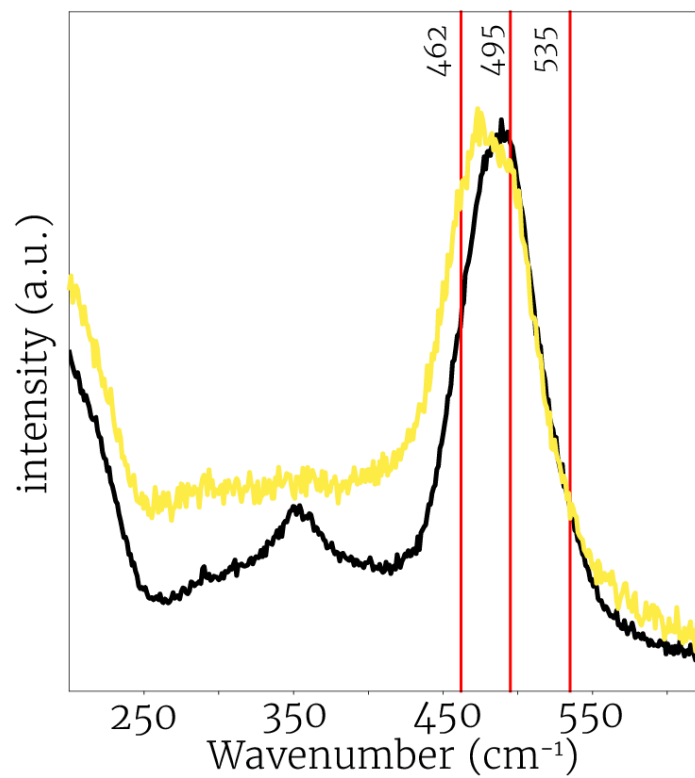
Figure A5: Two Raman spectra measured on the same cube sample, but at a different spot measured at roughly 1 min apart, at 45 min , –1.0 V_{RHE} in CO$_2$ saturated 0.1 M KHCO$_3$ electrolyte

Optimized geometries on (100) facet

CO

OH

HCO

CO$_B$

CO$_T$ = CO$_L$

CO$_F$

OH (F)

HCO (T)

HCO (BT)

Optimized geometries on (111) facet

CO

OH

CO$_B$

CO$_T$ = CO$_L$

CO$_{Th}$

CO$_{Tf}$

OH (T$_f$)

OH (T$_h$)

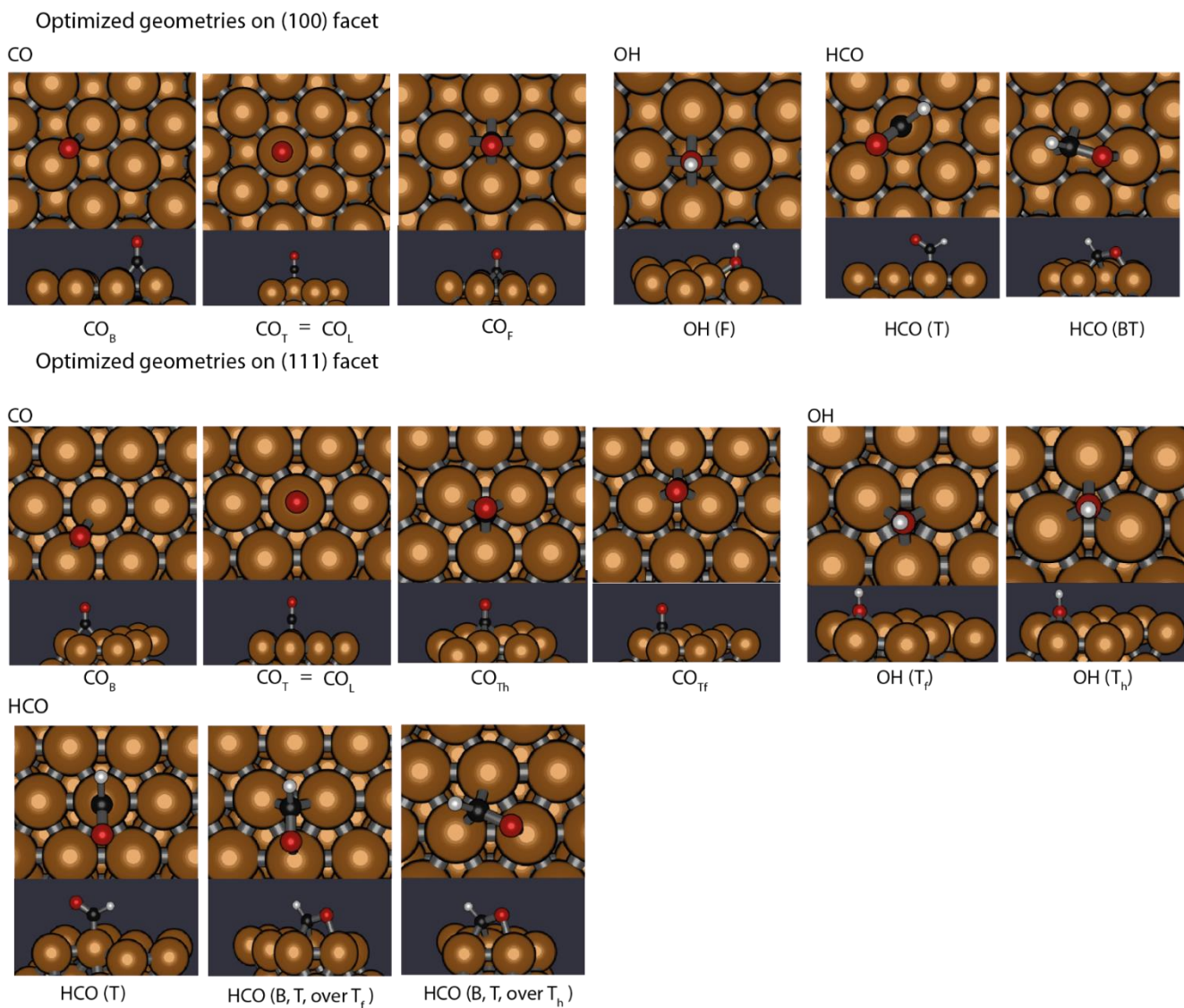HCO

HCO (T)

HCO (B, T, over T$_f$)

HCO (B, T, over T$_h$)
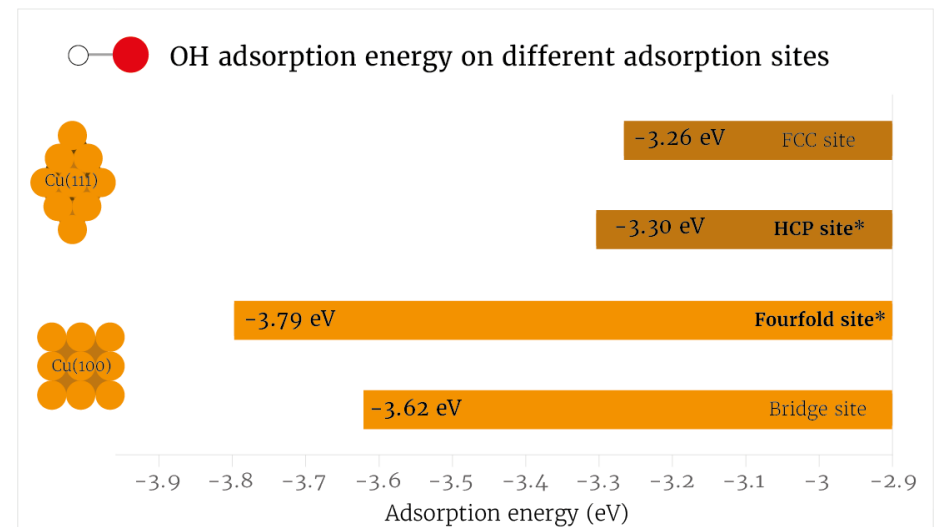
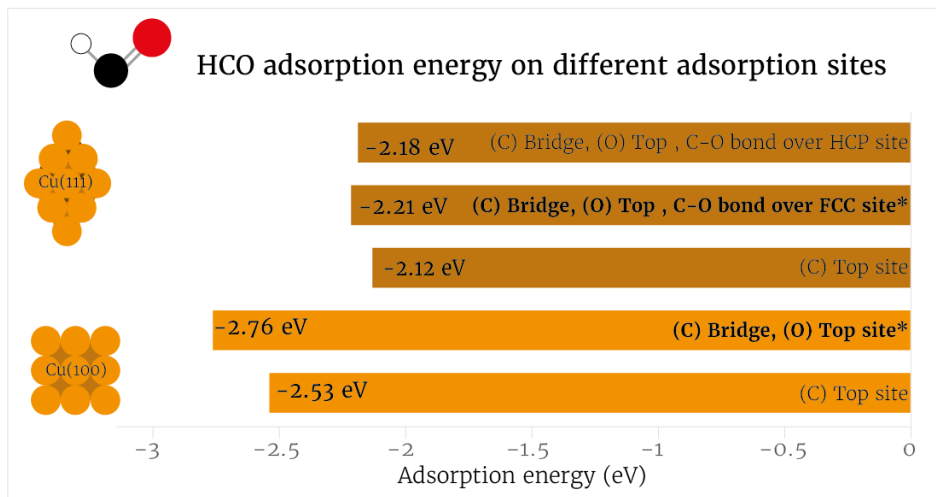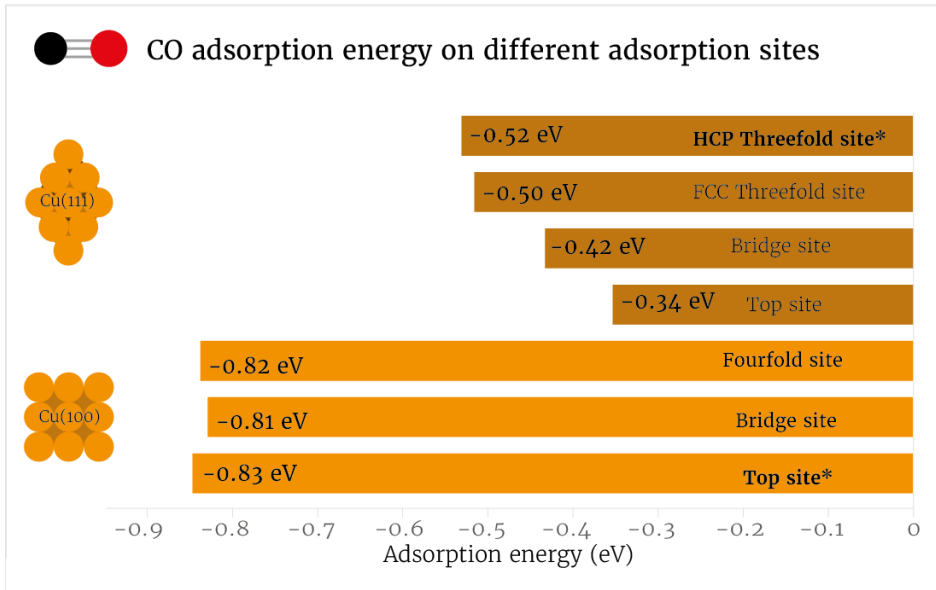*Figure A6: Overview of all the calculated optimized geometries*
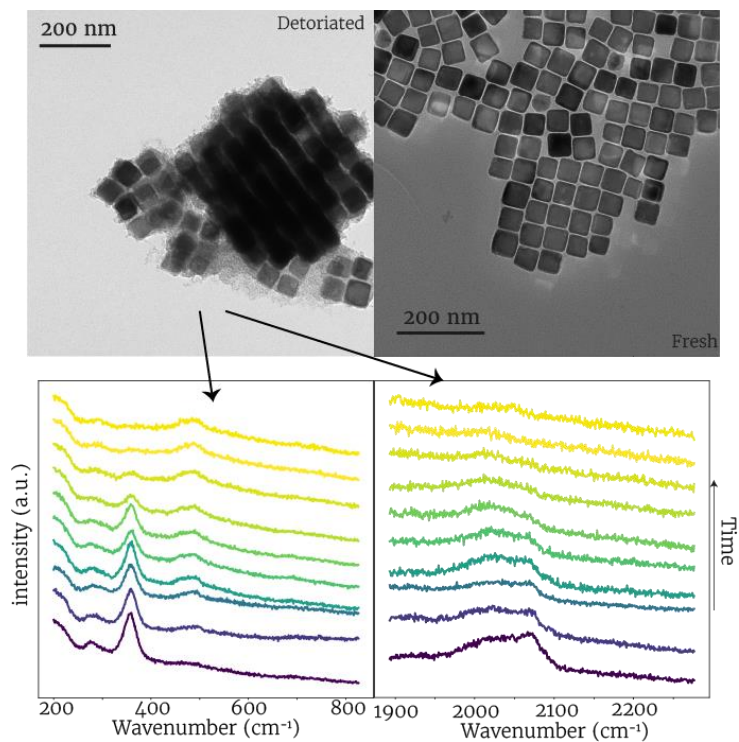
Figure A7: Overview of all calculated adsorption energies

Figure A8: Linear CO vibrations observed on deteriorated Cu Cubes. Measurement was carried out at -0.85 V_{RHE} in CO_2 sat. 0.1 M $KHCO_3$

Table A1: Overview of the calculated vibrational modes on the calculated stable geometries

CO	**T (100)**	T (111)	B (100)	B (111)	F (100)	T_f (111)	**T_h (111)**
E_{ads} (eV)	-0.83	-0.34	-0.81	-0.42	-0.82	-0.50	-0.52

Vibrations (cm^{-1})	**T (100)**	T (111)	B (100)	B (111)	F (100)	T_f (111)	**T_h (111)**
V_{M-C}	393	388	323	326	259	308	315
V_{C-O}	2020	2016	1883	1869	1695	1821	1815
V_{bend}	267/274	266/273	293	258	234	227/240	237/244

OH	B (100)	**F (100)**	**T_f (111)**	T_h (111)
E_{ads} (eV)	-3.62	-3.79	-3.30	-3.26

Vibrations (cm^{-1})	B (100)	**F (100)**	**T_f (111)**	T_h (111)
V_{M-O}	433	322	398	397
V_{O-H}	3755	3650	3708	3693
$V_{rocking}$	363	181	264	249
V_{bend}	616	595	455-480	455-471

HCO	T (100)	T (111)	**BT**	**B, T, over T_f**	B,T over T_h
E_{ads} (eV)	-2.53	-2.12	-2.76	-2.21	-2.18

Vibrations (cm^{-1})	T (100)	T (111)	**BT**	**B, T, over T_f**	B,T over T_h
M-adsorbate	427	430	434	429	401
C-O	1670	1674	1352	1396	1405
wagging	656	676	630	604	589
sciccoring	1181	1186	1243	1235	1227
C-H	2750	2784	2827	2856	2842

Table A2: Calculated Stark Shifts for CO on all adsorption sites the (111) facet

CO on (111)	T 0	T + (↑)	T - (↓)	B 0	B + (↑)	B - (↓)
V_{M-C}	393	385 ↓	415 ↑	339	329 ↓	347 ↑
V_{C-O}	2031	2076 ↑	1984 ↓	1880	1939 ↑	1830 ↓
V_{bend}	336	286 ↓	347 ↑	201	252 ↑	309 ↑

CO on (111)	T_f 0	T_f + (↑)	T_f (↓)	T_h 0	T_h + (↑)	T_h (↓)
V_{M-C}	314	311 ↓	316 ↑	320	311 ↓	314 ↓
V_{C-O}	1829	1905 ↑	1772 ↓	1823	1897 ↑	1786 ↓
V_{bend}	201	215 ↑	206 ↑	252	211 ↓	287 ↑

Table A3: Calculated Stark Shifts for CO on all adsorption sites the (100) facet

CO on (100)	T 0	T + (↑)	T - (↓)	B 0	B + (↑)	B - (↓)	F 0	F + (↑)	F - (↓)
V_{M-C}	393	385 ↓	415 ↑	339	329 ↓	347 ↑	258	259 ~	271 ↑
V_{C-O}	2031	2076 ↑	1984 ↓	1880	1939 ↑	1830 ↓	1706	1755 ↑	1660↓
V_{bend}	336	286 ↓	347 ↑	201	252 ↑	309 ↑	239.2	252 ↑	303 ↑